DESIGN AND DEVELOPMENT OF A 12" x 12" SHOCK TUBE.

By

ALAN MOORE

Research Assistant, Department of Aeronautics and Fluid Mechanics, The University of Glasgow.

CORRIGENDA.

26th.,Oct.,1966

Page 27 : for fig.(3. 11), read fig.(3. 12),

28 : for fig.(3. 12), read fig.(3. 11).

66 : the correct expression for equation (5. 1) is

$$\omega.dr = \frac{\sqrt{3}}{2}r(k - 2) + 2a$$

and for equation (5. 2) is,

$$T_{p_w} = p\left[\frac{\sqrt{3}}{2}r(k - 2) + 2a\right]r.dr.$$

71 : the correct expression for equation (5. 10) is,

$$\left(\frac{A_r}{A_t}\right)^2 = \frac{\gamma - 1}{2}\cdot\frac{\left(\frac{2}{\gamma + 1}\right)^{\frac{\gamma + 1}{\gamma - 1}}}{\left[1 - \left(\frac{p_r}{p_o}\right)^{\frac{\gamma - 1}{\gamma}}\right]\left(\frac{p_r}{p_o}\right)^{\frac{2}{\gamma}}}.$$

77 : for appropraite, read appropriate.

SUMMARY

The simple one-dimensional theory for the inviscid flow in a constant area shock tube is reviewed and data on wave velocities and flow durations, derived on the basis of this theory, is presented in graphical form. Consideration is given to the deviations from these predicted results, which will arise as a consequence of, the real gas effects, the viscous nature of the channel gas and the non-ideal diaphragm performance.

The design of the shock tube is described in detail and illustrated. Novel features included are, the hydraulic clamp and the rubber suspension. Likewise the instrumentation is described, with particular emphasis on the design and use of thin film heat transfer gauges.

A theoretical assessment of the real diaphragm opening is made, with particular reference to large thin steel discs, as used in the 12"x12" Shock Tube. Wave diagrams, following the non-instantaneous diaphragm opening, are plotted for two particular cases and comparison is made with shock trajectories measured over the first six feet of the tube length. Theoretical consideration is given to the variation in state parameters, with time, after the passage of the shock wave past a fixed station. The criterion for shock formation is discussed and White's definition ratified, in the absence of petal rebound. The effect of non-ideal diaphragm performance on flow durations, which should be obtained at a fixed station, is noted.

Measurements of, diaphragm opening time, shock trajectories and flow duration are plotted. Measured flow durations are compared with work of a similar nature in a smaller tube and an improvement noted. A method of assessing flow uniformity is discussed and a rudimentary evaluation of its sensitivity made.

CONTENTS

CHAPTER 1.

NOTATION

NOTATION.

Upper Case Alphabet

A	area of a section
E	Young's Modulus
	Voltage
I	moment of inertia
M	Mach No.
N	slope of a characteristic
R	radius of curvature
T	temperature
	torque about an axis
U	free stream velocity
V	voltage
W	specific weight (force/unit area)

Upper Case Letters (non-dimensional ratios)

A	speed of sound (eg. $A_{14} = \frac{a_1}{a_4}$)
E	energy ratio
P	pressure ratio
U	velocity (eg. $U_{14} = \frac{u_1}{a_4}$)
W	wave velocity
X	length

Non-dimensional Constants

Nu	Nusselt No.
Pr	Prandtl No.
Re	Reynolds No.

Lower Case Alphabet

a	speed of sound
	half dimension of the tube
c	diaphragm constant,(derived in Chap. 5)
f	stress
g	gravitational constant
k	constant, describing the scribe pattern
	thermal conductivity
ℓ	length, (defined as required)
p	pressure
q	heat transferred
r	local value of radius
s	entropy
t	time, (defined as required)
u	velocity
w	local value of width
x	distance along the channel

Greek Symbols

Δ	increment
α	coefficient of resistivity
	gas constant defined in Chap. 2
β	gas constant defined in Chap. 2
γ	ratio of specific heats
δ	boundary layer thickness
ϵ	strain
μ	viscosity
ν	Poisson's Ratio
θ	angular displacement of a diaphragm petal
ρ	density
σ	radius of a heat transfer probe
ω	angular velocity
η	density ratio, Chap. 3

Subscripts

1, 2, etc. refer to the regions labelled as in fig.(2. 1)

s	shock wave
t	throat
w	shock tube wall
r	value at a local radius
i	inlet to nozzle
z	exit from nozzle
b	component due to bending
p	component due to pressure
o	stagnation value
	value at time when $\theta = 30^{o}$
y	value at the yield point
f, ult.	value at failure

Superscripts

*	local sonic value

ACKNOWLEDGEMENT.

This project was initiated under the guidance of the late Professor W. J. Duncan. I wish to express my thanks to Professor T. R. F. Nonweiler for his support in the continuation of the work, and for his guidance and criticism.

I also wish to thank Mr. A. MacNeill and his staff in the Engineering Department Workshops for their co-operation during the installation and development of the equipment.

Thanks are also due to my colleagues in the Department of Electrical Engineering for their assistance, both practical and by way of discussion, in the design and development of the instrumentation.

CHAPTER 2.

THE PERFORMANCE OF A SIMPLE CONSTANT AREA SHOCK TUBE

THE PERFORMANCE OF A SIMPLE CONSTANT AREA SHOCK TUBE

INTRODUCTION.

It is not proposed to develop the simple one dimensional inviscid theory for the performance of a shock tube, since this may be found in a number of treatises, eg. refs.(1), (2), (3) and (4). We shall, however quote the equations of motion of the various waves governing the performance of the simple tube and derive performance data for the 12"x12" tube at Glasgow University. Deviations from the performance, predicted by the simple theory, will be large, particularly when strong shocks are driven into low pressures.

These effects do not invalidate the use of curves based on the simple theory, since much of the initial calibration work will be carried out in conditions, where the departures from the ideal case will be minimal. It is also expected that the proportions, small length to diameter ratio, of the tube, will minimise viscous effects.Finally, it will be the practice to express the actual performance relative to the simple theoretical predictions.

EQUATIONS OF MOTION.

The chosen model for the shock tube assumes that the diaphragm bursts instantaneously and that the gas is perfect and inviscid. The resulting wave motion after instaneous rupture of the diaphragm is shown in fig. (2. 1). The shock is assumed to accelerate to a constant velocity, whilst the backward facing rarefaction wave moves at the speed of sound in region 4.

The diaphragm is ruptured at time $t=0$, and the pressure and the particle velocity can be shown to be the same in regions 2 and 3, ref.(1). A contact surface must be assumed for the coexistence of states 2 and 3, which were formed by two entirely different processes and which have

different densities, temperatures, internal energies and entropies. The states 2 and 3 are, however assumed to be uniform since the changes of state occur through the waves and the contact surface.

The shock tube problem is solved by taking the standard equations for the forward facing shock wave,

$$\frac{u_2}{a_1} = \left[\frac{p_2}{p_1} - 1\right] \cdot \left[\frac{2}{\gamma_1 \left(\gamma_1 + 1\right) \cdot p_{2/p_1} + \left(\gamma_1 - 1\right)}\right]^{\frac{1}{2}} \qquad \ldots\ldots (2.\ 1)$$

and a backward facing rarefaction wave,

$$\frac{u_3}{a_4} = \frac{2}{\gamma_4 - 1}\left\{1 - \left[\frac{p_3}{p_4}\right]^{\frac{\gamma_4 - 1}{2\gamma_4}}\right\} \qquad \ldots\ldots (2.\ 2)$$

and matching the velocities and pressures resulting from the compression of the gas in region 1 by the shock wave and the expansion of the gas from region 4 through the rarefaction wave. The equations

$$u_2 = u_3 \quad \text{and} \quad p_3 = p_2 , \qquad \ldots\ldots (2.\ 3\ \&\ 4)$$

express this condition.

Expressing equations (2. 1, 2, 3 & 4) in non-dimensional form,

$$U_{21} = \frac{P_{21} - 1}{\gamma_1 \sqrt{\beta_1 \left(\alpha_1 \cdot P_{21} + 1\right)}}, \qquad \ldots\ldots (2.\ 5)$$

$$U_{34} = \frac{1}{\gamma_4 \beta_4} \cdot \left[1 - \left(P_{34}\right)^{\beta_4}\right] \qquad \ldots\ldots (2.\ 6)$$

$$U_{34} = A_{14} \cdot U_{21} \qquad \ldots\ (2.\ 7)$$

and

$$P_{34} = P_{14} \cdot P_{21} \qquad \ldots\ (2.\ 8)$$

where

$$\alpha = (\gamma + 1)/(\gamma - 1)$$

and

$$\beta = (\gamma - 1)/2\gamma,$$

they may be combined to form a relation between the shock pressure ratio P_{21} and the known parameters P_{14}, A_{14}, γ_4 and γ_1.

An explicit solution for P_{21} in terms of the other variables has not been found, but a convenient expression for a graphical solution has been arrived at and is expressed here in terms of the initial energy ratio E_{14}, where

$$A_{14} = \frac{\gamma_1}{\gamma_4} \cdot \left[\frac{\beta_1}{\beta_4} \cdot E_{14} \right]^{\frac{1}{2}} \qquad \ldots\ (2.\ 9)$$

viz.,

$$P_{14} = \frac{1}{P_{21}} \left\{ 1 - (P_{21} - 1) \left[\frac{\beta_4 \cdot E_{14}}{\alpha_1 P_{21} + 1} \right]^{\frac{1}{2}} \right\}^{\frac{1}{\beta_4}} \qquad \ldots\ (2.\ 10)$$

The use of the energy ratio rather than the sound speed ratio restricts the validity of the solution to cases where there is no ionisation or dissociation of the gas.

Graphical and tabulated solutions of equation (2. 10) are found in refs. (1), (2), (3) and (4), and data has been extracted from them and applied in dimensional form to the particular conditions normally encountered in the operation of the 12"x12" shock tube. Generally speaking the data from ref. (1) has been used wherever possible. The data presented in figures (2. 2-3) allows one to predict the shock strength

W_{11} or P_{21}, based on the initial pressure ratio. The ideal shock trajectory is illustrated in fig.(2. 4).

EFFECT OF VARIATION IN INITIAL BURSTING PRESSURE RATIO ON SHOCK TRAJECTORY

Referring to fig.2.3.18 of ref.(1), it is apparent that the variation of W_{11} with P_{41} is practically logarithmic for the case Air: Air over the range, which is of practical interest. The case He: Air may be treated similarly. Table I is derived from data extracted from figs. 2.3.15,16 and 23 of ref.(1).

	Air : Air		He : Air	
$\text{Log}_{10}P_{41}$	P_{21}	W_{11}	P_{21}	W_{11}
5	22.5	4.46	-	-
4	17.0	3.87	56.5	7.00
3	11.4	3.17	33.6	5.42
2	6.4	2.40	15.0	3.64
1	2.8	1.60	4.6	2.04
0	1.0	1.00	1.0	1.00

Table I

Table I has been plotted in fig.(2. 5) and the undernoted functions, valid in the range $1 < \log_{10}P_{41} < 4.0$, have been fitted to the curves.

(a) Air : Air, $W_{11} = 0.9 + 0.75\log_{10}P_{41}$ .... (2. 11)

(b) He : Air, $W_{11} = 0.4 + 0.6\log_{10}P_{41}$ .... (2. 12)

Consider case (a), and assume a 5% variation in the value of P_{41}: from equation (2. 11);

$$W_{11}^{*} = 0.9 + 0.75\log_{10}P_{41}(1 \pm 0.05)$$

$$= W_{11} + 0.75\log_{10}(1 \pm 0.05).$$

so that when P_{41} is 5% greater than desired,

$$W_{11}^{*} = W_{11} + 0.015$$

and for a typical value, $W_{11} = 3.0$ the variation in W_{11} for a 5% increase in P_{41} is

$$\triangle W_{11} = 0.5\%.$$

With the existing vacuum gauges one would hesitate to credit them with an accuracy of better than 1%, hence the assumption; the shock velocity is sensibly independent of minor changes in diaphragm bursting pressure, is theoretically justifiable. If one now refers to fig.(2. 4) and evaluates the decrease in the time required by the shock wave to pass two stations 2 feet apart, when $W_{11} = 3.0$, this time $t = 600$ microseconds and the reduction $\triangle t$ corresponding to a 5% increase in P_{41} is 3 microseconds, which is insignificant compared to the increase one would expect to result from shock attenuation.

It should be noted that because of the logarithmic relationship between W_{11} and P_{41}, the variation in the value of W_{11} is only a function of the relative change in P_{41} and is independent of the absolute value of P_{41}.

It will be seen from the form of equation (2. 12) that errors in W_{11} caused by inconsistent bursting pressures will be less in the case, He : Air, than those for the case, Air : Air.

IDEAL RUNNING TIME PREDICTION

Referring to fig.(2. 1), the running time at station x is defined as the duration of quasi- steady flow obtained after the passage of the shock front and terminated by the arrival of the contact surface. The maximum running time is obtained at that station where the reflected shock wave meets the contact surface. The basic

parameter chosen for the following data is the shock Mach No., W_{11}. The non-dimensional particle velocity U_{21} is also the velocity of the contact surface and is given in equation (2. 5). Thus knowing the trajectories of the shock wave and the contact surface, it is simple to evaluate the running time at any station, where the flow has not been interfered with by other waves, namely the reflected shock wave and the reflected head of the rarefaction wave. The data for contact surface trajectory has been taken from fig. 2.3.23 of ref.(1) and fig.(2. 6) depicts the running time.

The boundaries, which limit the use of this curve are presented in fig.(2. 7) and the data on the reflected shock wave has been taken from table VI of ref.(3), whilst the data on the reflected head of the rarefaction wave has been extracted from ref.(2). The maximum running time and the time between the passage of the incident shock and the reflected shock are also shown in fig.(2. 6).

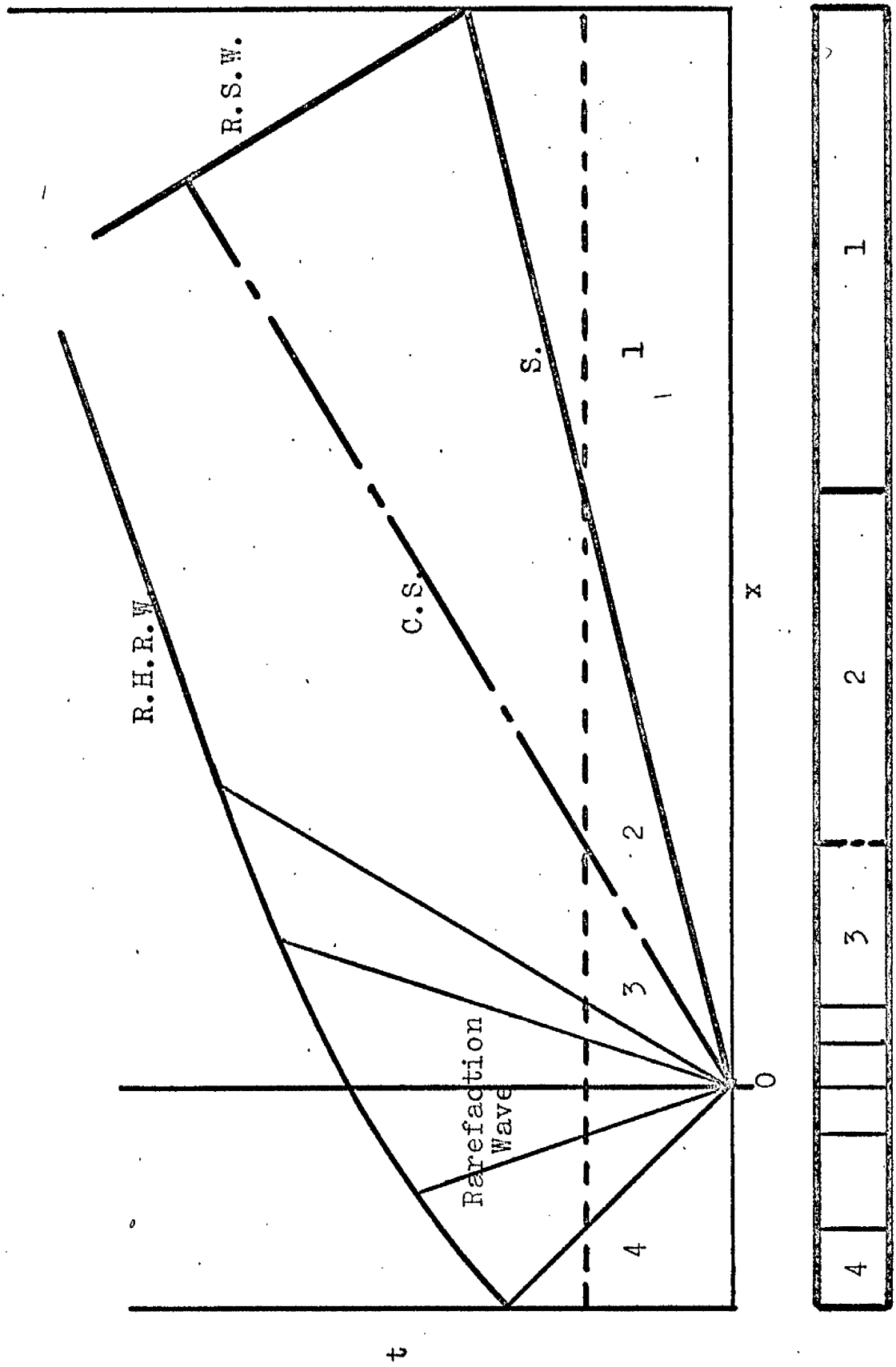

Fig. (2. 1)

x - t. Diagram Following the Instantaneous Removal of the Diaphragm in a Shock Tube.

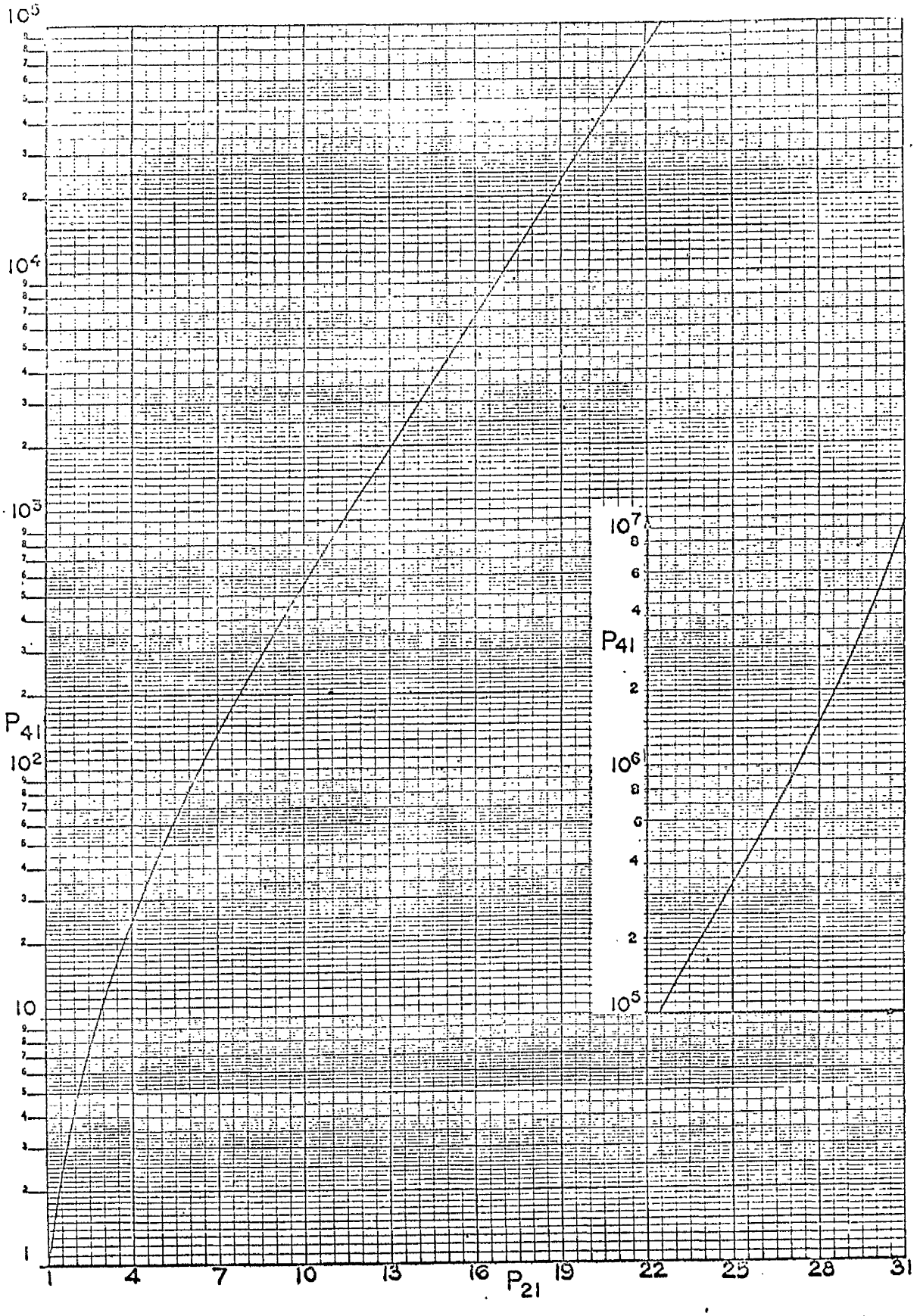

Variation of the initial shock pressure ratio (P_{21}) with the diaphragm pressure ratio (P_{41}); case air/air.

Fig. (2. 2a)

235

546697 O-60—18

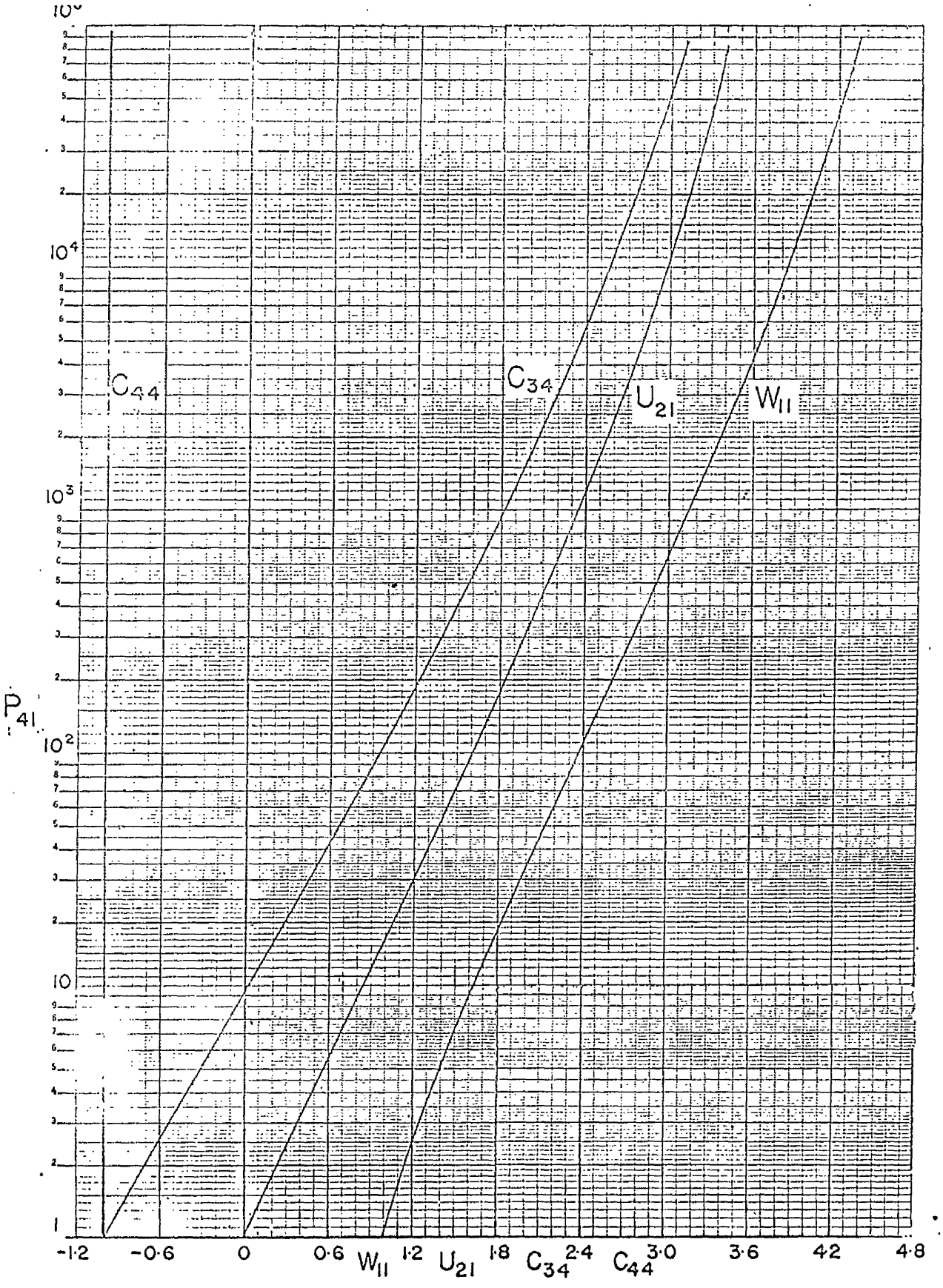

Variation of initial shock wave velocity (W_{11}), particle velocity (U_{21}), and rarefaction front velocities (C_{44} and C_{34}) with the pressure ratio (P_{41}) across the diaphragm; case air/air.

238

Fig. (2. 2b)

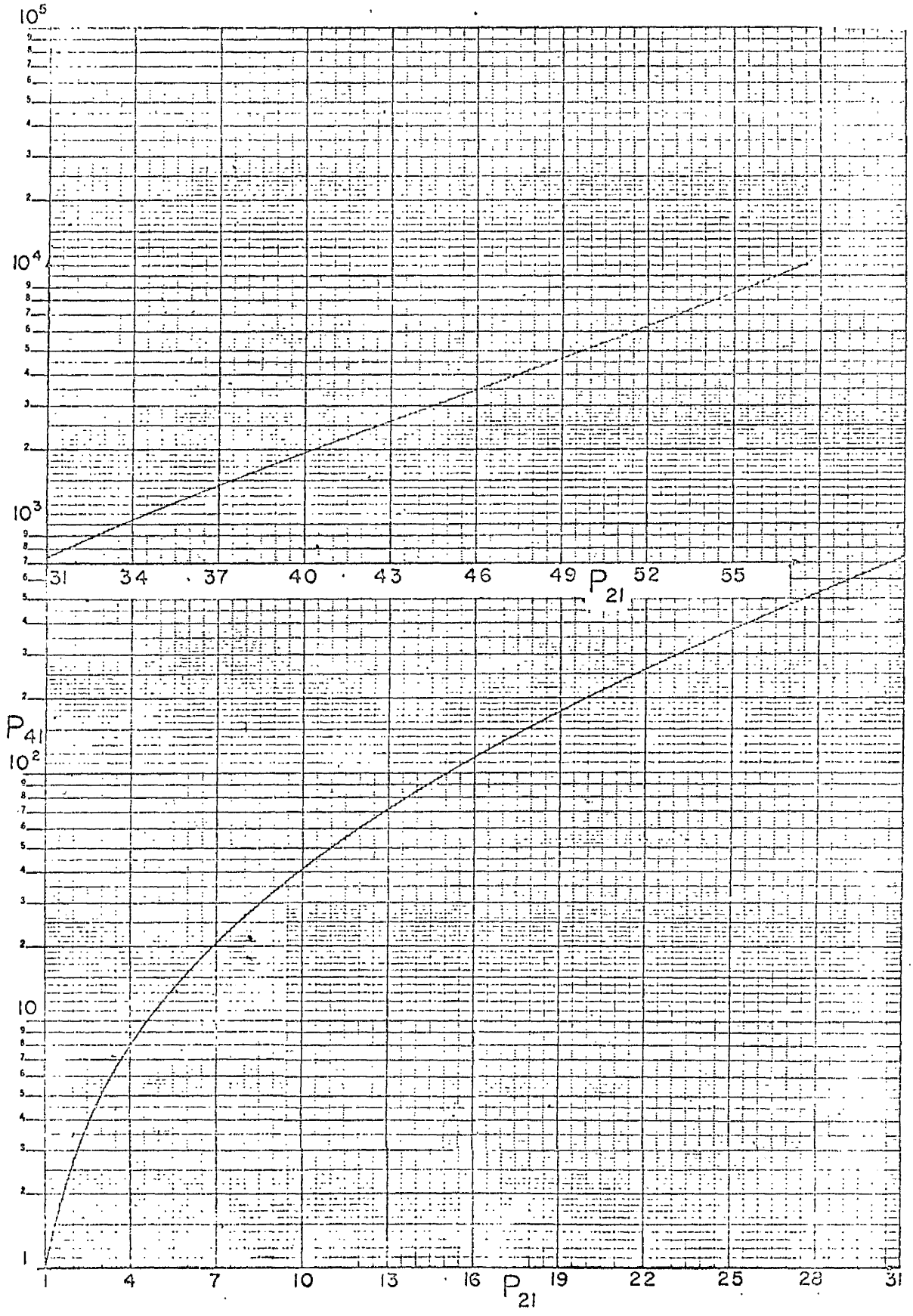

Variation of the initial shock-wave pressure ratio (P_{21}) with the diaphragm pressure ratio (P_{41}); case He/air, $\gamma_4 = 1.665$, $\gamma_1 = 1.402$, $T_4 = T_1$.

Fig. (2. 3)

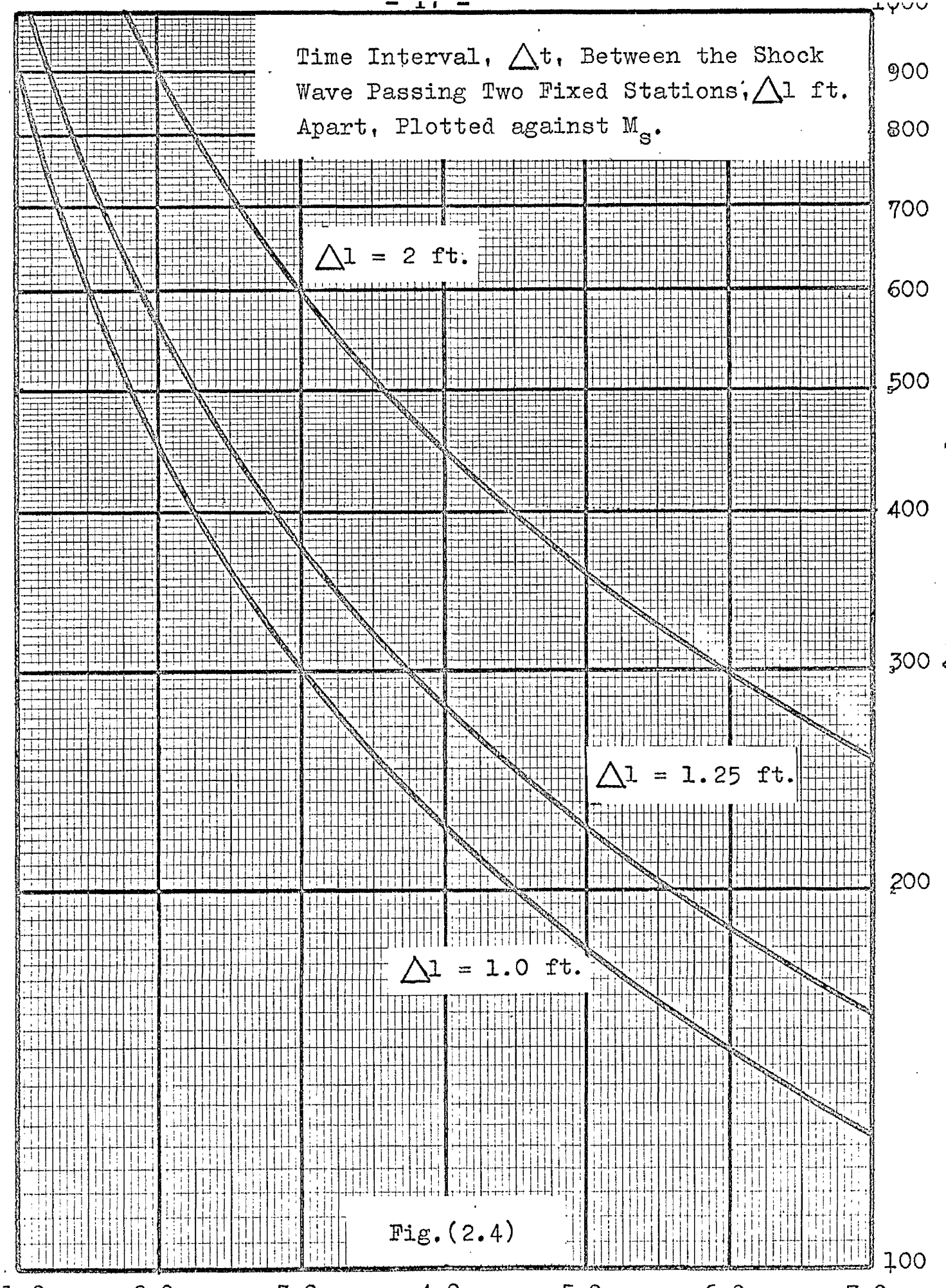
Time Interval, △t, Between the Shock Wave Passing Two Fixed Stations, △l ft. Apart, Plotted against M_s.
△l = 2 ft.
△l = 1.25 ft.
△l = 1.0 ft.
900
800
700
600
500
400
300
200
100
△t - microseconds
1.0
2.0
3.0
4.0
5.0
6.0
7.0
Shock Mach No., M_s

Fig.(2.4)

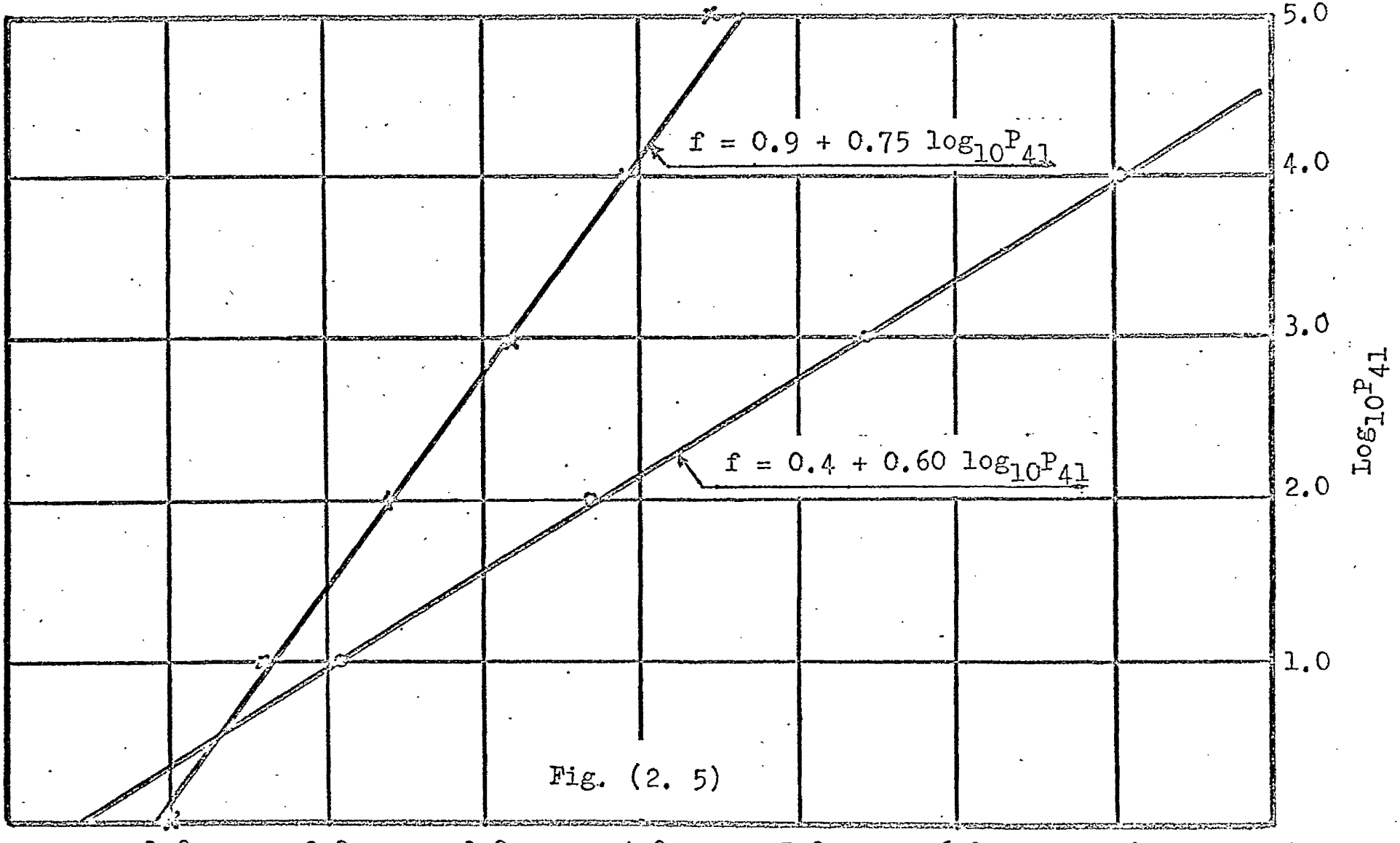

Fig. (2. 5)

Approximate Relationships for Shock Mach No. M_s, Valid in the range $1 < \log_{10} P_{41} < 4$

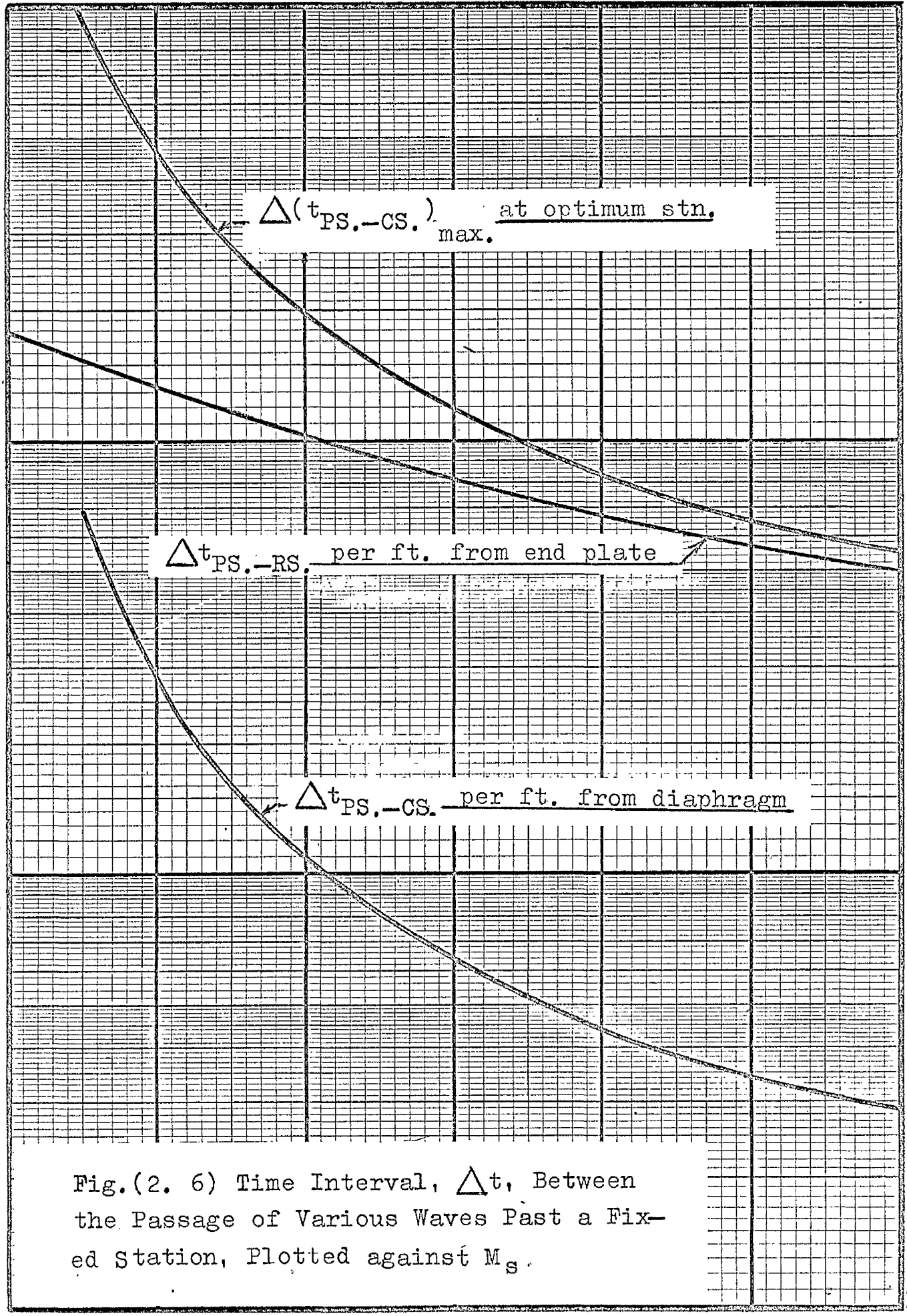

Fig.(2. 6) Time Interval, Δt, Between the Passage of Various Waves Past a Fixed Station, Plotted against M_s.

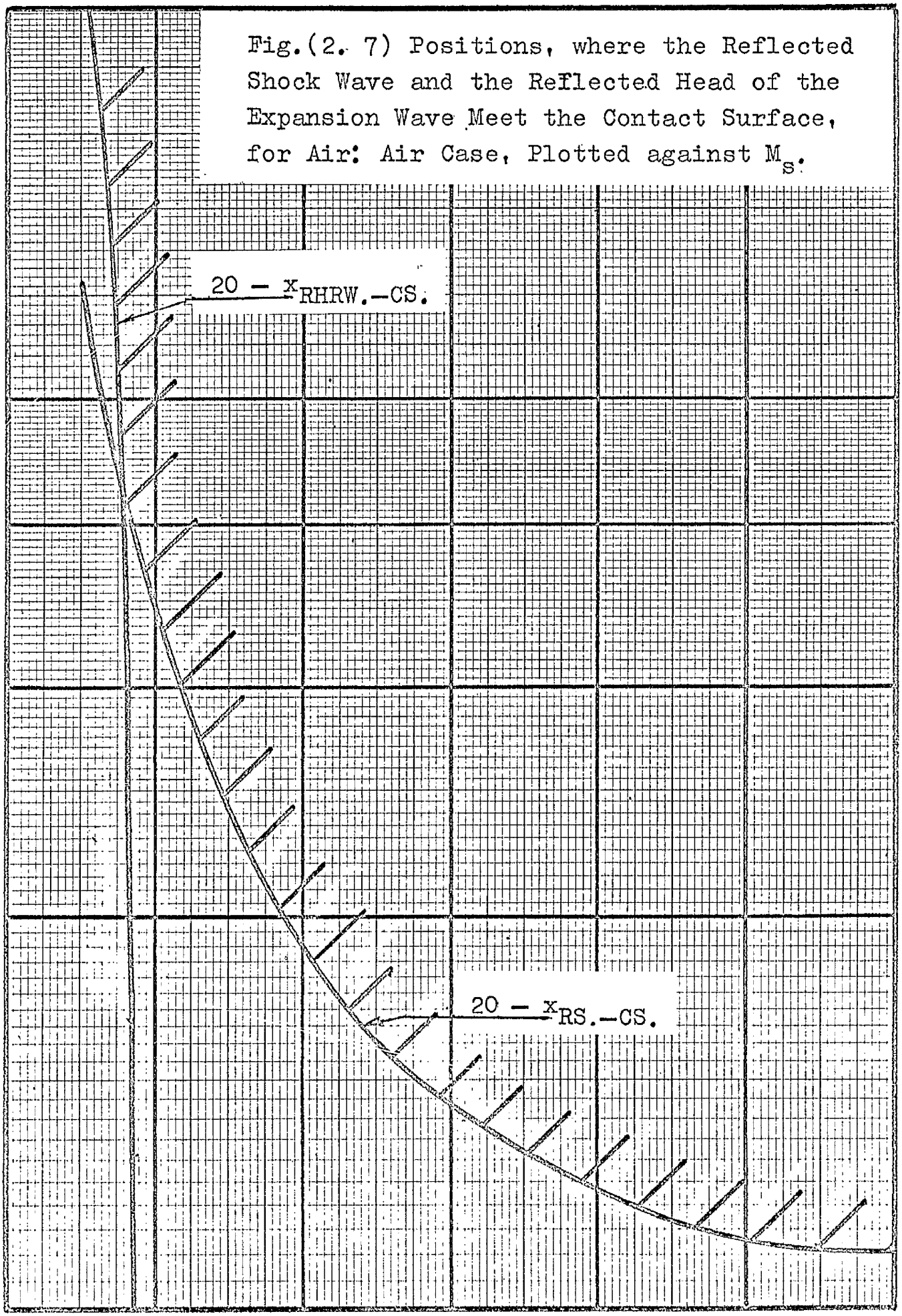

Fig.(2. 7) Positions, where the Reflected Shock Wave and the Reflected Head of the Expansion Wave Meet the Contact Surface, for Air: Air Case, Plotted against M_s.

CHAPTER 3.

DEPARTURES FROM THE IDEAL THEORY

DEPARTURES FROM IDEAL THEORY

INTRODUCTION

The data presented in Chapter 2 is based on the idealised conditions; ie. instantaneous removal of the diaphragm separating the two gases, which are assumed to be perfect and inviscid. These three assumptions are not valid under certain conditions.

(a) The fact that the gases are real asserts itself at temperatures corresponding to $M_s = 4$.

(b) Since the gas in the channel is viscous, a boundary layer develops along the walls behind the shock front, as the shock moves down the channel. The boundary layer has a marked effect on the motion of the shock and the properties of the flow behind the shock, when the initial channel pressure is low, ie. 1.0 Torr.

(c) The diaphragm requires a finite time, of the order 1 millisecond, to open completely. During this period a series of compression waves and shock waves emanate from the diaphragm station and coalesce into a shock front some little way down the tube. This leads to a shock wave effectively starting at some downstream station and of a strength, which is to some extent determined by the bursting process.

REAL GAS EFFECTS.

In the shock tube imperfections in the gas properties arise, as a result of the high temperatures and the low pressures involved. The equation of state is then of the form

$$p = \rho RT(1 + \alpha), \qquad \ldots\ (3.1)$$

and the specific heat ratio cannot be considered constant. The shock heated gas in region 2, fig.(2. 1) will depart significantly from ideal conditions when $M_s = 4$.

At low temperatures the energy is shared between the translational and rotational degrees of freedom of the gas molecules only. As the temperature rises the higher modes are progressively excited. At around 1000° C. a significant proportion of the internal energy is vested in the vibrational degrees of freedom. As the temperature further increases all the vibrational modes are excited. Eventually the gas will dissociate, which may be followed by chemical reactions. Finally all the components will be excited electronically, with subsequent ionisation. These processes are not separated in the 'clear cut' manner as described above, but will overlap one another to a certain extent.

The temperatures at which one must consider any one process will vary with the channel gas. For a monatomic gas one need only consider the translational degree of freedom and eventually the electronic degrees. In this analysis we are particularly concerned with the gas mixture, air. At the shock Mach Nos. attainable in the 12"x12" tube, viz. $M_s \doteqdot 7$, the vibrational modes are the only ones of any significance behind the incident shock.

Thus the equilibrium state properties of the gas behind the incident shock will be a function of the shock Mach No. In particular the specific heat ratio γ will not be a constant 1.4 for air. Fig.(3. 7), which has been taken from ref.(1), illustrates the variation in M_s for the same values of initial pressure ratio, if one includes the effect of variations in γ as a result of vibrational excitation in an Air : Air shock tube. It should be noted that the practical significance is small in the Air : Air case, since the reduction in M_s is small at constant initial pressure ratio, eg.,

$P_{41} = 4 \times 10^4$: $M_s = 4.20$ (γ constant)

$P_{41} = 4 \times 10^4$: $M_s = 4.14$ (γ variable)

Such an effect on M_s should be swamped by other considerations as described in (b) and (c) above.

An important variable, the duration of the quasi-steady flow behind the incident shock is subject to real gas effects.

Roshko in ref.(5) has expressed the running time, t_i, at station x as a function of M_s and $\eta = \rho_1/\rho_2$, in an inviscid gas as:

$$t_i = \frac{x}{a_1} \cdot M_s(\eta - 1) \qquad \ldots\ (3.2)$$

The density ratio η is a function of the real gas properties and is plotted against M_s in fig.(3. 8) for various values of p_1, the initial pressure in the channel.

The consequent reduction in running time from the ideal perfect gas value is expressed as a percentage of the ideal value and plotted against M_s in fig.(3. 9).

The loss of flow duration is small for the Air : Air case, but for a helium driven shock tube the loss is by no means negligible and must be considered.

The real nature of the channel gas manifests itself in another very important result. The translational and rotational modes relax to equilibrium conditions in a very few collisions, consequently the shock front may be considered to be infinitesimally thin, except at very low pressures. The higher modes, however, take several hundreds of collisions to relax and thus, at high temperatures and low pressures the relaxation time may well be of the same order of magnitude as the duration of steady flow. In these circumstances the gas will not then attain equilibrium.

The non-ideal behaviour of the driving gas may affect the shock tube problem in the case when a cold driver is expanded to very low pressure. In air if the initial pressure ratio P_{21} is of the order 10^5, then as a result of the

expansion, the nitrogen and oxygen components should have liquified. Information as to how this would affect the shock motion is not available. It is contended, however, that the low temperatures predicted are not attained, because of the viscous properties of the driver gas.

(b) VISCOUS EFFECTS.

Loss of Flow Duration.

The development of a boundary layer behind the incident shock wave has proved to be one of the greatest problems encountered, when one attempts to study chemical reactions, relaxation times, etc., in a gas at low pressure in a shock tube.

The shock wave attenuates rapidly when the boundary layer occupies much more than 10% of the tube cross-section. The duration of the quasi-steady flow, in which one can make such studies, decreases rapidly, as the boundary layer thickens.

If the boundary layer is thick, then any technique of measurement, which relies on the integration of a gas property across the tube, eg. electron beam densometry, will be subject to error, because the assumption of one-dimensional flow is no longer valid.

Likewise if studies are to be carried out in the region behind the reflected shock, then the interaction of this wave with the boundary layer will lead to a marked variation of the flow properties at a fixed station, with both time and position, refs.(6) and (7).

In treating the flow duration problem, Roshko's analysis, ref.(5), will be employed.

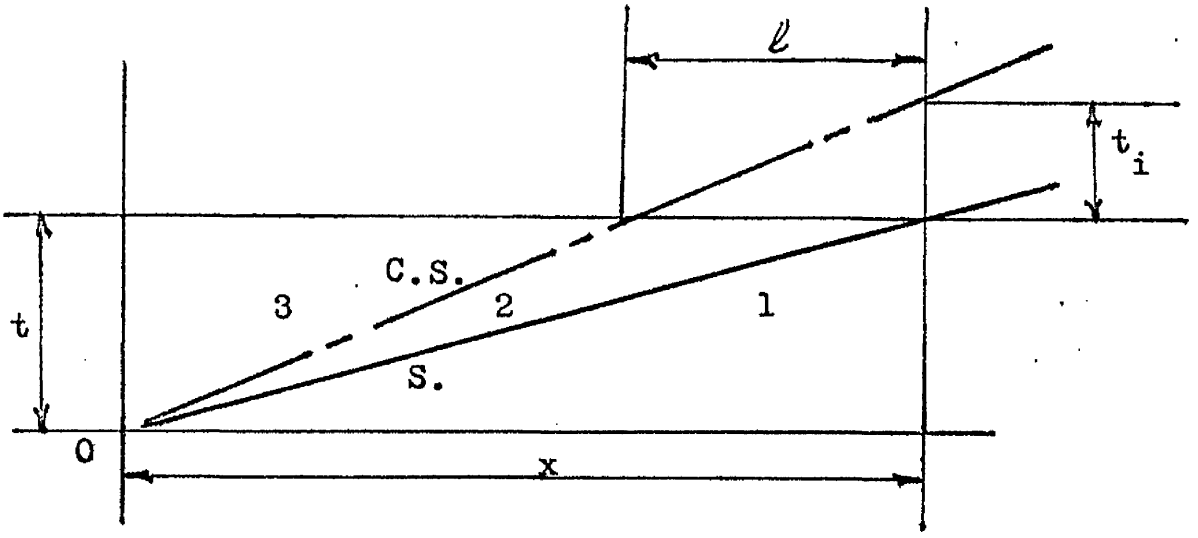

Fig.(3. 1)

Fig.(3. 1) is the x-t diagram illustrating the shock and contact surface trajectories, following an instantaneous diaphragm burst. The length ℓ is that of the shock processed gas available at station x. If the fluid is inviscid, there is no loss of shock processed gas and the relation,

$$\rho_2 \ell = \rho_1 . x,$$

holds true. The flow duration t_i at station x will then be given by equation (3. 2).

Roshko now postulates that the loss of running time resulting from the development of a boundary layer may be attributed to gas leakage past the contact surface through the boundary layer.

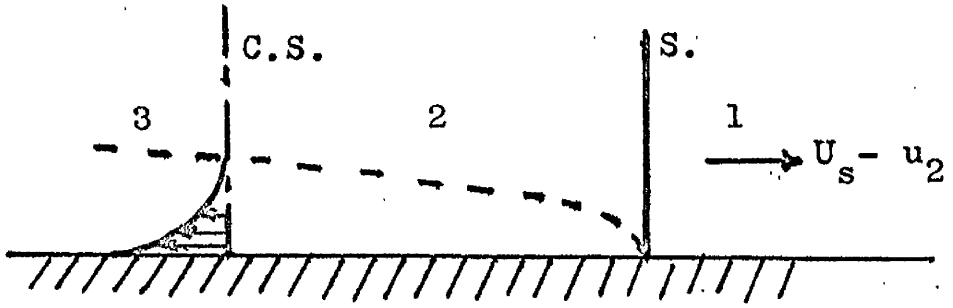

Fig.(3. 2)

Fig.(3. 2) illustrates the explanation and is drawn with the velocities relative to a stationary contact surface.

The relation describing the rate of increase of ℓ with time t, is then

$$\frac{d\ell}{dt} = \frac{u_2}{(\eta - 1)} - 4 \cdot \frac{\rho_w}{\rho_2} \cdot \frac{u_2}{d} \cdot \frac{\mu_w}{\rho_w . u_2} \cdot \ell^{\frac{1}{2}} \quad \ldots(3.\ 3)$$

when the boundary layer is laminar. The first term is the solution in the ideal case, whilst the second term describes the reduction in the rate of increase of ℓ caused by the boundary layer.

The maximum value of ℓ, which we shall call ℓ_m, is obtained from equation (3. 3) by $d\ell/dt = 0$, and knowing ℓ_m, one can evaluate t_m.

The differential equation (3. 3) is solved in terms of the non-dimensional variables,

$$T = \frac{t}{t_m} \quad \text{and} \quad X = \frac{x}{\ell_m} \ ,$$

yielding the solution,

$$\frac{X}{2} = - \ln.(1 - \sqrt{T}) - \sqrt{T}, \qquad \ldots.(3.\ 4)$$

in the viscous case and

$$X = T_i,$$

in the ideal case.

Relative flow durations are plotted in fig.(3. 10), using Roshko's values for the constant parameters. Real gas effects are included and also plotted is the inviscid real gas duration.

The Boundary Layer.

The boundary layer becomes so thick at low pressures that it is essential to have at least an indication of its relative importance as conditions in the chan-

nel are varied. This problem has been tackled by a number of investigators, notably Trimpi and Cohen in ref.(8); Demyanov in ref.(9) and Mirels in refs.(10) and (11). The method of the last named will be adopted to predict the boundary layer thickness and the resultant shock attenuation.

Mirels develops expressions for the boundary layer thickness behind a stationary wave on a moving wall.

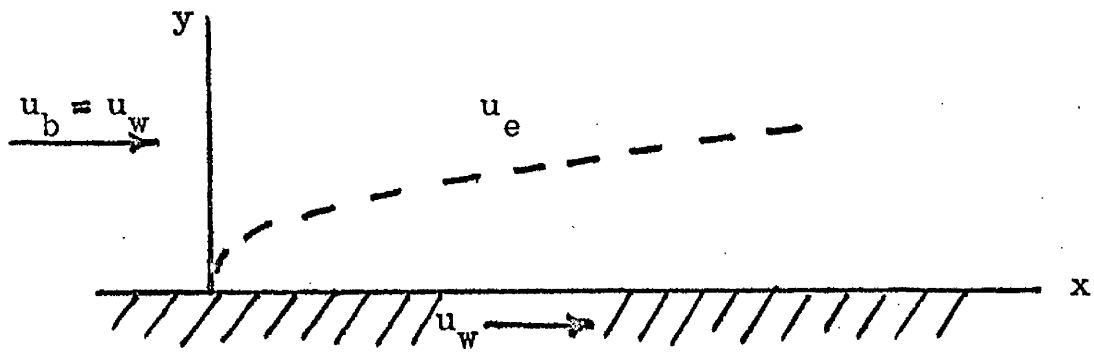

Fig.(3. 3)

The co-ordinate system for the shock wave case is shown in fig.(3. 3). Suffix b refers to conditions ahead of the shock and thus u_b = shock velocity, in the shock tube case. Suffix e refers to conditions outside the boundary layer and downstream of the shock. The laminar boundary layer fluid velocity thickness is given by the value of y corresponding to the condition,

$$\frac{u - u_w}{u_2 - u_w} = 0.99$$

Equation D.5 of ref.(11) provides an expression for δ_2, in the region 2, behind the incident shock and has been evaluated at the contact surface. Fig.(3. 11) is taken from this work and shows the relationship between $2\delta_2/d$ at the contact surface and the incident shock Mach No. The boundary layer thickness is greatest at the contact surface and hence this is the limiting value for δ_2.

The assumption of a completely laminar boundary layer will only be valid at low pressures and if the tran-

sition Reynolds No., Re, based on δ_2, is taken as 0.5×10^6, then the limiting pressure may be found from fig.(3. 12). This is based on equation H.3 of ref.(11).

The evaluation of the shock attenuation produced by a laminar boundary layer in a shock tube demands a knowledge of the viscous flow from the head of the expansion to the shock front. To make the problem tractable, Mirels was forced to adopt a model involving a shock expansion, instead of the actual expansion wave. This simplification is reasonable for moderate expansion ratios. The validity of the solution is doubtful in the case of the 12"x12" tube, since it is normal practice to operate with large diaphragm pressure ratios. Mirels' results will, however, indicate the order of magnitude for the shock attenuation, which may be anticipated.

To evaluate the attenuation of the shock wave stemming from the boundary layer, Mirels assumes the flow in the tube to be ideal, with small superimposed perturbations due to the boundary layer.

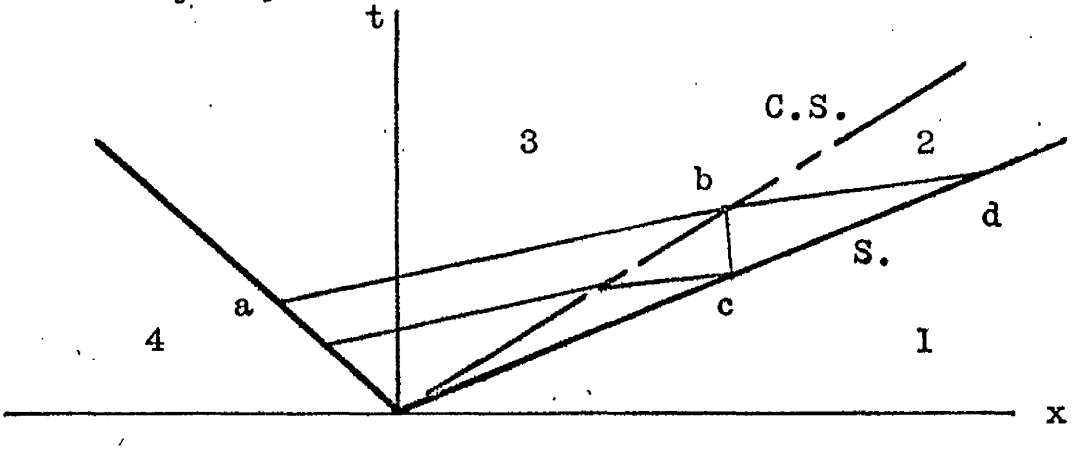

Fig.(3. 4)

The major contribution to shock attenuation comes from the characteristics bd, bc, and ab. The reflected characteristics at c do not contribute a great deal and will be neglected. The small perturbations are integrated along the characteristics and the pressure reduction at point d is obtained from equation (6) of ref.(11), for the laminar case.

Using Mirels' data for the Air : Air shock tube the nett attenuation is plotted against ideal M_s in fig.(3. 13) for various values of p_1. In fig.(3. 14) the shock strength M_s given by the pressure ratio $(p_2 - p_1)/p_1$ has been plotted against ideal M_s.

EFFECT OF DIAPHRAGM OPENING

In this section a brief survey of the problem is made, with particular reference to the conditions in the 12"x12" shock tube. A fuller discussion of the theoretical diaphragm performance and some experimental data is included in Chapters 5 and 6, respectively.

Two investigators, White ref.(13) and Kireyev ref. (14) have made theoretical approaches to the problem.

Fig.(3. 15) illustrates the "shock formation distance", $\triangle x_f$ as defined by White and it has been plotted for representative values of P_{41}. The accuracy of White's method has been improved by including additional characteristics, corresponding to $P_{41} = 10^2$, 10^3, and 10^4. This means that the formation distance given by fig.(3. 15) will be equal to the value obtained with White's analysis for $P_{41} = 10^2$, but the results for higher values of P_{41} should be more realistic. The opening time, t_w, is given as $1/a_1$ and the value of $\triangle x_f$ is proportional to t_w. The times taken by the final compression wave to reach the tail of the expansion and the contact surface are also included. Fig.(3. 16) shows the x-t diagram in the case $P_{41} = 10^3$.

The implications of fig.(3. 15), in the light of the measured diaphragm opening time $t_w \doteqdot 1$ millisecond, were such that it became necessary to examine the opening process in greater detail.

Plate I, which is taken from ref.(15), shows the formation of "standing shock waves" in the vicinity of the petals. Pressure and entropy will be increased immediately downstream of these shocks. The theoretical analysis, Chapter 5

attributes their existence to being a result of the motion of the petals relative to the walls of the tube.

The existence of forward facing secondary shock waves moving downstream of the diaphragm has been implied from heat transfer recordings of the type, shown in fig.(6, 13). The speed of a forward facing shock wave through the tail of the expansion wave is given by,

$$w = u + aM_s,$$

which should be compared with that for a compression wave, viz.,

$$v = u + a.$$

Since the strength of the shock wave will increase as it proceeds through the expansion, the formation distance should be reduced by its prescence.

The interaction between two forward facing shocks is treated by Rudinger, ref.(16). The wave diagram obtained in this case is shown below in fig.(3. 5).

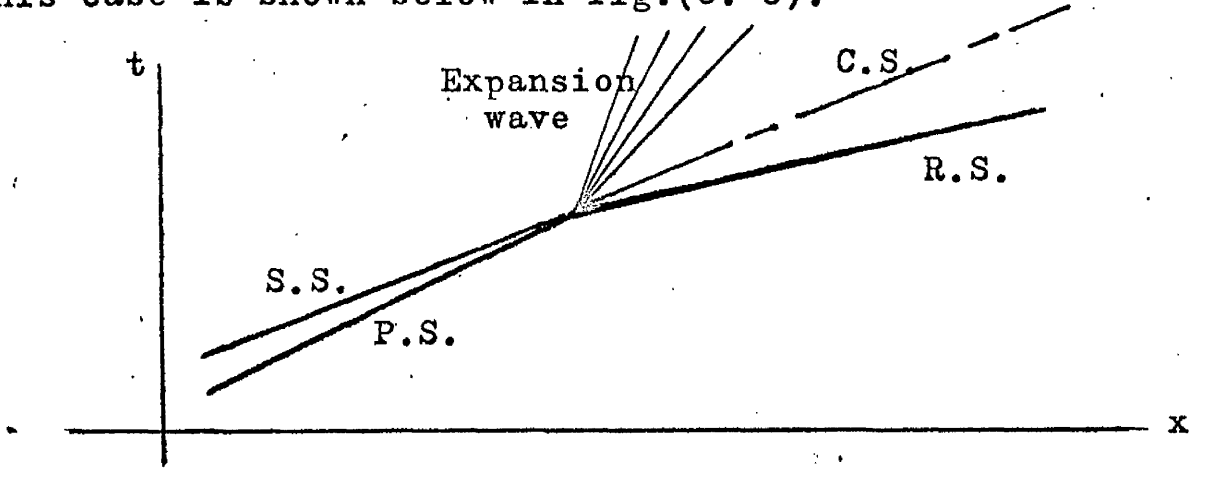

Fig.(3. 5)

The reflected wave is always an expansion for a real gas. If one knows the strength of the two shocks, then the problem may be solved by iteration. This wave diagram is the same as that obtained in a shock tube with instantaneous

removal of the diaphragm.

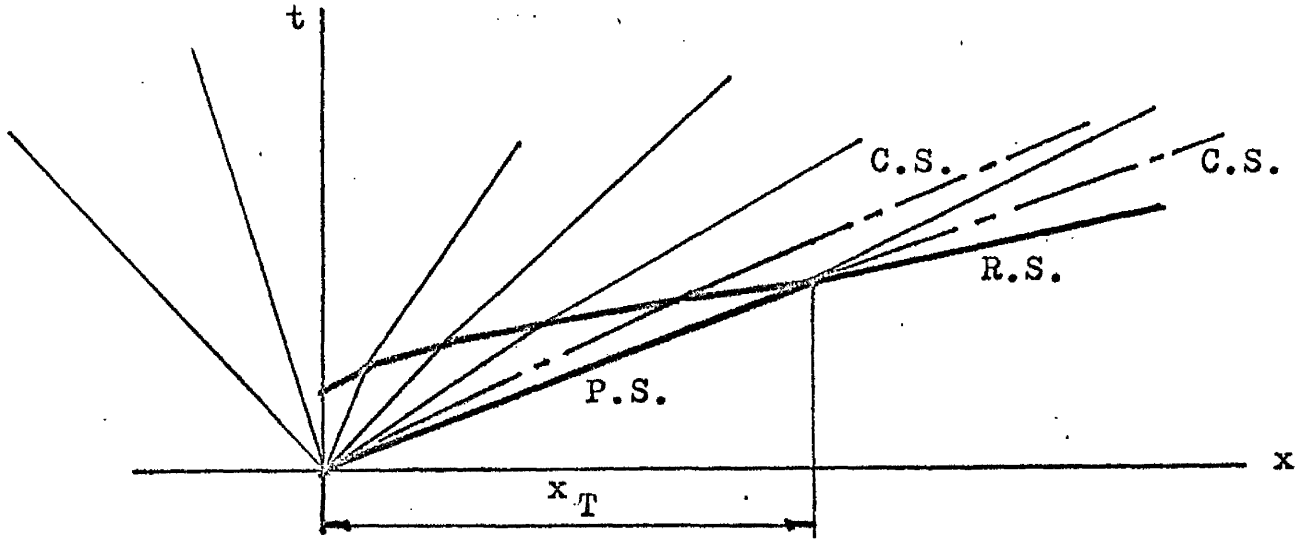

Fig.(3. 6)

Fig,(3. 6) shows the transitory wave diagram obtained at the diaphragm, with a sufficiently strong secondary wave. The nett effect of this wave process is to allow an ideal shock tube analysis, with modified initial conditions:

(a) $x = 0$ at station x_T

and

(b) M_s is now the strength of the resultant transmitted shock wave, R.S.

The quasi-steady flow duration will now be terminated by the resultant contact surface and not the gas interface.

In an effort to determine the source of the observed secondary shock waves and consequently be able to assess whether they could be usefully employed to reduce the shock formation distance in the manner suggested above, a theoretical analysis was instigated; reported in Chapter 5, on the basis of ref.(14).

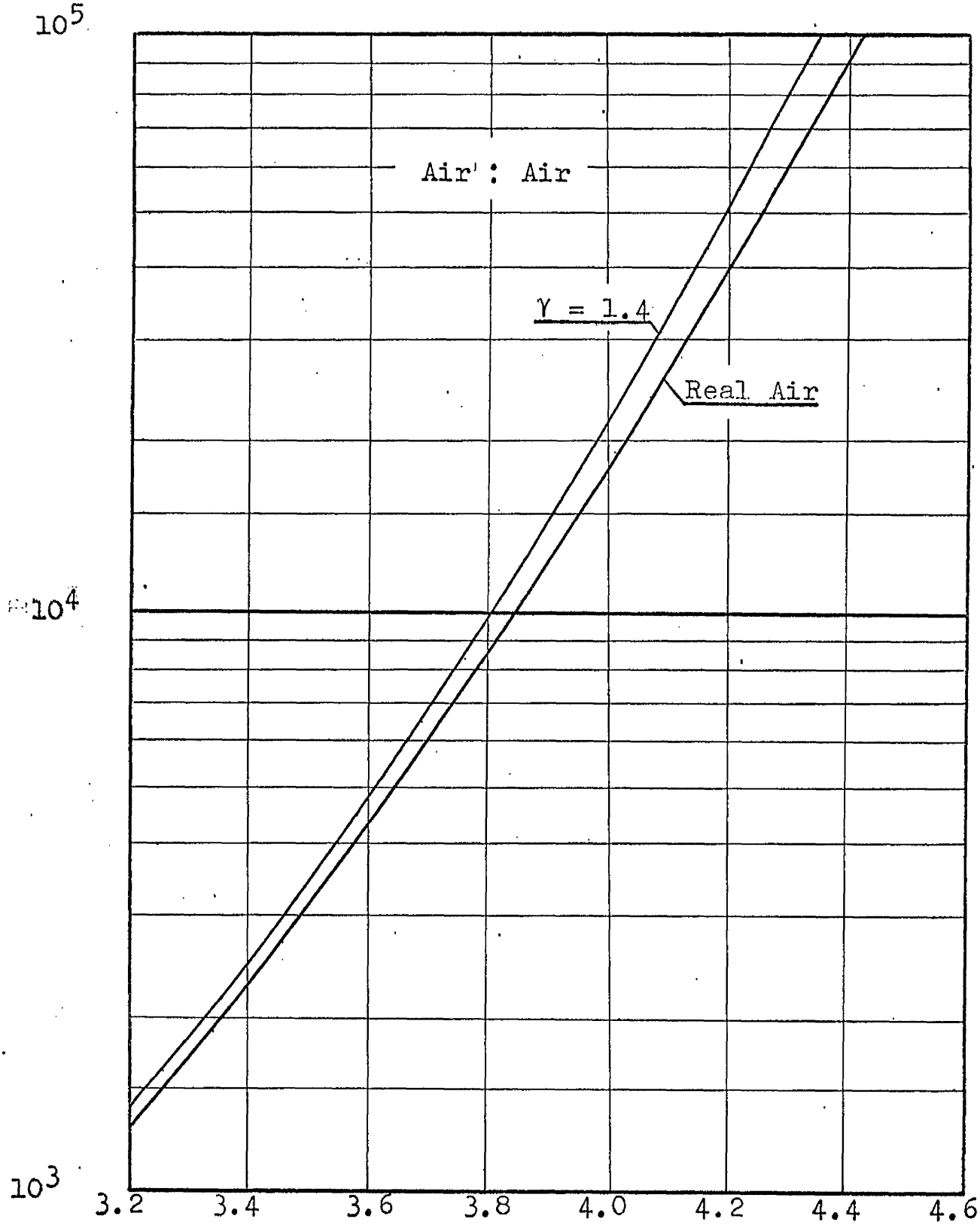

The Relationship Between the Shock Mach No., M_s and the Initial Pressure Ratio, P_{41}.

Fig.(3.7)

The Variation of Shock Density Ratio, η with Shock Mach No., M_s

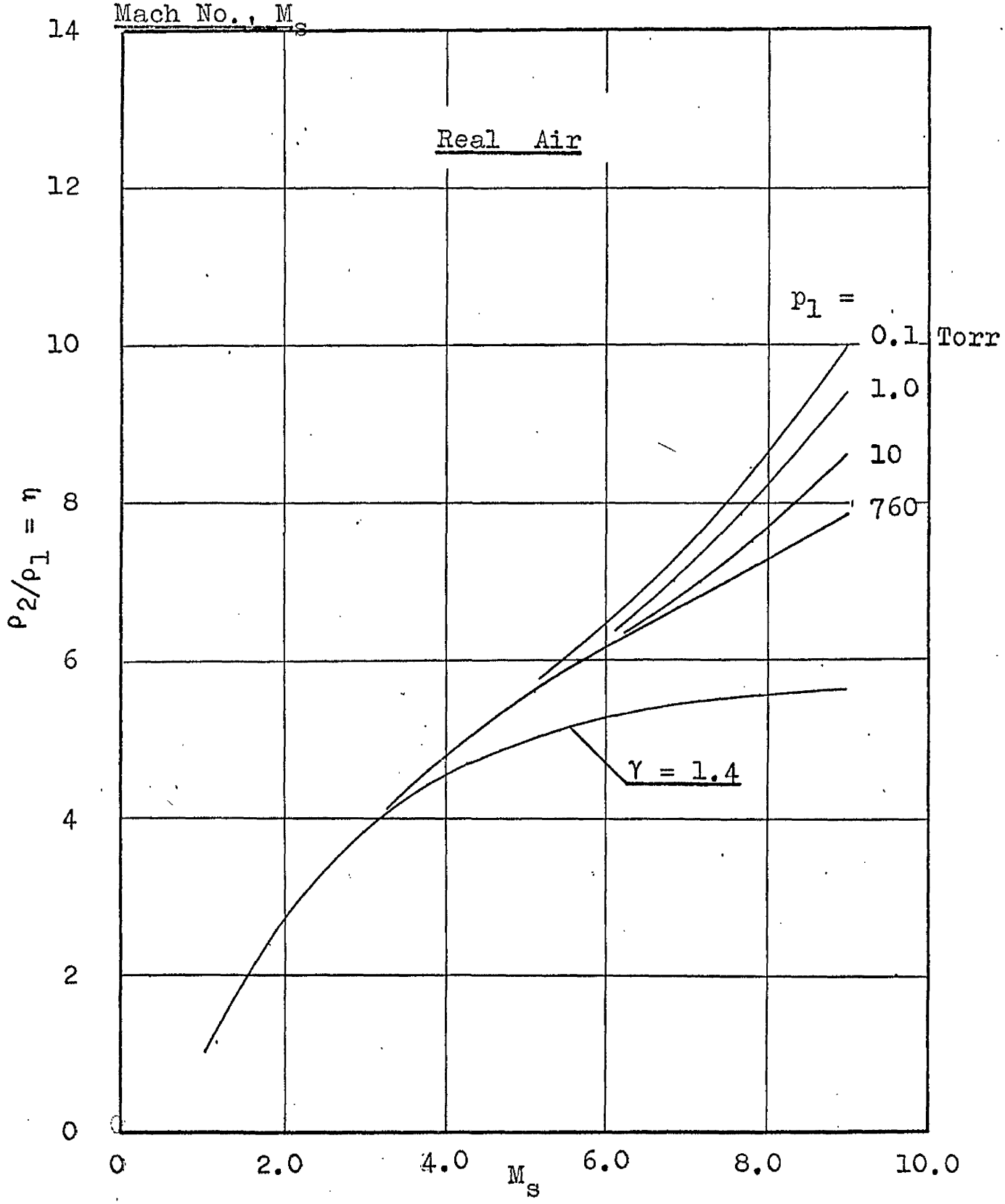

Fig. (3. 8)

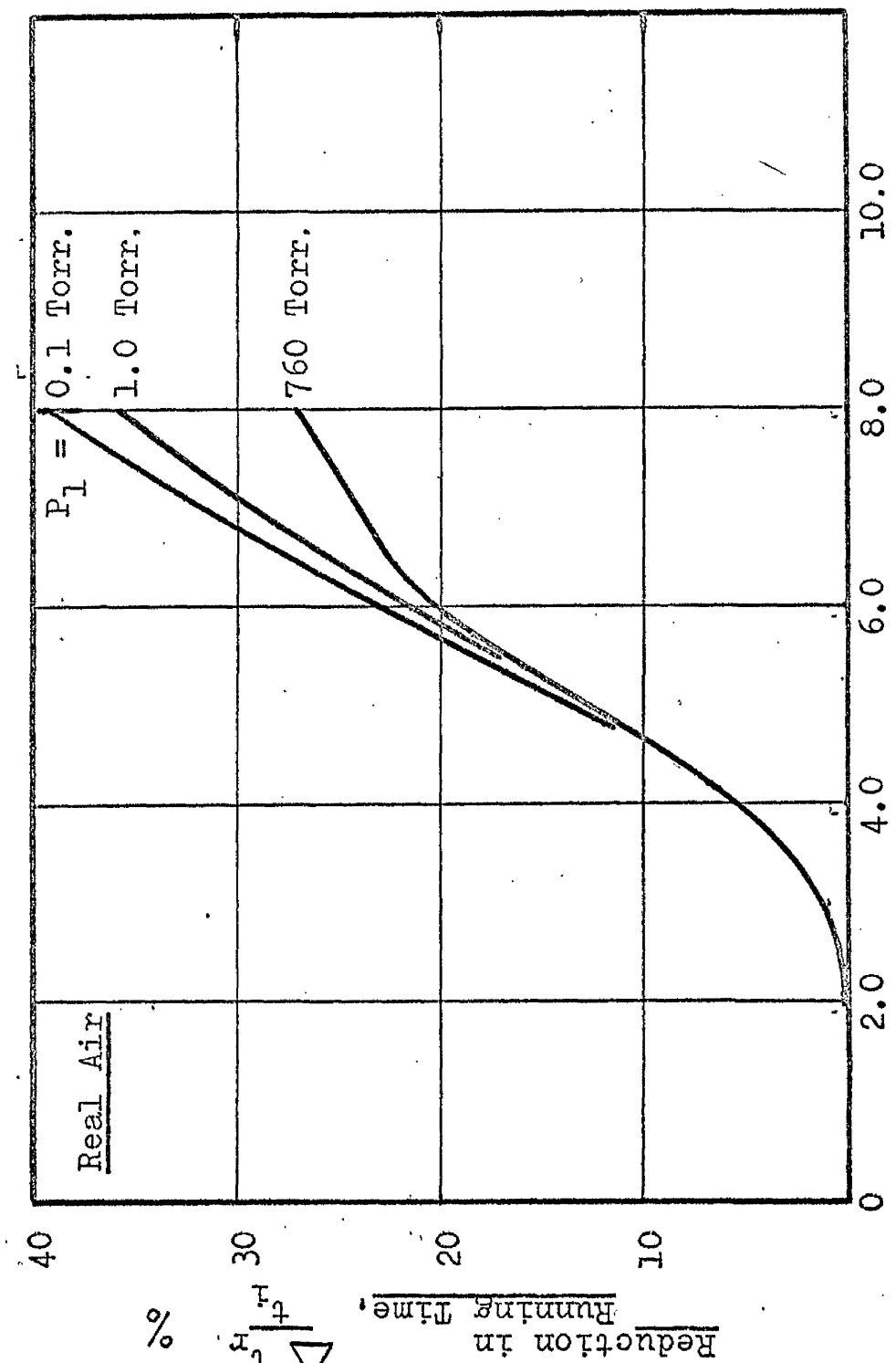

Fig.(3. 9) Loss of Flow Duration in an Inviscid Gas with M_s.

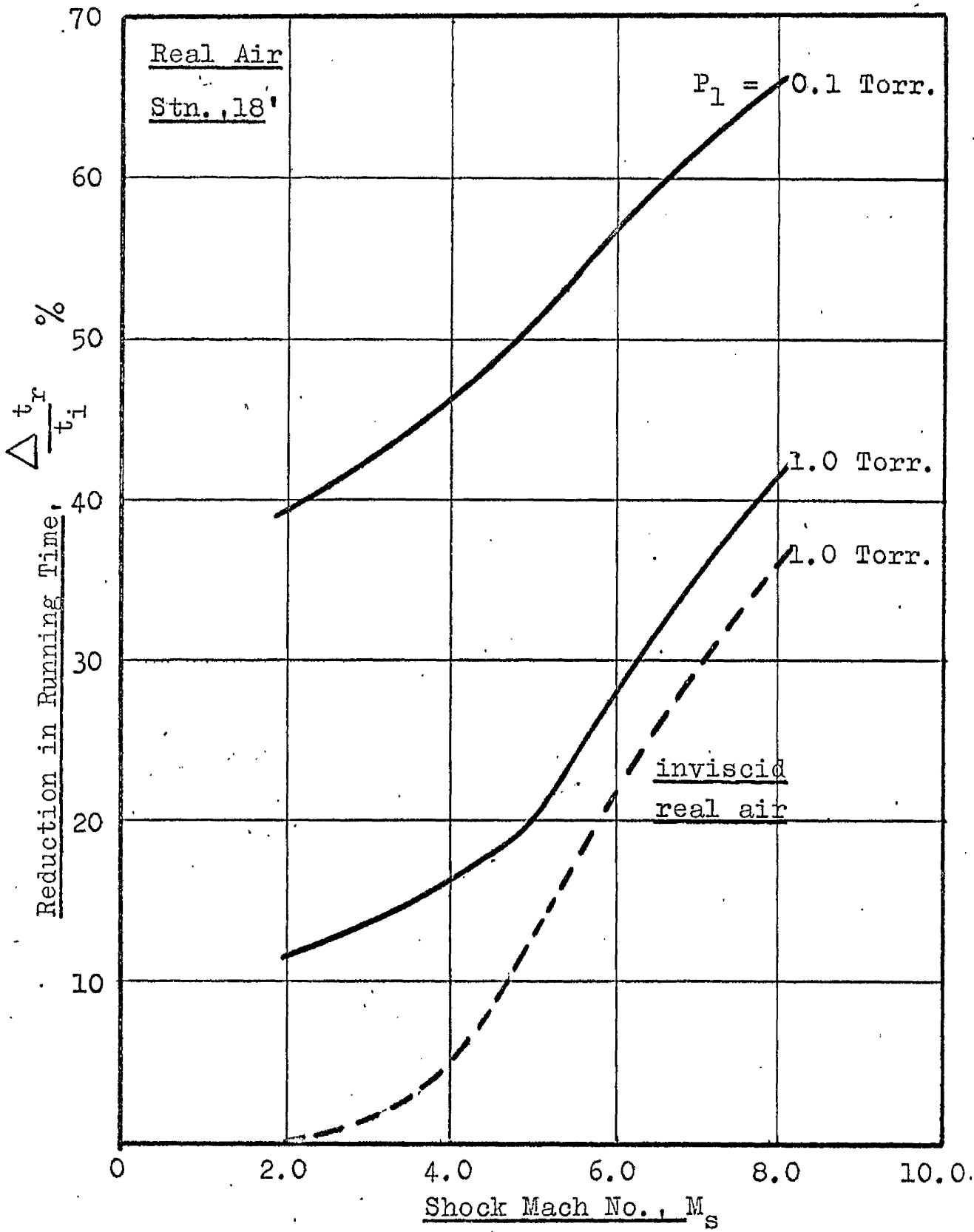

Fig.(3. 10) Loss of Flow Duration in Real Air with M_s.

Fig.(3.11), Variation of Laminar B.L. Re at C.S. with Ms

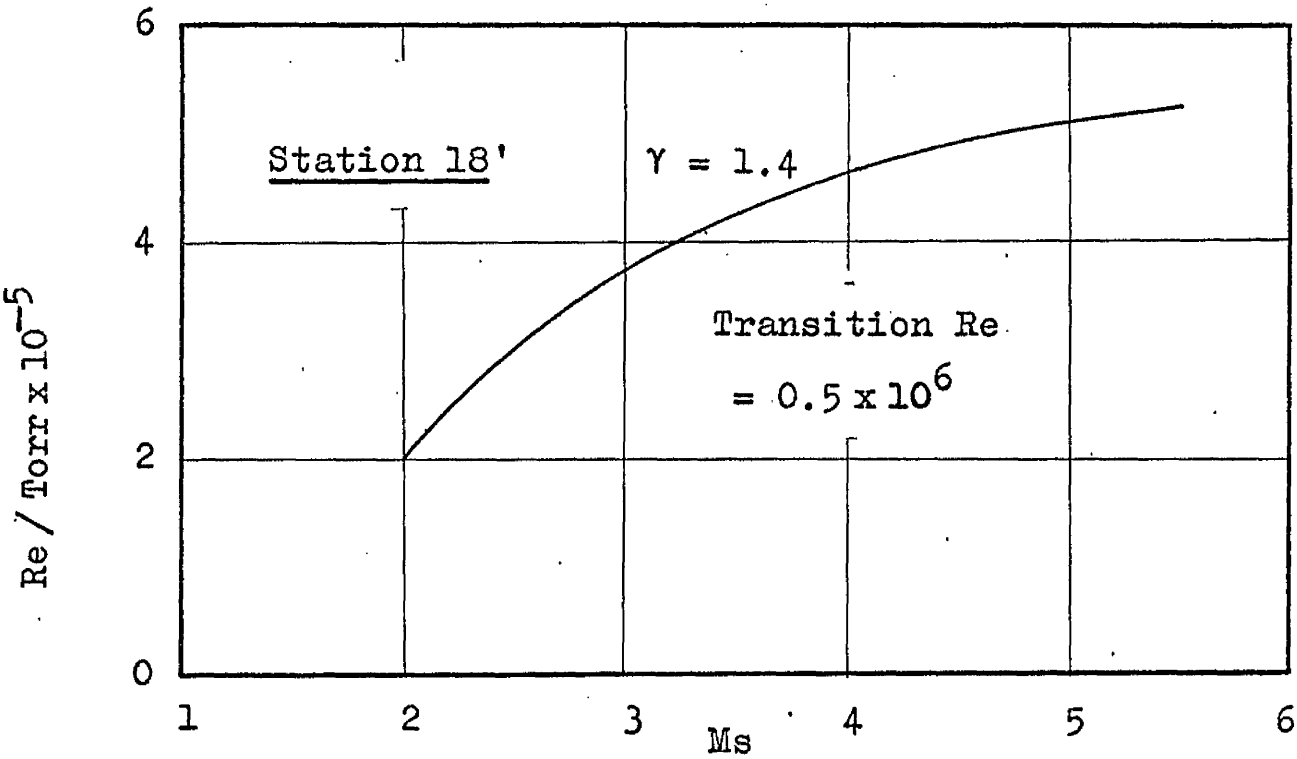

Fig.(3.12), Variation of Laminar B.L. Thickness at C.S. with Ms

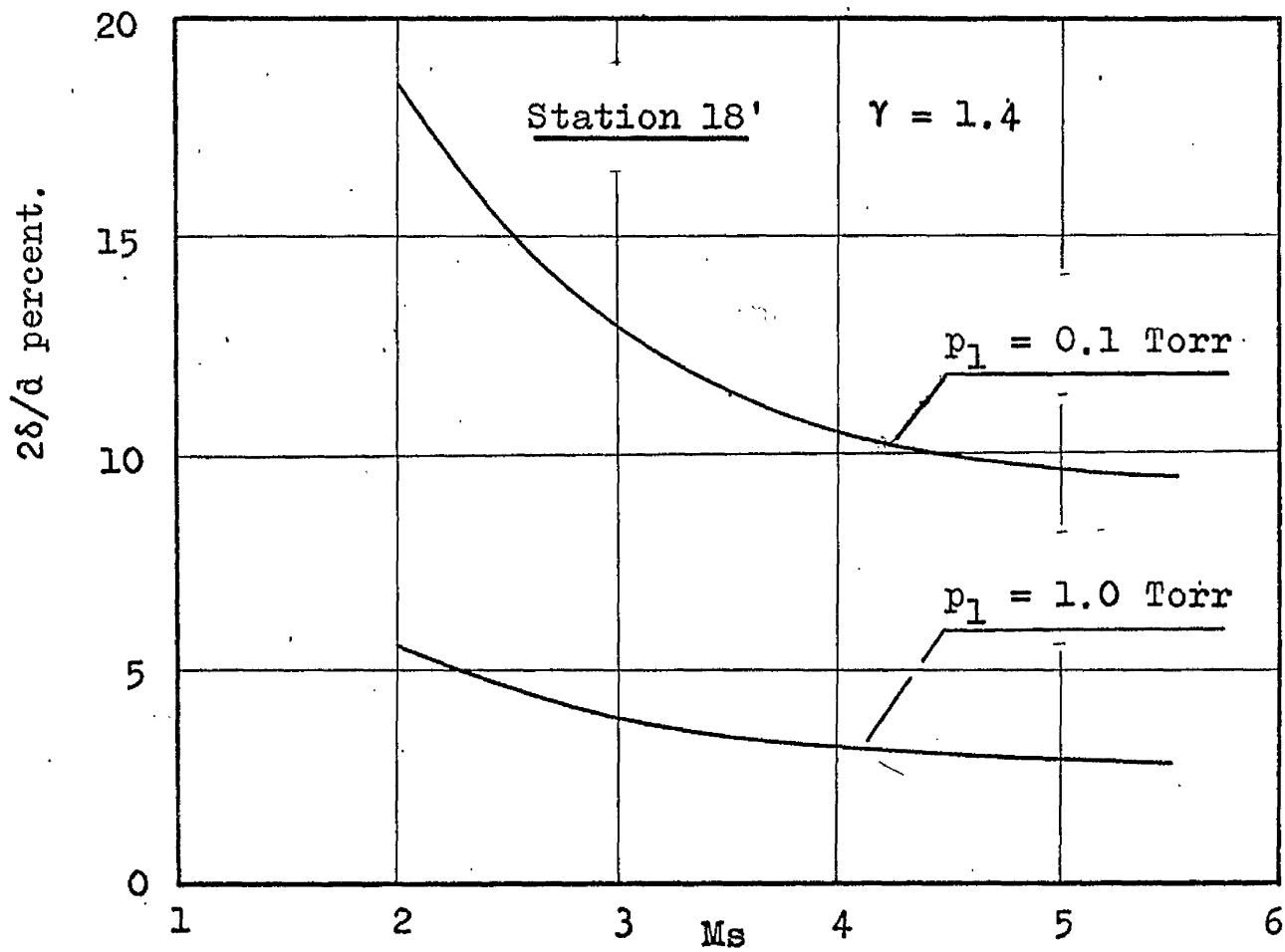

The Relationship Between $M_{s(attenuated)}$ and $M_{s(ideal)}$

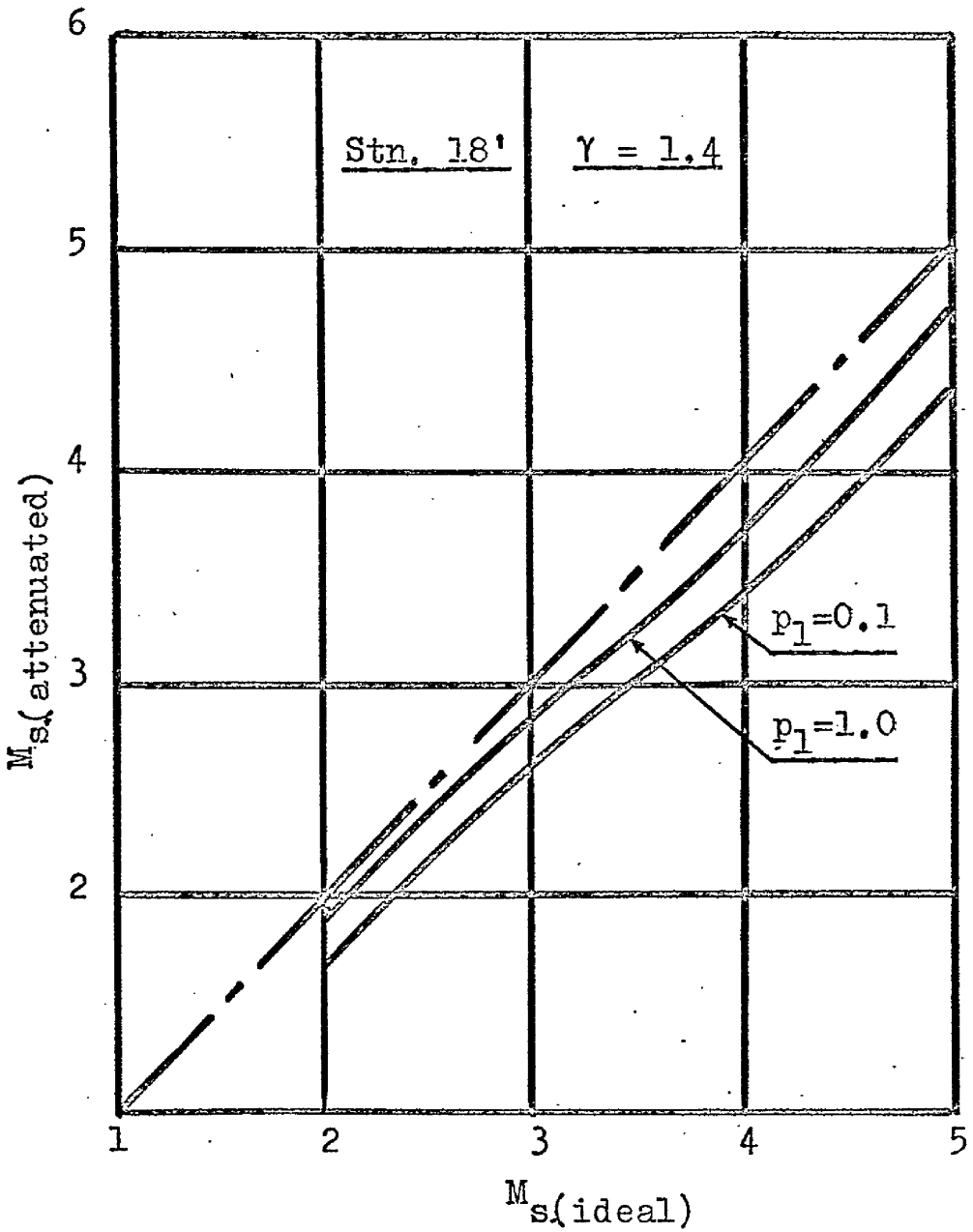

Fig. (3. 14)

Variation of pressure Attenuation with Shock Mach No. M_s

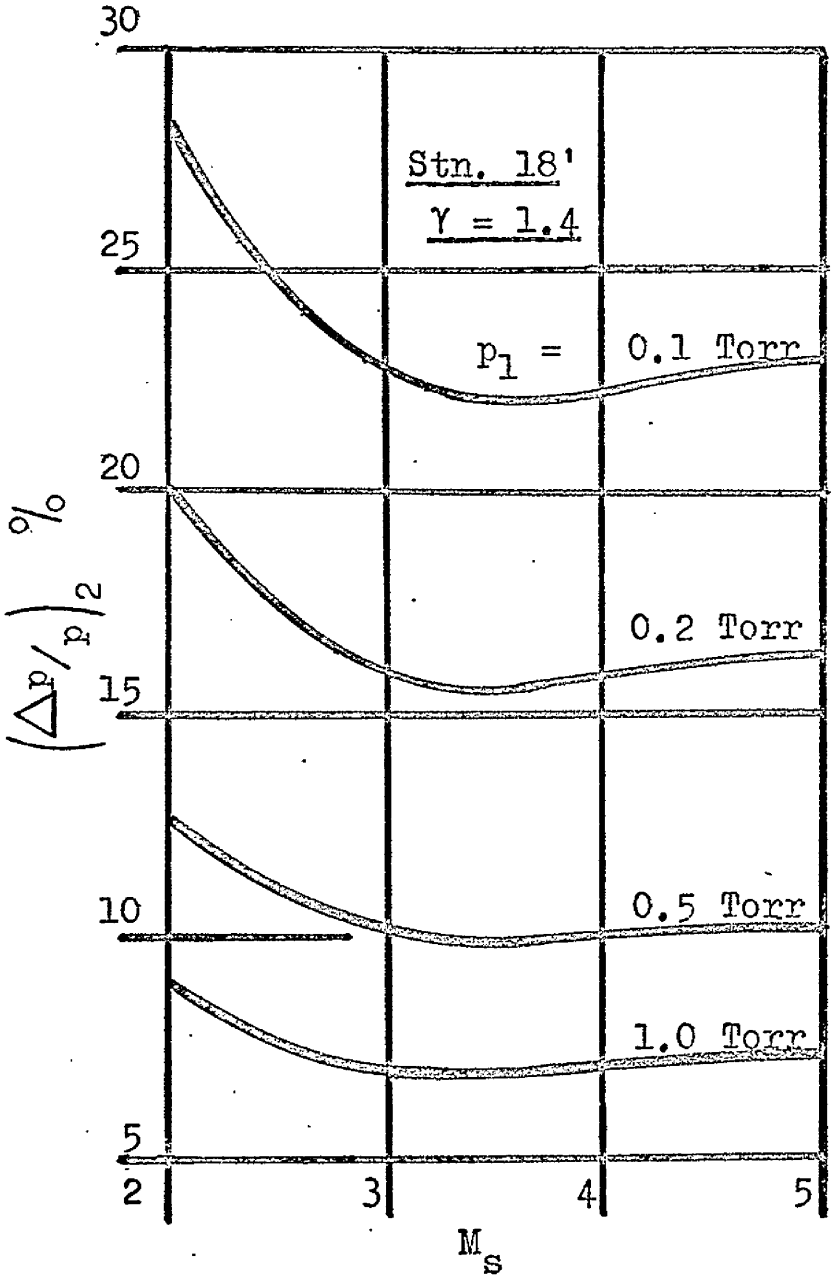

Fig. (3. 13)

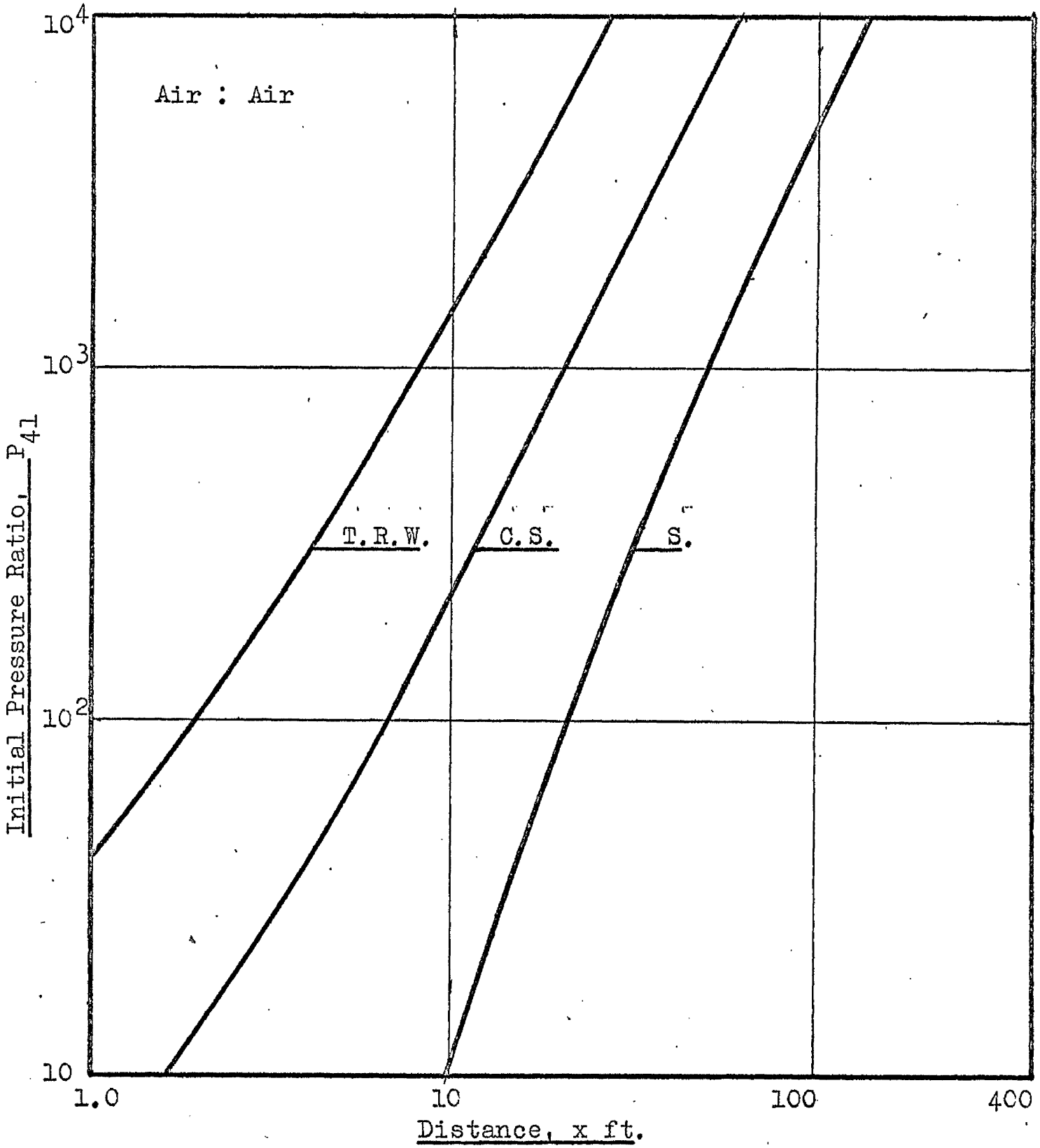

Fig.(3. 15) Location of the Points, where a Compression Wave, Leaving (0, $1/a_1$) meets the Primary Waves.

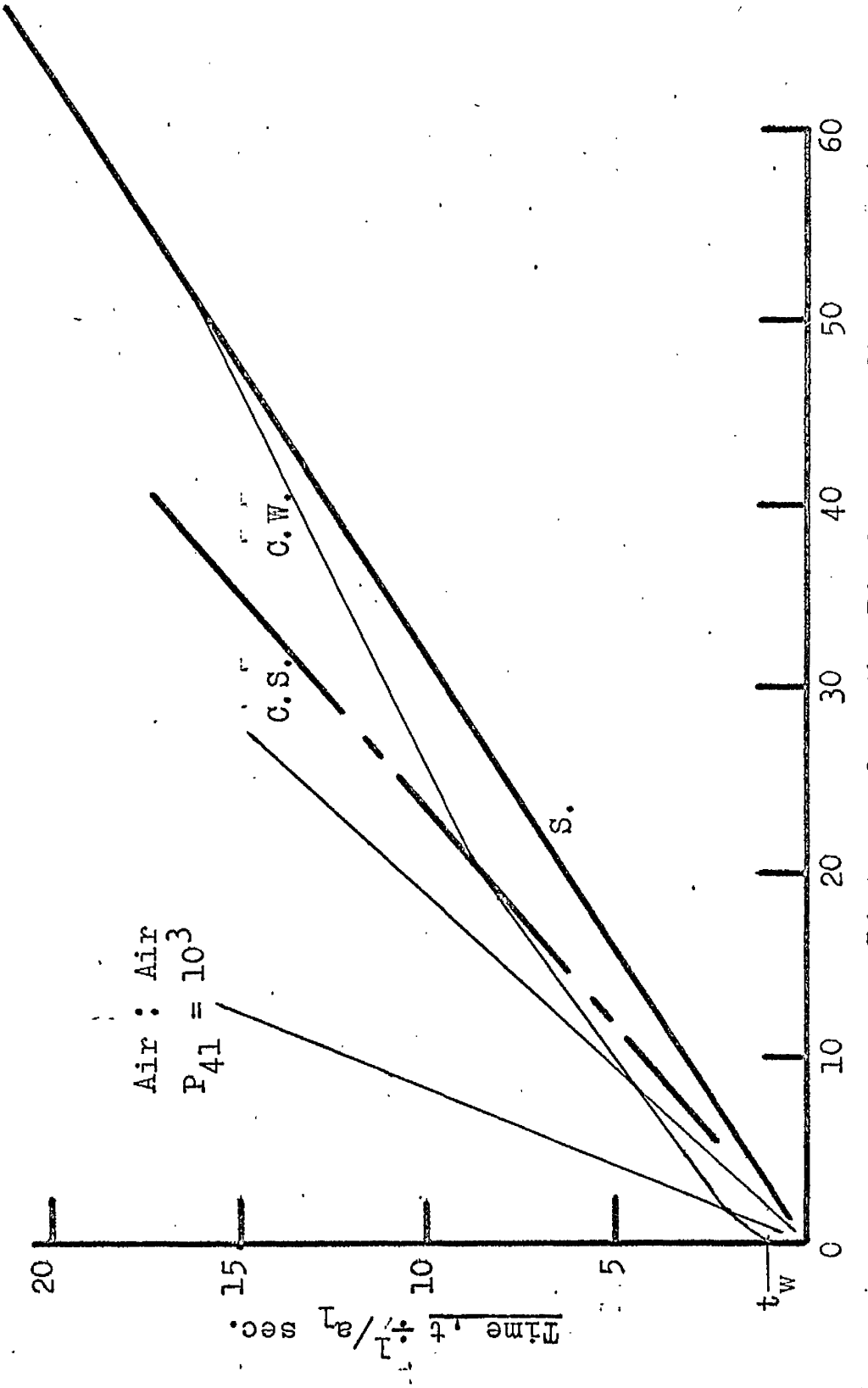

Fig.(3. 16), Trajectory of a Compression Wave Emanating from Stn.0 at time $t_w = 1$

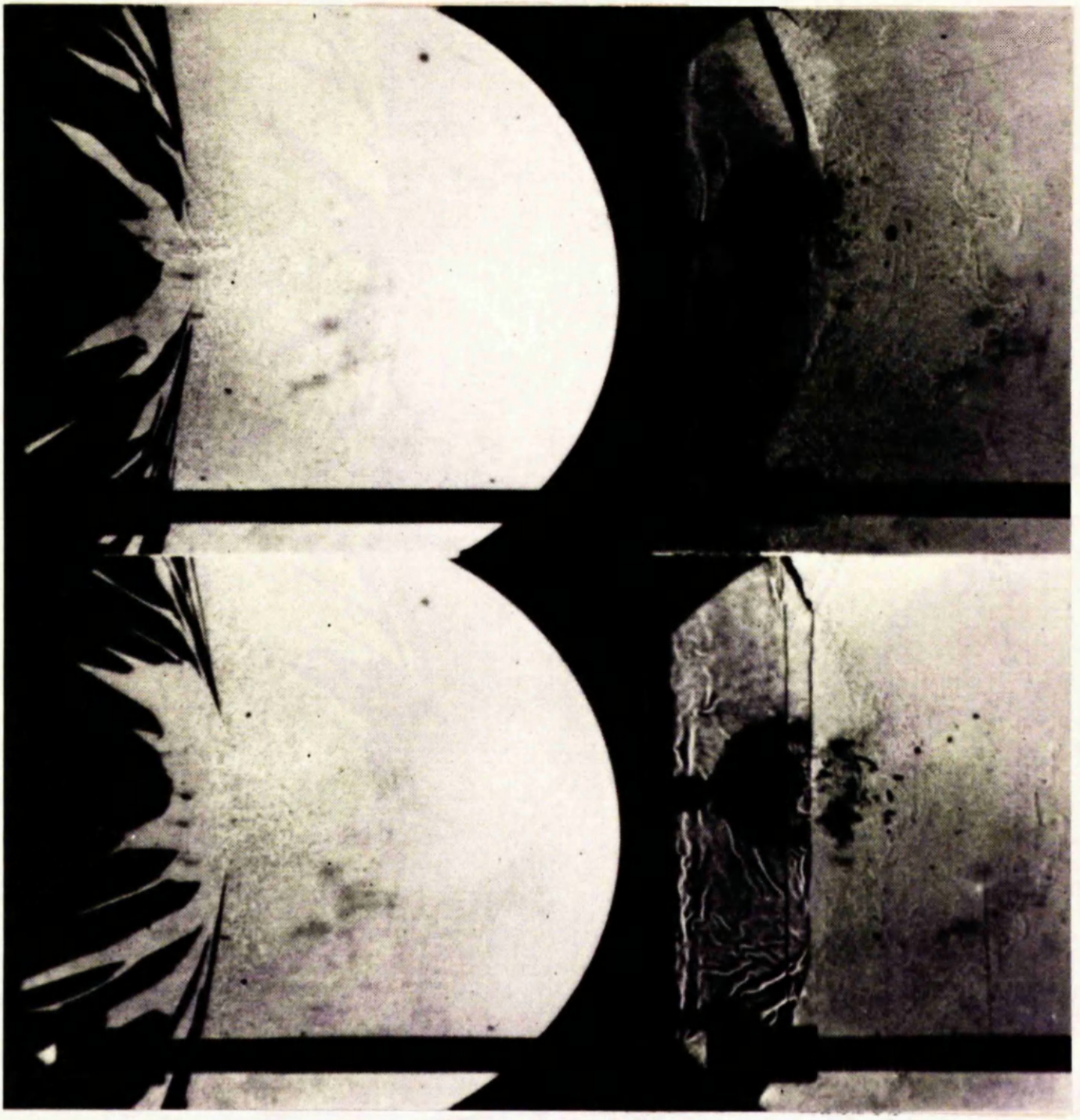

Reproduced from "Shock Waves in Chemistry & Physics"

Successive Flash Photographs of Shattering & Petalling Diaphragms.

PLATE I.

CHAPTER 4.

DESCRIPTION OF THE SHOCK TUBE AND ITS ASSOCIATED EQUIPMENT.

DESCRIPTION OF THE SHOCK TUBE AND ASSOCIATED EQUIPMENT

INTRODUCTION

The 12"x12" shock tube is a uniform tube, with a 4 foot long driver and a 20 foot long low pressure channel. These proportion are flexible and the main hydraulic clamp at the diaphragm station may be moved, fairly readily. The general arrangement is illustrated in fig.(4. 1) and in plate II.

STANDARD SECTION

The tube is built up from a number of individual sections, eleven of which are 2 feet long and the remaining two are 1 foot in length. Nine of the 2 feet long sections are the same and the design is illustrated in fig. (4. 2). This type of section is used in both high and low pressure sections of the tube and the whole tube has been designed to withstand an internal gauge pressure of 250 psi. The sections are fabricated from four rolled steel angles, butt welded along the centre lines and stiffened externally with 'T' section members. Heavy flanges are welded to each end, one of which is grooved to receive an 'O'-seal.

Owing to an error made in the original fabrication, it was necessary to reduce the internal dimensions to $11\frac{3}{4}$"x$11\frac{3}{4}$", in order to maintain a specified wall thickness of $\frac{3}{4}$". The tolerance called for on the bore dimmansions, viz. plus or minus 2 thousands of an inch, was not met and it proved necessary to scrape the sections, over a 6 inch length at each end, to the specified size, in order to eliminate any step at the interfaces

To ensure interchangeability all the flanges were jig drilled and two holes in each face are located to within 0.0002 inch. Fitted bolts in these holes ensure accurate alignment of one section with another.

The sections were machined internally in a slotting machine, which resulted in some surface marking. Subsequent hand finishing reduced this to,an acceptable level. The sections were finally electro-tinplated, a coating which has proved suprisingly robust. Tinplating was adopted as a second choice, after it proved impossible to deposit a satisfactory nickel coating.

The nine standard sections have a $1^{1}/_{16}$ inch diameter hole drilled in one wall, located as shown in fig.(4. 3). These holes permit the insertion of heat transfer gauges, pressure gauges, (S.L.M.), or any other transducers, which may be fitted into the space available. The high pressure lines, vacuum gauges, etc. are all connected to the tube through standard holes, with the exception of the main vacuum line, which requires a 2 inch diameter port. This has been provided in the channel end plate, the main isolation valve being bolted directly onto this plate.

NON-STANDARD SECTIONS.

Two non-standard sections, besides those 1 foot long, are incorporated in the channel. One, termed the "working section" is illustrated in fig.(4. 4). This section has apertures machined in the walls, into which schlieren quality windows, or special purpose panels, may be fitted. The windows are $1\frac{1}{2}$ inches thick and permit observation of the flow from the floor to the roof of the tube over a 4 inch wide field of view. Panels have been made, which allow the mounting of stagnation probes transversely across the tube. Standard tapping holes are drilled in the centre of each panel, which is of perspex, thus simplifying the problem of isolating one end of a heat transfer probe from the other.

The second non-standard section differs from the standard type, only in having three additional tapping holes located as shown in fig.(4.3). This section is primarily intended to provide;

(a), tapping holes for the measurement of shock velocity, with thin film shock detectors mounted in the foremost and aftmost locations and

(b), a means of detecting tilting of the shock front in relation to the vertical plane, with shock detectors mounted in the centre positions.

This section is particularly useful when the flow at the wall is observed with a transducer mounted in one or other of the centre holes, since in these circumstances the average shock velocity measured, as in (a), will refer to the transducer position.

THE HYDRAULIC CLAMP

The hydraulic clamp, illustrated in plate III, facilitates diaphragm changing. The diaphragm is retained by the action of the knurled ring biting into it, under the pressure of the clamp. Sealing on both sides of the disc is effected by 'O'-rings. This simple system, which may be fitted at any interface, holds the diaphragm effectively, maintaining a gas tight seal under all conditions. Fig.(4. 5) shows a section through one piston and lever assembly. The hydraulic load on the piston is transmitted by the lever - ratio 1:1 - to the low pressure flange. Return springs, not shown, return the lever when the pressure is released. The piston motion is governed by the cam form of the lever. There are sixteen such assemblies spaced around the flange, one between each bolt hole. The clamps normally operate at a pressure of 6,000 - 7,000 psi. and apply a load of about 3½ tons at each position, allowing a factor of 2 on the 'break open' load of 28 tons. The hydraulic system is designed for a safe pressure of 10,000 psi. and the weakest members, viz. the levers, have a reserve factor of 4 at this pressure

A measure of safety against a failure in the hydraulic system is provided by hand tightening nuts on two

bolts after the clamp has been pressurised. It is not intended that the tube should remain gas tight in the event of a hydraulic failure. The bolts will, however, prevent the tube from 'flying' apart, whilst the gas in the high pressure chamber leaks out into the laboratory. The chance of such a failure occuring necessitates the precaution of ensuring that personnel keep clear of the diaphragm station, whilst the tube is pressurised.

RECOIL SYSTEM AND SUPPORTING STRUCTURE.

The general arrangement, fig.(4. 1) shows the manner in which the shock tube is supported. The channel length is suspended from above and is free to move. To equalise the loads on the rail, a "Metalastik" cylindrical rubber shear bush is incorporated in each hanger assembly, see fig.(4. 6). Individual adjustment is provided by the turnbuckle. The design relies on the machining of the individual shock tube sections to ensure that the tube remains straight as it is assembled.

The high pressure chamber is also carried by rubber mountings, fitted between it and the sub-frame. The primary function of these mountings is to reduce the recoil load to a value, which the structure can withstand. The recoil load is evaluated by the method of ref.(17). No account is taken of the relief afforded by the reflection of the shock wave at the channel end plate. This allows the addition of a dump chamber at a later date, without reconsidering the recoil system. The recoil system has been designed on the basis of driving with air at pressures up to 250 psig. Lighter gases may also be used in the driver without incurring restrictions, other than the static limit of 250 psig.

To corroborate the design figures, measurements of both the accelerations and the displacements developed

by the tube, following diaphragm rupture, were made. Typical oscillograms are shown in figs.(4. 7) - (4. 9). The wave reflections account for the difference between the maximum measured displacement of 0.06 inches and the design figure of 0.5 inches. The peak acceleration is not affected by the reflection of the shock wave and good agreement between the measured and predicted values is observed.

The rail, from which the shock tube channel is suspended, is supported by two large viriendal trusses, the static load being transmitted through this structure to two transverse floor beams. The dynamic loads are fed from the sub-frame into the trusses and reacted at the floor. This type of structure allows maximum unobstructed access to the tube and has been designed to withstand the maximum recoil load in conjunction with the static load.

THE VACUUM SYSTEM.

The shock tube channel has a capacity of 20 cubic feet and the measured rate of pressure rise, when closed off at the ultimate vacuum, ie. 0.05 Torr, is 7 - 8 microns per minute. This high apparent leak rate is largely attributed to outgassing, principally from the welded joints, where pockets have been detected. These pockets are invariably connected to the inside surface of the tube by minute pinholes and the nett result of this is that large quantities of air are drawn into the channel, when the pressure is low, ie. when the mass flow in the pump is small.

In order to obtain the quoted leak rate, the undernoted measures were taken.

(a) All the minute pinholes, which could be found, were opened out with a drill and the enlarged holes were then plugged with epoxy resin.

(b) A Halogen Leak Detector was employed to find external leaks and any so detected were sealed with 'Araldite'.

(c) Finally all the exposed welds were painted with

'Araldite', whilst the tube was held at low pressure.

All the flanged joints are sealed with 'O'-seals and care has been taken in the design and assembly of these joints to avoid forming pockets, which would behave in a like manner to those in the welded joints.

The vacuum pump used is the Leybold S.60, which evacuates the tube to a pressure of 1 Torr in less than 7 minutes. The ultimate pressure, 50 microns, that can be attained, is the limit quoted by the pump manufacturer.

The channel pressure is normally measured with,

(a), a diaphragm vacuum gauge, which measures total gas pressure against a "zero" reference pressure and has a useful range, 50 - 1 Torr;

(b), a Pirani Gauge, which has a working range, 10 - 0.01 Torr.

In addition there is a Miniature MacLeod Gauge, which when used in conjunction with the 'Pirani' enables one to make a qualitative assessment of the vapour concentration in the channel.

The high pressure chamber can be evacuated also. This permits the use of Helium as the driver gas at low pressure, ie. 5 - 10 psig. At these low pressures, driving with Helium is a viable proposition, since the cost of the gas is then about ten shillings per shot.

Fig.(4. 10) shows the pressure and vacuum connections to the shock tube. The control panel layout and the location of the valves isolating the vacuum connections at the tube are shown in plate VII. The controls are so grouped, that once the hydraulic clamp has been closed, all the actions necessary to carry out a run may be controlled from the low pressure end of the tube.

INSTRUMENTATION.

The Shock Tube,

As the instrumentation was developed, trouble was experienced with electrical interference, which manifested itself in the form of spurious triggering of the timing equipment. This was eventually attributed to imperfect grounding of the shock tube itself. The tube is situated in a laboratory on the fourth floor of the Engineering Building. Ground loops were formed by the plumbing connections to the tube in conjunctiom with the electrical earth.

It proved necessary to isolate the tube completely, except for a single earth connection. Fortunately this was feasible, since all the mechanical supports were isolated electrically from the body of the tube by the rubber mountings. The pressure lines are insulated at the tube by the use of tufnol plugs in the tapping holes, a perspex spacer is fitted in the vacuum line and all the transducers are mounted in insulated plugs. A single earth connection is made from the tube to the earth line of the mains supply.

The series wiring employed in the timing circuit had proved particularly susceptible to electrical pick-up until the above noted measures were adopted. Since these steps to eliminate ground loops were taken the timing equipment has proved extremely reliable.

The Shock Timing Circuit.

The normal practice of timing the shock wave past two stations was adopted to measure the shock strength. Thin film heat transfer gauges are used to detect the shock front. These gauges are mounted on pyrex plugs, following the method of ref.(18) and their design is illustrated in fig.(4. 11). Generally speaking films of high resistance, approximately 800 ohms per inch, are drawn. This tends to lead to the gauge resistances being

less consistent in value, however they are used in matched pairs and the high resistance gauges are more sensitive than the more usual 50 - 100 ohm gauge, for a similar power dissipation. The heating current adopted is based on a maximum power dissipation of 0.05 watts, thus with a 200 ohm gauge the heating current is restricted to 15 milliamperes. A block diagram of the shock timing circuit is shown in fig. (4. 12). The pulse amplifier used is the Dynatron Type 50/D, which is supplied in two units. The head amplifier has a fixed gain of 40 db., whilst the main amplifier gain may be varied from 0 - 60 db. Pulse shaping networks are incorporated in the main amplifier, which allow one to pick-off the a.c. voltage across the transducers. In order to obtain a pulse from the leading edge of a step function with this amplifier, the transducers should be negatively biased. The output will then bea sequence of positive pulses derived from the sharp voltage rise obtained as the shock wave passes each transducer.

The amplifier has two outputs, one of which is normally coupled to a Venner Counter. With only two thin film gauges connected, the counter will receive a start pulse as the shock passes the first station and a stop pulse as it passes the second one, both on the same line. The second output may be used to monitor the signal with an oscilloscope, which will display a signal as shown in fig. (4. 14). This allows one to carry out spot checks on the counter calibration very readily. Alternatively and more commonly the second output will be used as a trigger source for another piece of equipment. In plate V. the second output is shown feeding a variable delay unit, which is connected to the trigger unit for a spark light source. It should be noted, that there will be two pulses on this line and the delay should be set with reference to the first transducer station. In addition the equipment so triggered

should have a lock-out facility, or as in the case of the spark gap, a long recharge time constant.

For shock trajectory studies the same circuitry may be employed, with the requisite number of gauges wired in series. The counter would be replaced by an oscilloscope, modified to provide an extended time base, which could be in the form of a raster display, ref.(19).

The power supply used with the shock detectors is an A.E.I. stabilised unit, Type R 1280. Constant current conditions are maintained, using a 10 kilohm dropping resistor and the appropriate value of current is obtained by adjusting the voltage. Twin screened wiring is used in the constant current supply circuit and both the screening and the positive line are grounded at a single point.

Heat Transfer Probes, (a).

Heat transfer measurements, as such, have not been made, but the output from thin film gauges has been used to detect the various waves, which follow the passage of the incident shock wave. The standard shock detector has been used for this purpose, but a gauge with coaxial terminations, fig.(4. 13), has also been used. Some difficulty has been experienced in the manufacture of these gauges, particularly in obtaining a reliable contact at the platinum to tungsten connection. They do, however, offer better frequency response and this may be observed in figs.(4. 15) and (4. 16), which illustrates the outputs of the two types under similar conditions. The resistance of the coaxial type is a quarter that of the straight film gauge, consequently for the same power dissipation the output will be reduced.

Let,

maximum power dissipated	w = watts
film resistance	k = ohm/in.
and total film length	x = in.

Then the resistance of the straight film gauge is,

$$R_s = k.x$$

and the resistance of the coaxial gauge is,

$$R_c = k.\frac{x}{4}$$

and the current taken by each gauge will be given by;

$$i_s^2 = \frac{w}{k.x} \quad \text{and} \quad i_c^2 = \frac{4w}{k.x}$$

If the change in resistance per unit length, $\Delta k/k$, is the same for each gauge then,

$$\Delta R/R = \Delta k.x/k.x = \Delta V/V \ ,$$

when the heating current is sensibly constant,

$$\text{ie. } \Delta V_s/\Delta V_c = \frac{1}{2}$$

The heat transfer gauges are normally coupled to a Tektronix 502A oscilloscope, which has a maximum sensitivity of 0.1 mV./cm., thus the the lower gauge sensitivity presents no real problem. It must be borne in mind however, that the bandwidth of the oscilloscope is related to the gain on the vertical amplifier and at the maximum gain the bandwidth is reduced to 50 Kc./sec. with this oscilloscope. In any particular instance it is a question of weighing the relative conditions in order to assess whether it is worthwhile using the somewhat less reliable coaxial type.

Heat Transfer Probes, (b).

Stagnation point thin film gauges have been used for the same purpose as the wall mounted gauges. Their response to the various waves tends, in general, to be less subject to misinterpretation. It is unfortunate that their design, at the present time, only allows their

use in the "working section". It was found necessary to include the spring loading in order to prevent the glass breaking when the shock front arrived at the assembly. The design lends itself to a simple modification, which would allow one to mount a series of transducers on the one support across the tube. The stagnation point gauge has proved an ideal instrument for measuring the duration of the quasi-steady flow. A stagnation probe has also been used to monitor the flow near the diaphragm station, immediately after diaphragm rupture.

With a view to obtaiming useful results immediately after the passage of the shock front, a stagnation point probe, incorporating a coaxial gauge,,has been devised; the design is illustrated in fig.(4. 13).

It has been found particularly convenient to use high tension dry batteries as a voltage source for the heat transfer probes. Sensibly constant current supply is ensured by using a 5 - 10 kilohm resistor in series with the thin film.

Schlieren System and Associated Equipment.

A Toepler Schlieren System is available, a diagramatic layout, of which, is shown in fig.(4. 18). It comprises two 8 inch diameter spherical mirrors, two 4 inch diameter plane folding mirrors, a slit and a condenser set. There are two light sources, a 12 volt car bulb, used to align the system and a spark gap. The location of these is shown in the diagram and a simple mirror is used to switch from one source to the other.

The spark light source is based on a design supplied by Mr. J. Busing of the College of Aeronautics. It employs an efficient 0.024 microfarad Barium Titanate Capacitor and the gap is triggered by a third electrode. The 17 KV. power supply and trigger unit was designed and built by

Mr. R. Perry of the University Aeronautics Department. The gap trigger voltage, nominally 3 KV. is derived from a standard car ignition coil. The 10 volt trigger pulse for the main gap trigger unit is normally taken from the second output of the pulse amplifier, via a delayed pulse generator.

The delay unit was designed and built by Mr. J. Cochrane of the University Electronics Department and it enables one to delay a pulse for any predetermined period ranging from 10 microseconds to 10 milliseconds. The delay generator requires a 10 volt positive pulse to trigger it and delivers, after the requisite time delay, a 10 volt negative pulse, the width of which, may be varied from 40 to 240 microseconds. To maintain optimum signal to noise characteristics for the whole system, a times 2 attenuator is incorporated at the input to the Venner Counter, when the spark trigger apparatus is operated in conjunction with the timing equipment.

In order to ensure reliable triggering of the spark gap, a pulse at least 100 microseconds wide is required at the input to the spark trigger unit. The resultant delay in this unit then lies in the range 120 - 125 microseconds. This delay was measured using a double pulse generator to trigger the system and a semiconductor, (Silicon), to detect the gap breakdown. A typical signal, monitored on an oscilloscope, is shown in fig.(4. 17).

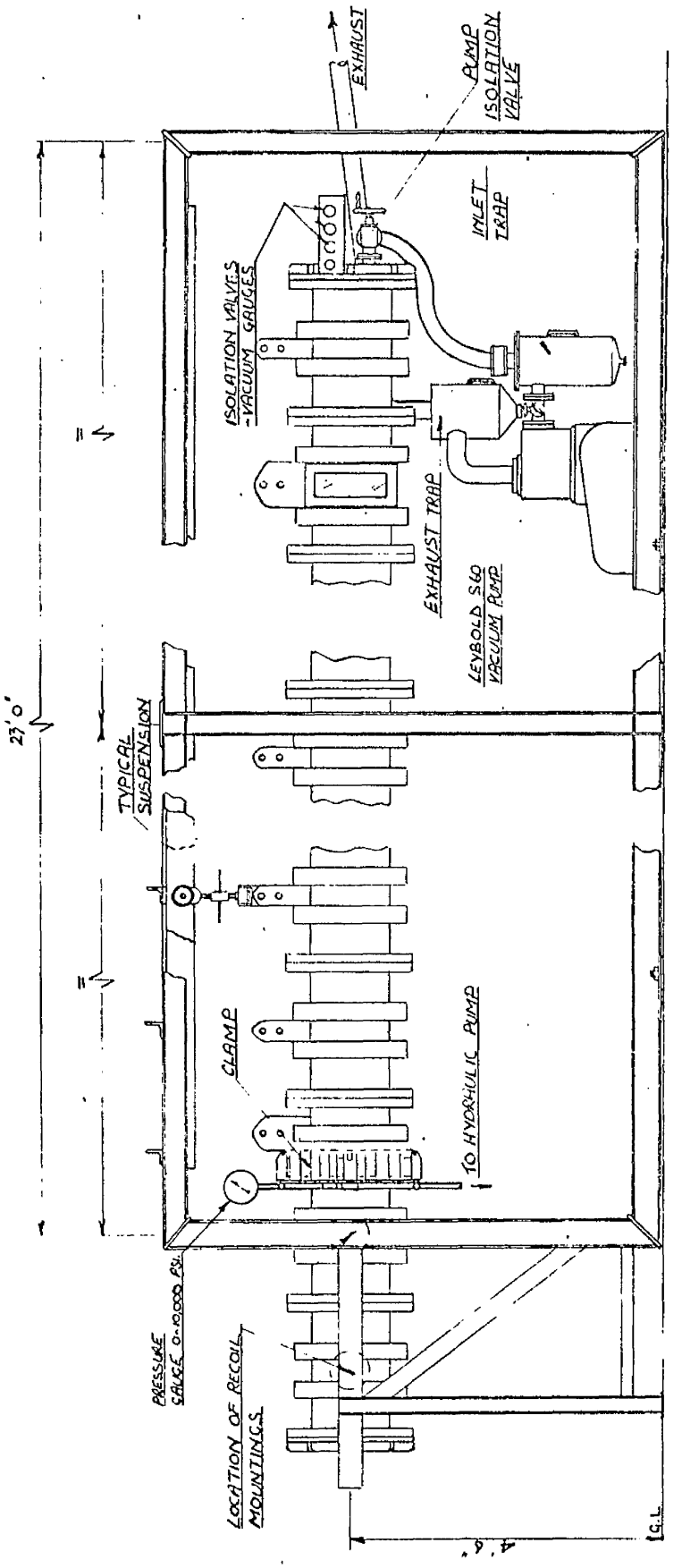

12"×12" SHOCK TUBE - ARRANGEMENT

Fig. (4. 1)

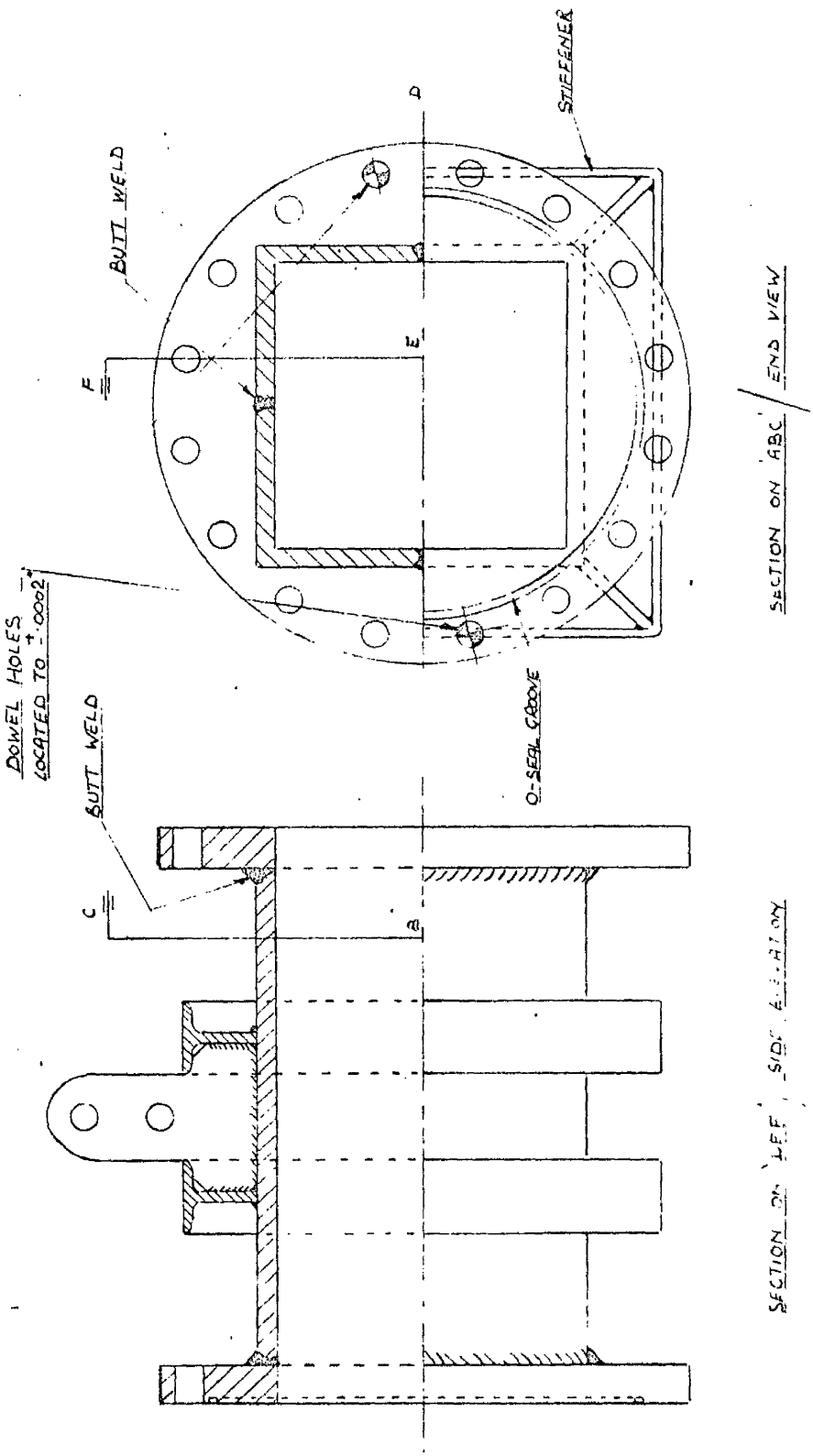

STANDARD 2'0" SHOCK TUBE SECTION

Fig. (4. 2)

Fig.(4. 4)

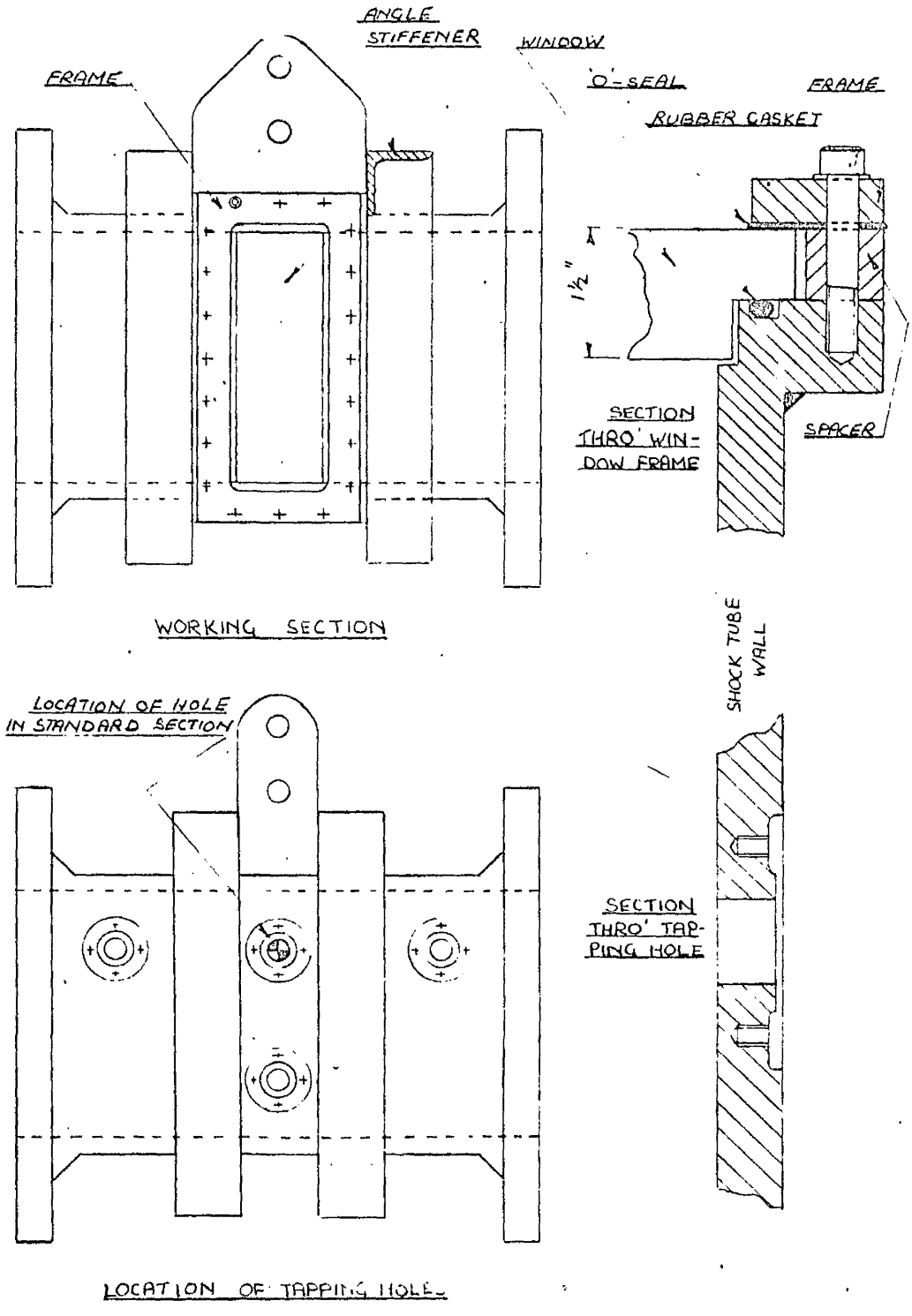
ANGLE STIFFENER
WINDOW
FRAME
O-SEAL
FRAME
RUBBER GASKET
1½"
SECTION THRO' WINDOW FRAME
SPACER
WORKING SECTION
LOCATION OF HOLE IN STANDARD SECTION
SHOCK TUBE WALL
SECTION THRO' TAPPING HOLE
LOCATION OF TAPPING HOLE

Fig.(4. 3)

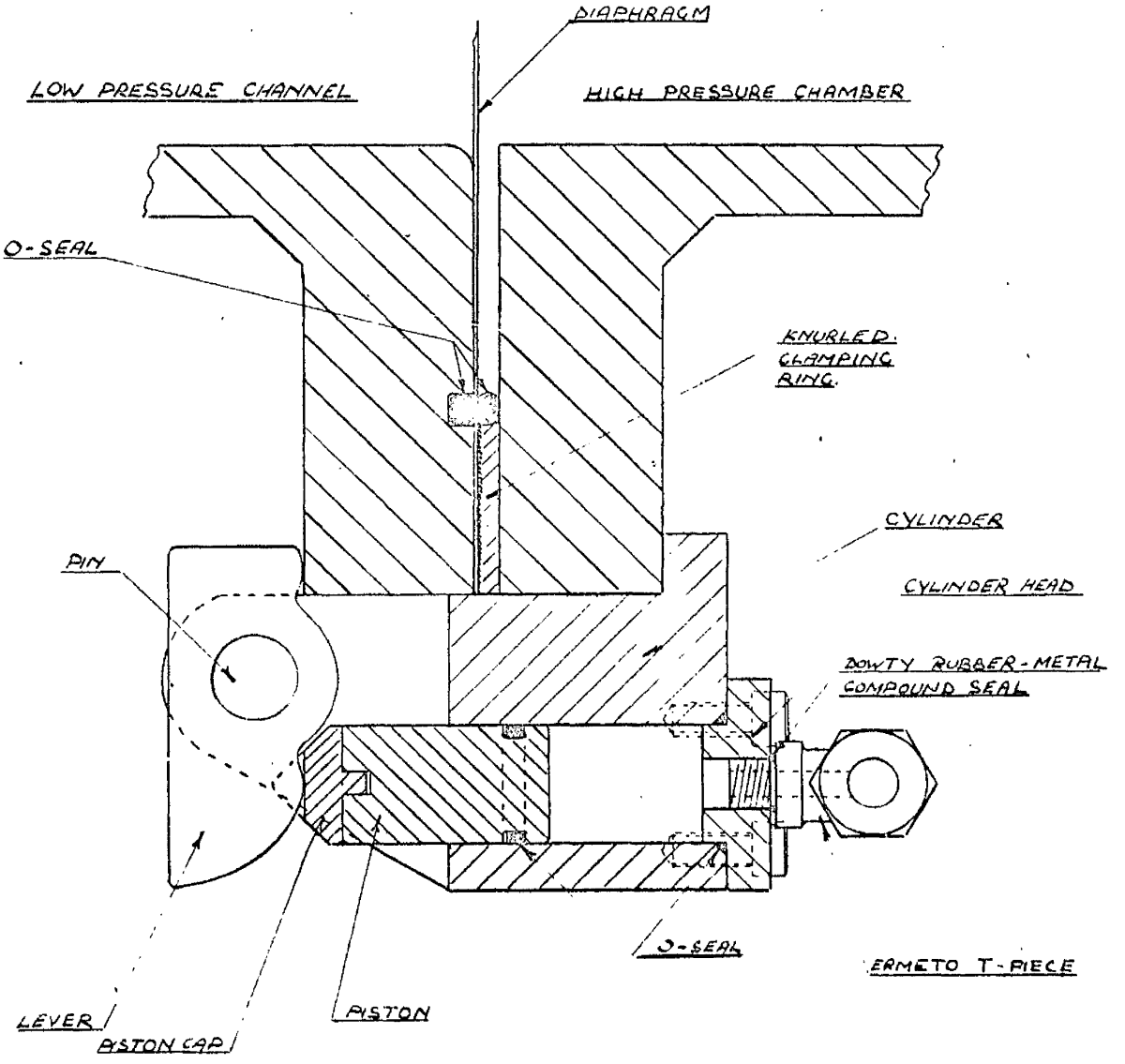

SECTION THROUGH DIAPHRAGM CLAMP

Fig.(4. 5)

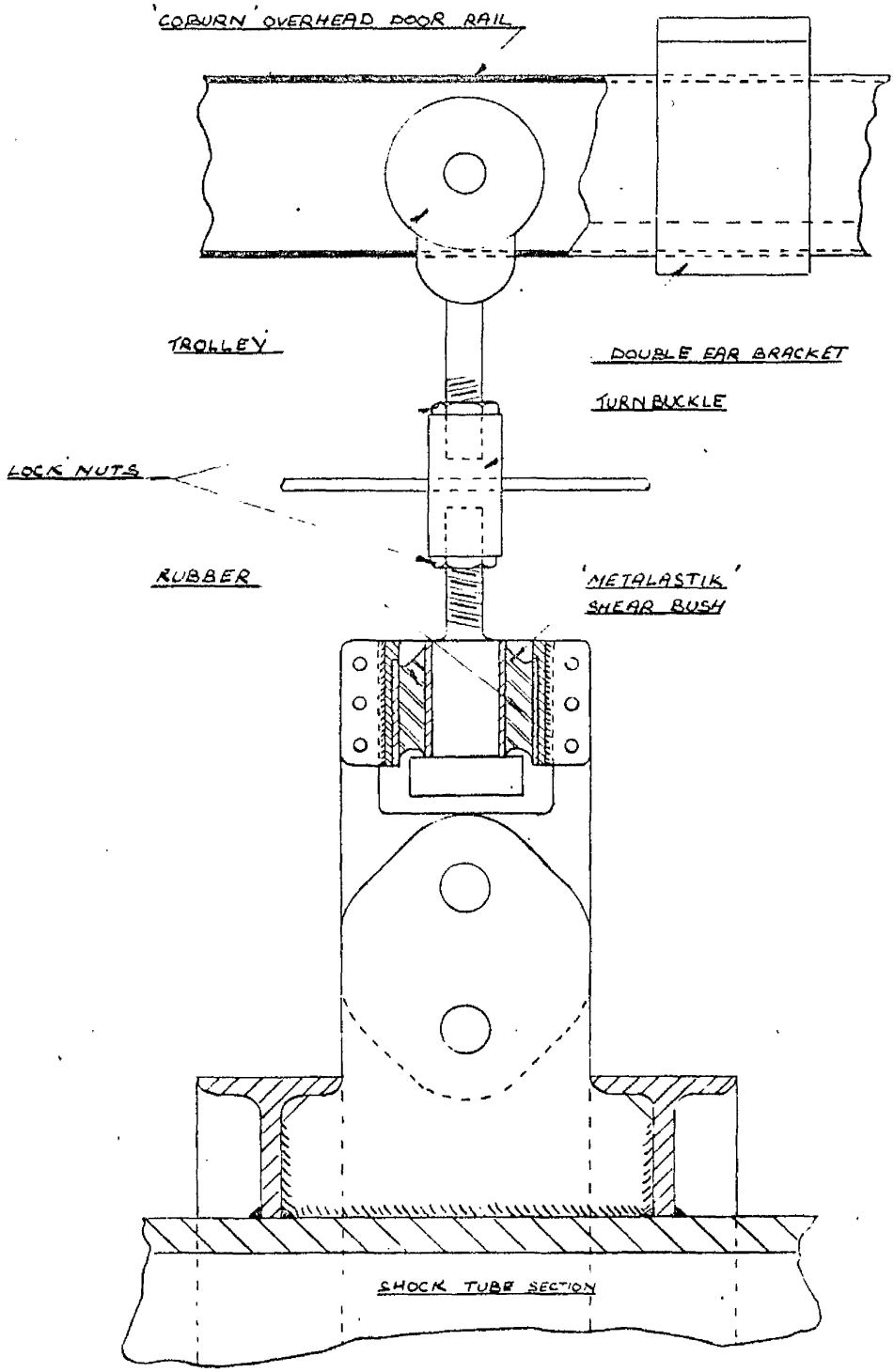

SHOCK TUBE SUSPENSION

Fig.(4. 6)

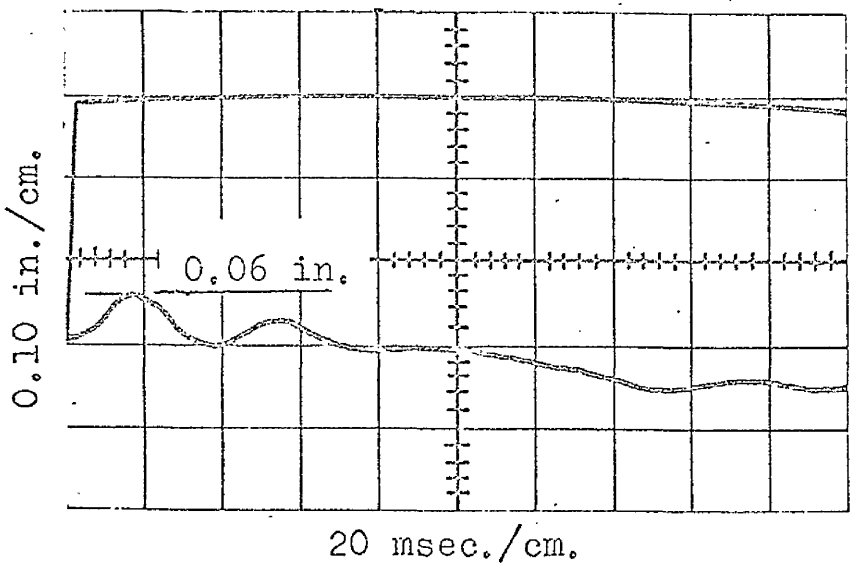

Fig.(4. 7) P_4 = 230 lb/in^2, gauge.

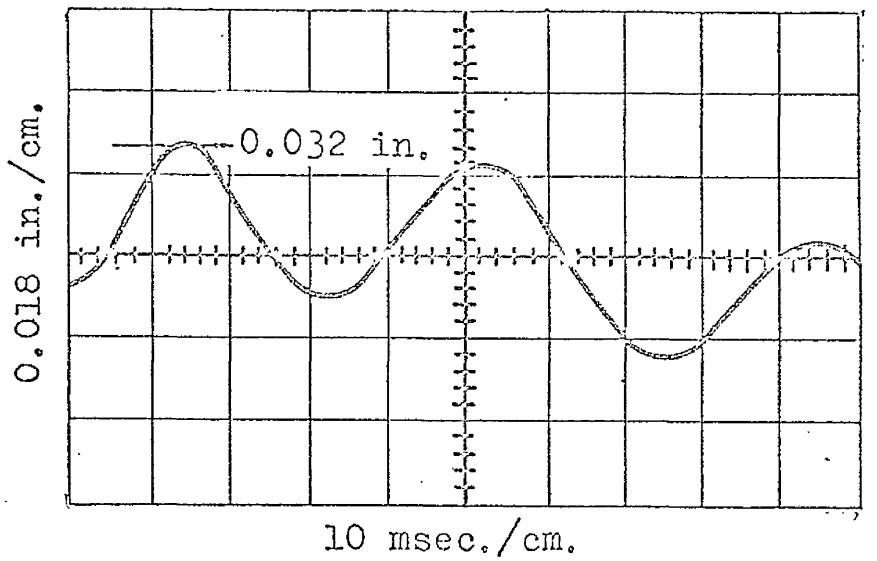

Fig.(4. 8) P_4 = 112 lb/in^2, gauge.

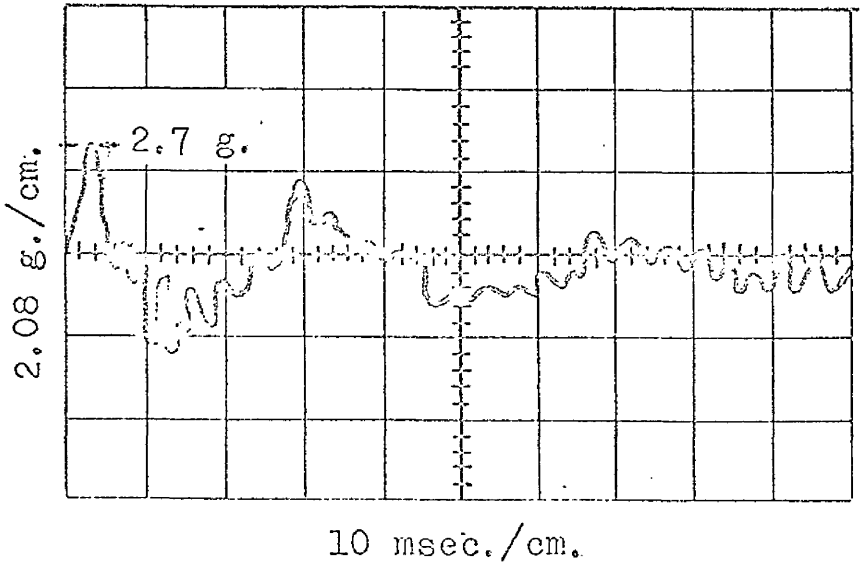

Fig.(4. 9) P_4 = 124 lb/in^2, gauge.

Acceleration and Displacement Measurements of the Recoil Characteristics.

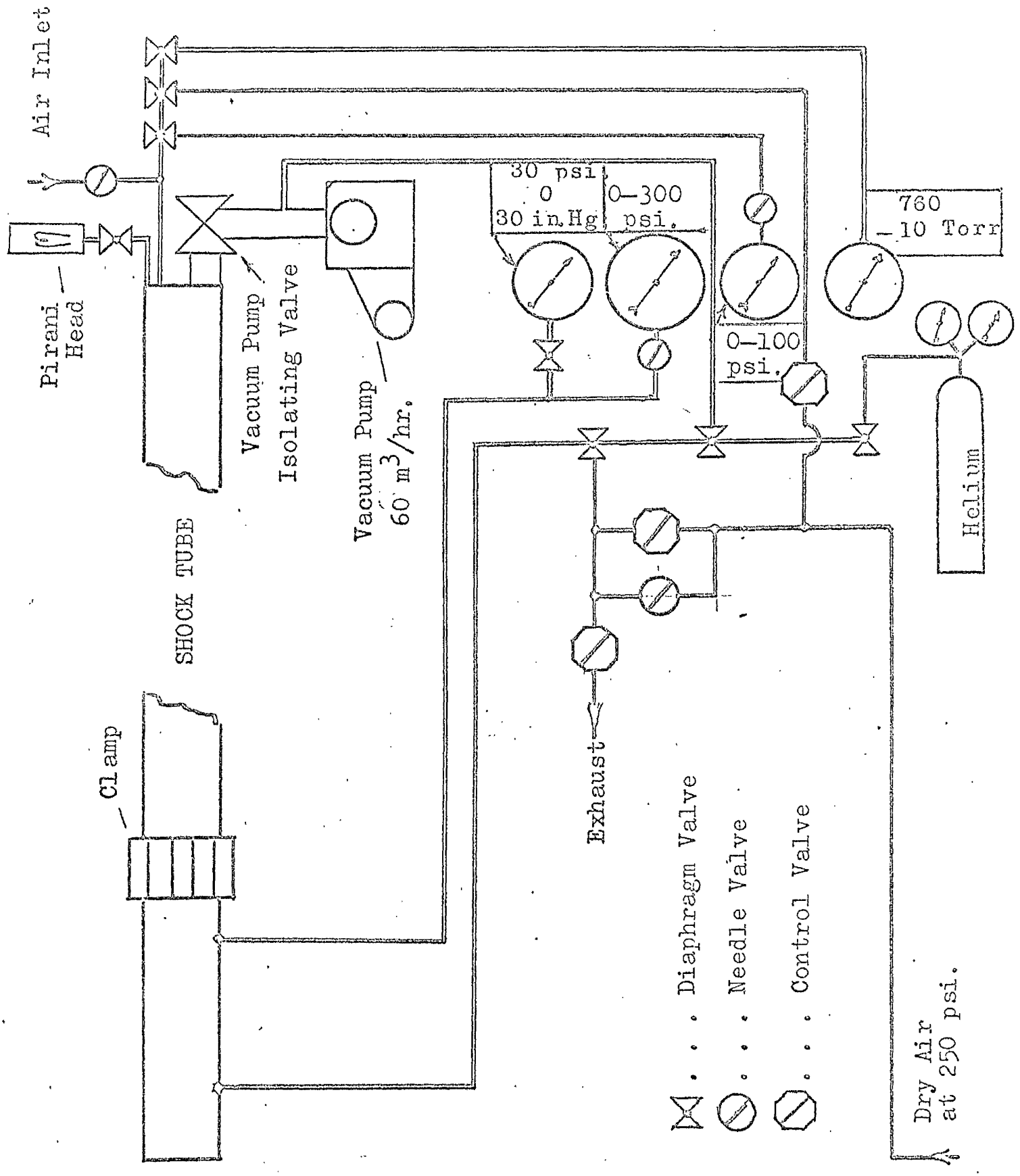

Layout of Pressure and Vacuum Lines

Fig.(4. 10)

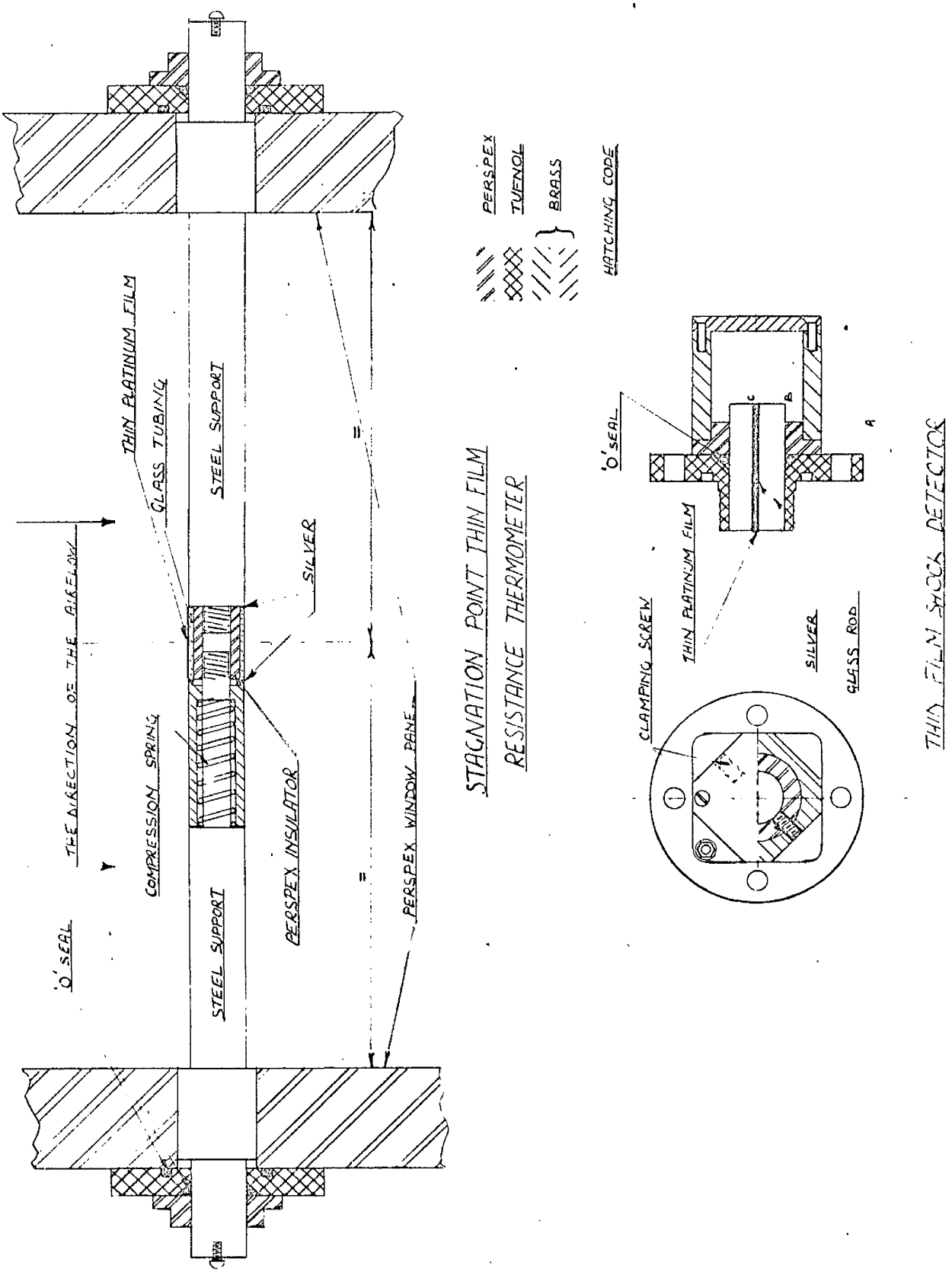
THIN PLATINUM FILM
GLASS TUBING
STEEL SUPPORT
SILVER
THE DIRECTION OF THE AIRFLOW
COMPRESSION SPRING
O' SEAL
PERSPEX INSULATOR
PERSPEX WINDOW PANE
STEEL SUPPORT
PERSPEX
TUFNOL
BRASS
HATCHING CODE
STAGNATION POINT THIN FILM
RESISTANCE THERMOMETER
O' SEAL
CLAMPING SCREW
THIN PLATINUM FILM
SILVER
GLASS ROD
THIN FILM SHOCK DETECTOR

Fig.(4. 11)

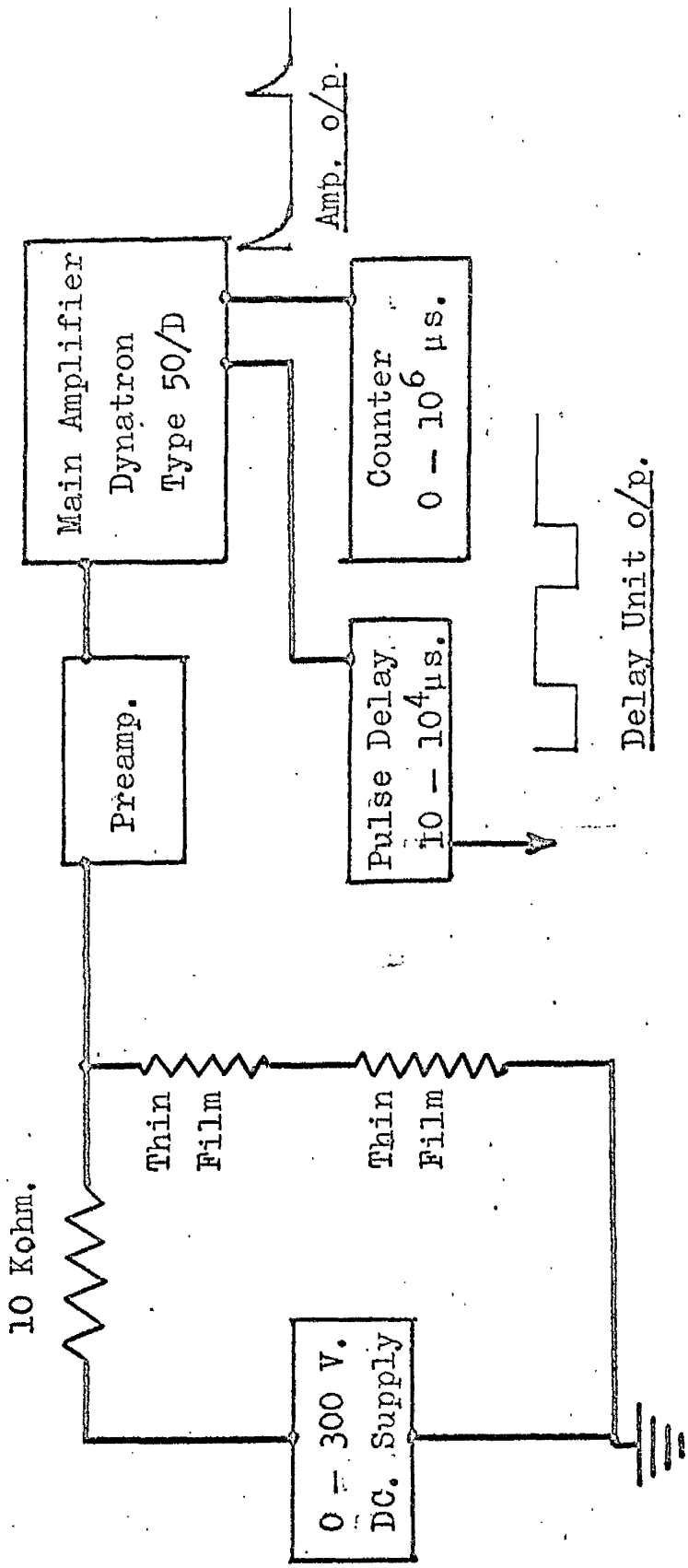

Fig.(4. 12) Block Diagram of Shock Timing Circuit.

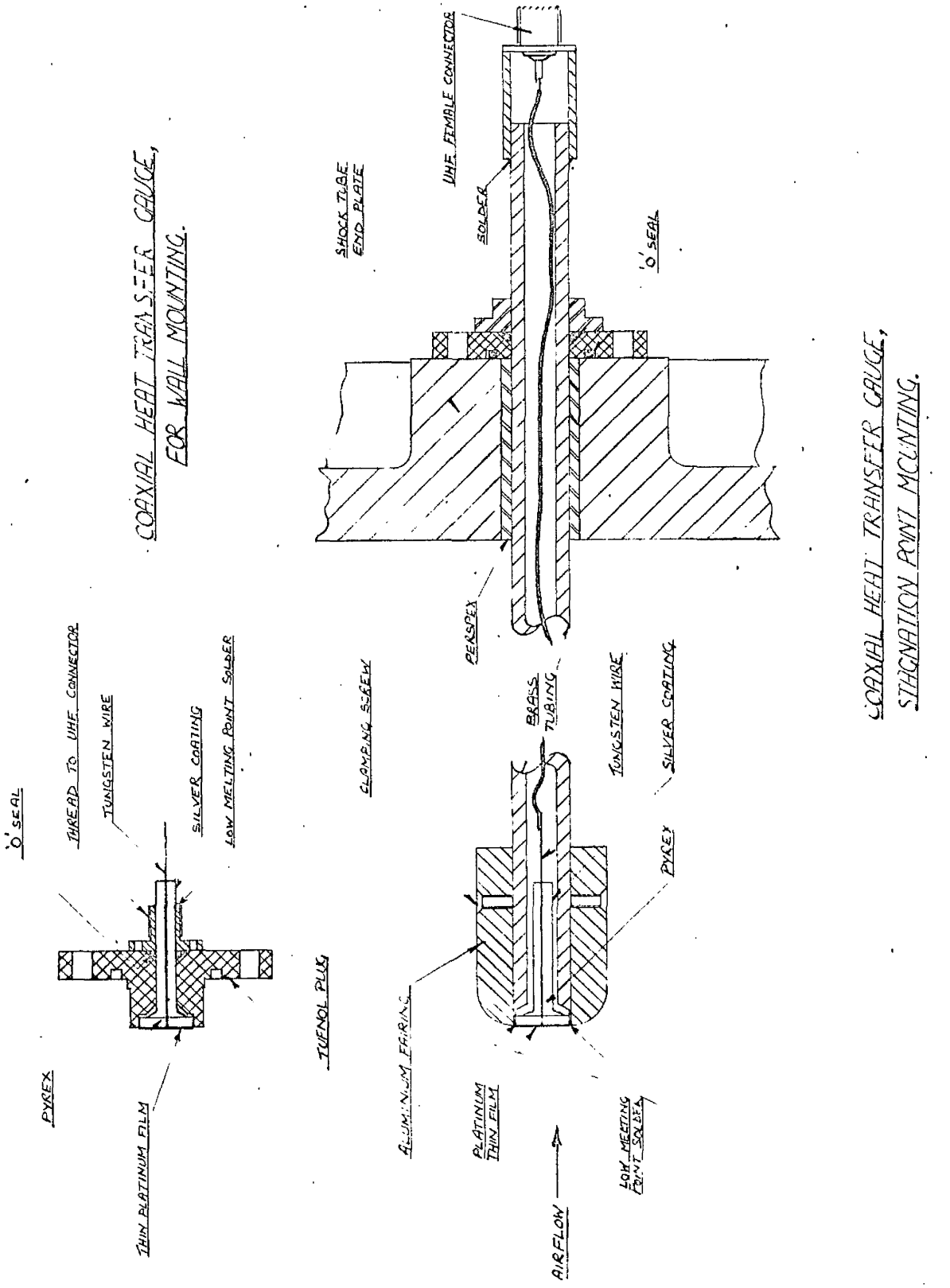
COAXIAL HEAT TRANSFER GAUGE, FOR WALL MOUNTING.
SHOCK TUBE END PLATE
UHF. FIMBLE CONNECTOR
SOLDER
'O' SEAL
PERSPEX
'O' SEAL
THREAD TO UHF. CONNECTOR
TUNGSTEN WIRE
SILVER COATING
LOW MELTING POINT SOLDER
CLAMPING SCREW
BRASS TUBING
TUNGSTEN WIRE
SILVER COATING
PYREX
PYREX
THIN PLATINUM FILM
TUFNOL PLUG
ALUMINIUM FAIRING
PLATINUM THIN FILM
LOW MELTING POINT SOLDER
AIRFLOW
COAXIAL HEAT TRANSFER GAUGE, STAGNATION POINT MOUNTING.

Fig.(4. 13)

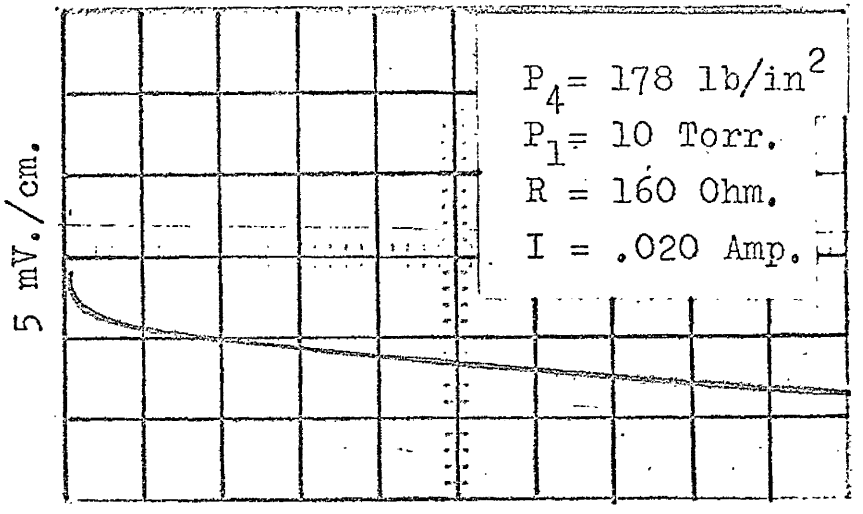

Fig.(4. 15) Signal from Std. Wall Gauge.

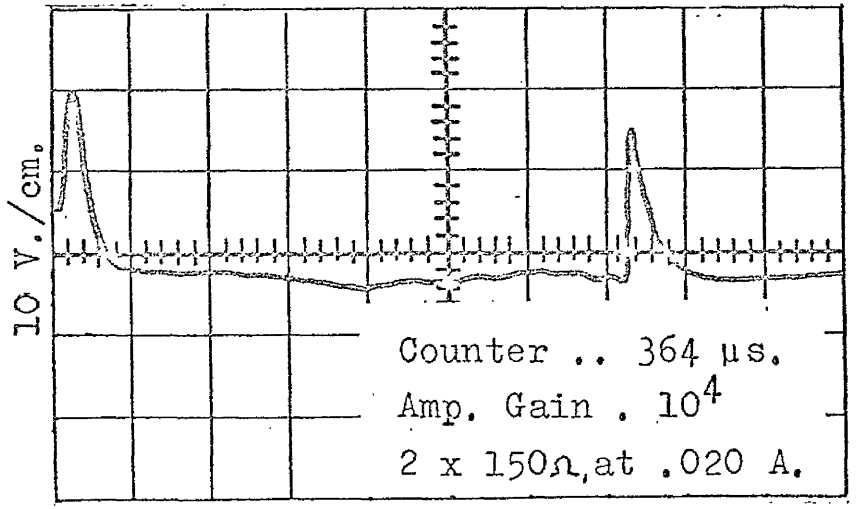

Fig.(4. 14) o/p Signal from Pulse Amplifier.

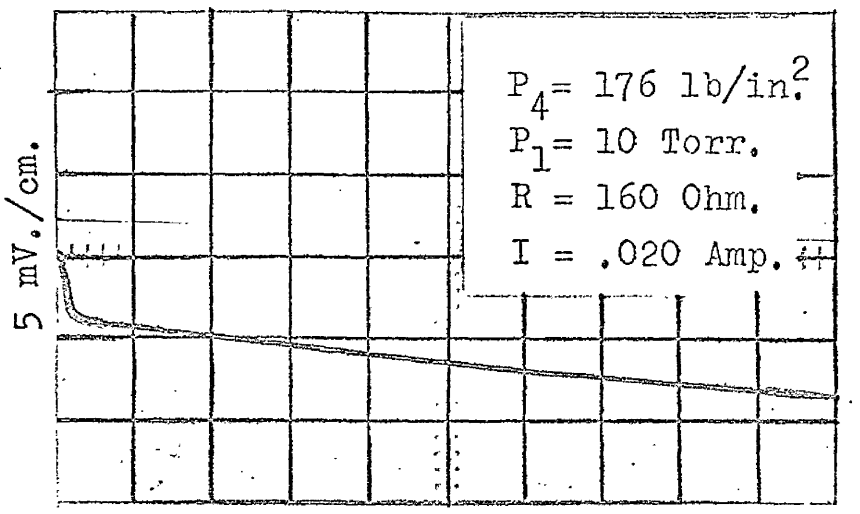

Fig.(4. 16) Signal from Coaxial Type Wall Gauge.

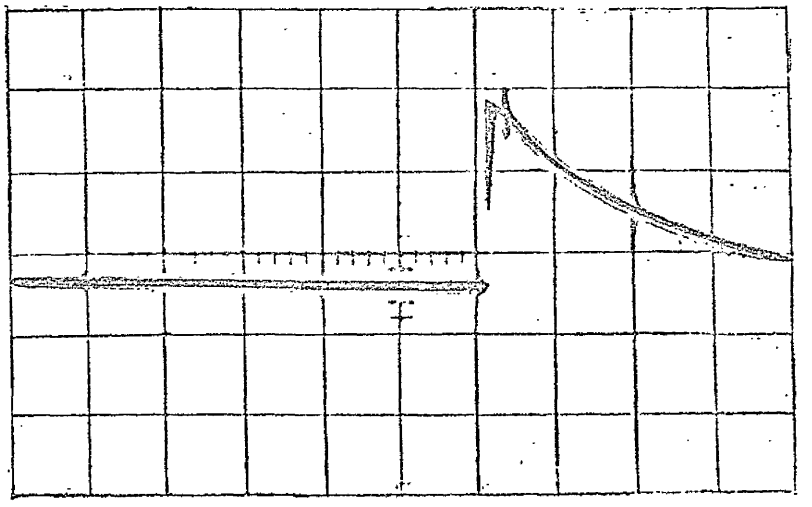

Fig.(4. 17) Measured Delay between Trigger Pulse and Spark.

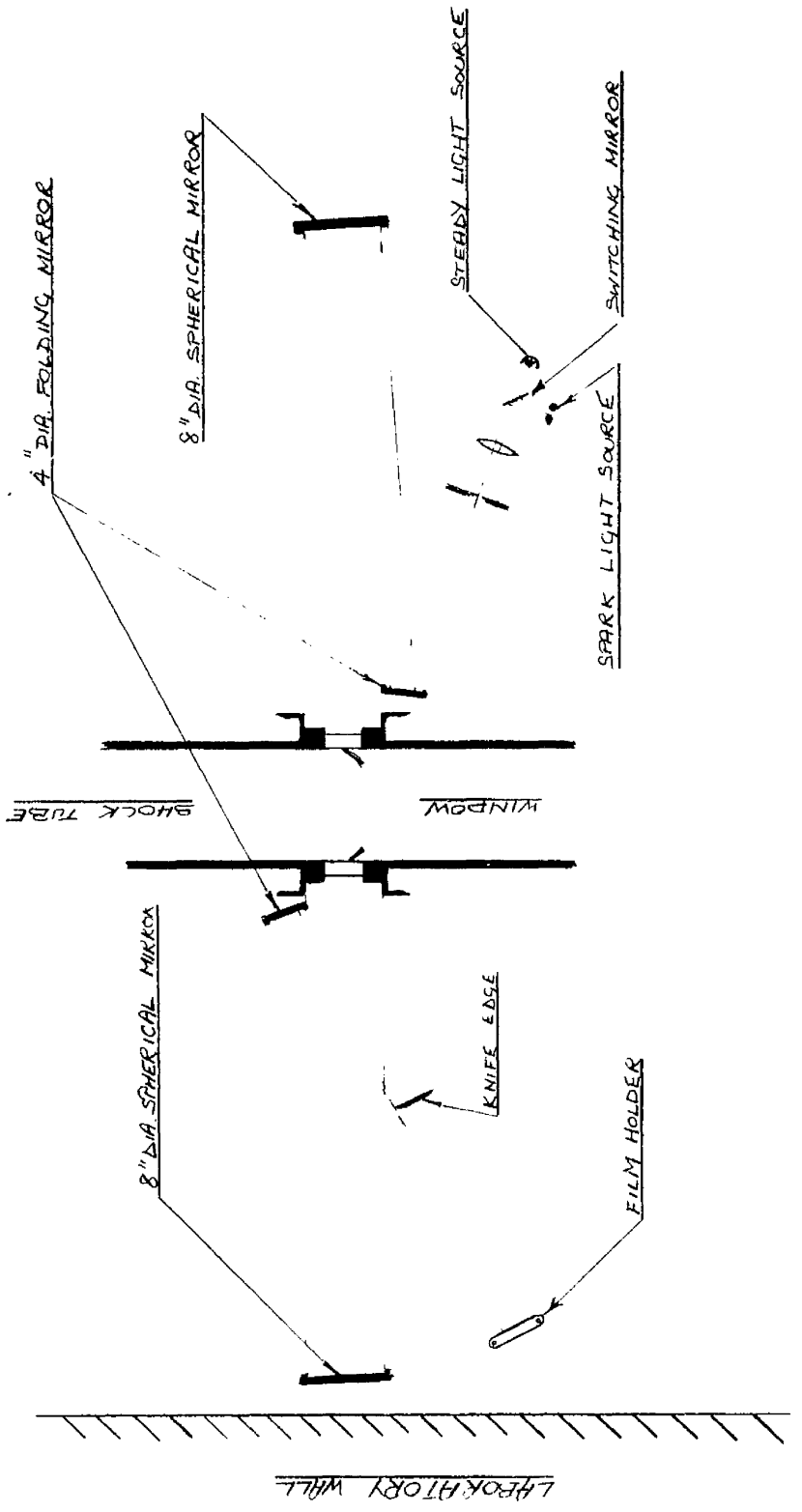

DIAGRAMATIC ILLUSTRATION OF THE SCHLIEREN SYSTEM

Fig.(4. 18)

General View of the Shock Tube

PLATE II.

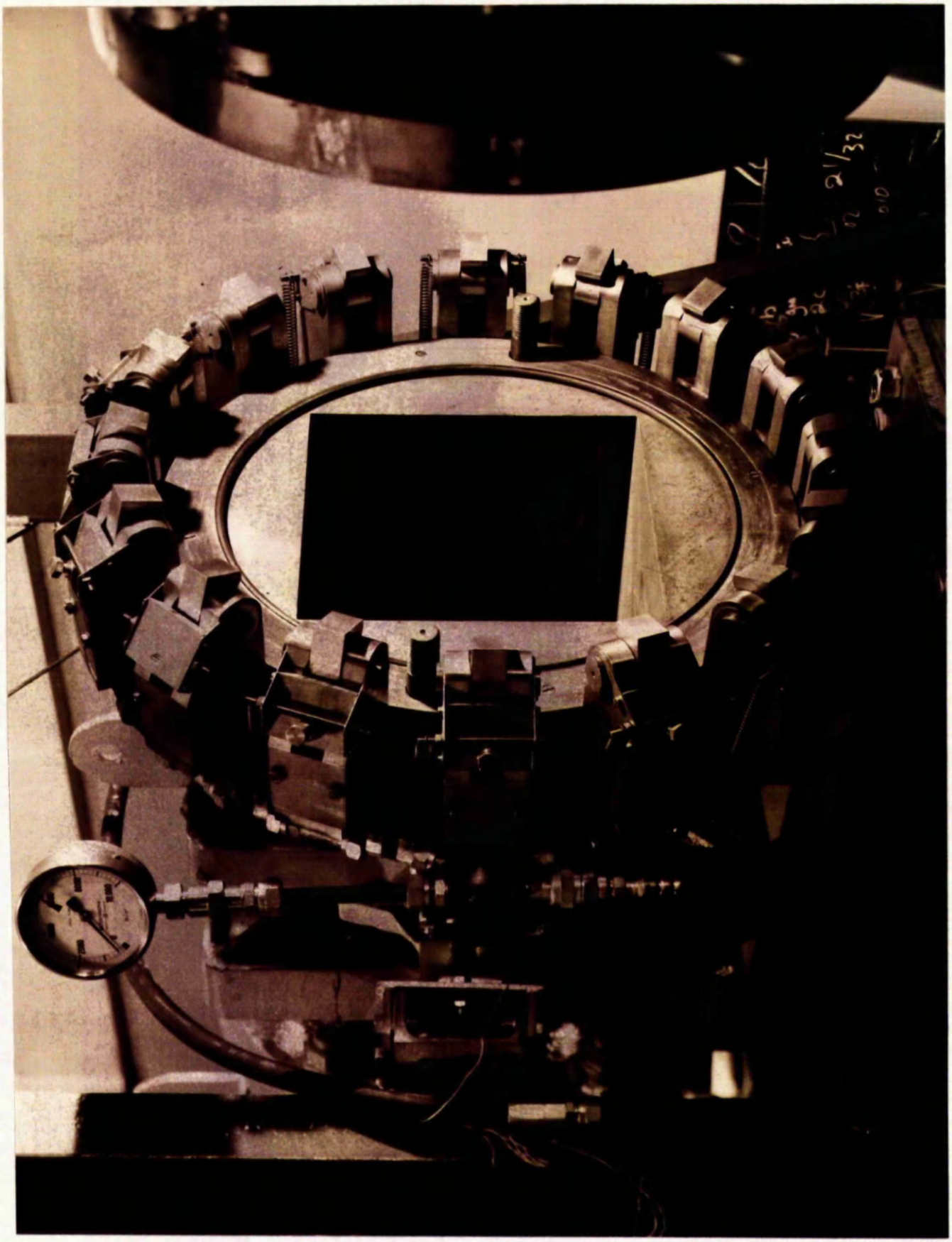

The Hydraulic Clamp

PLATE III.

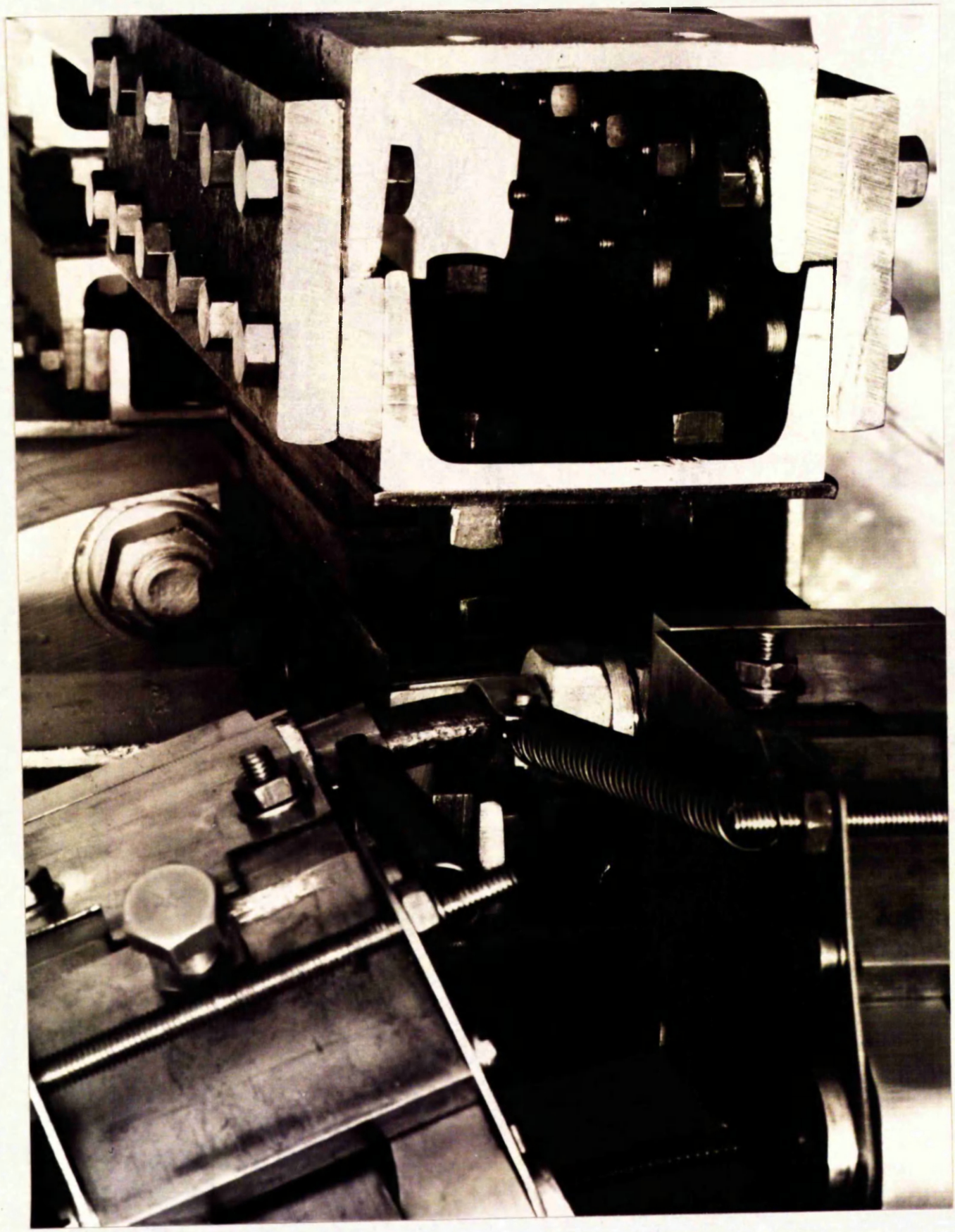

The Recoil Mountings

PLATE IV.

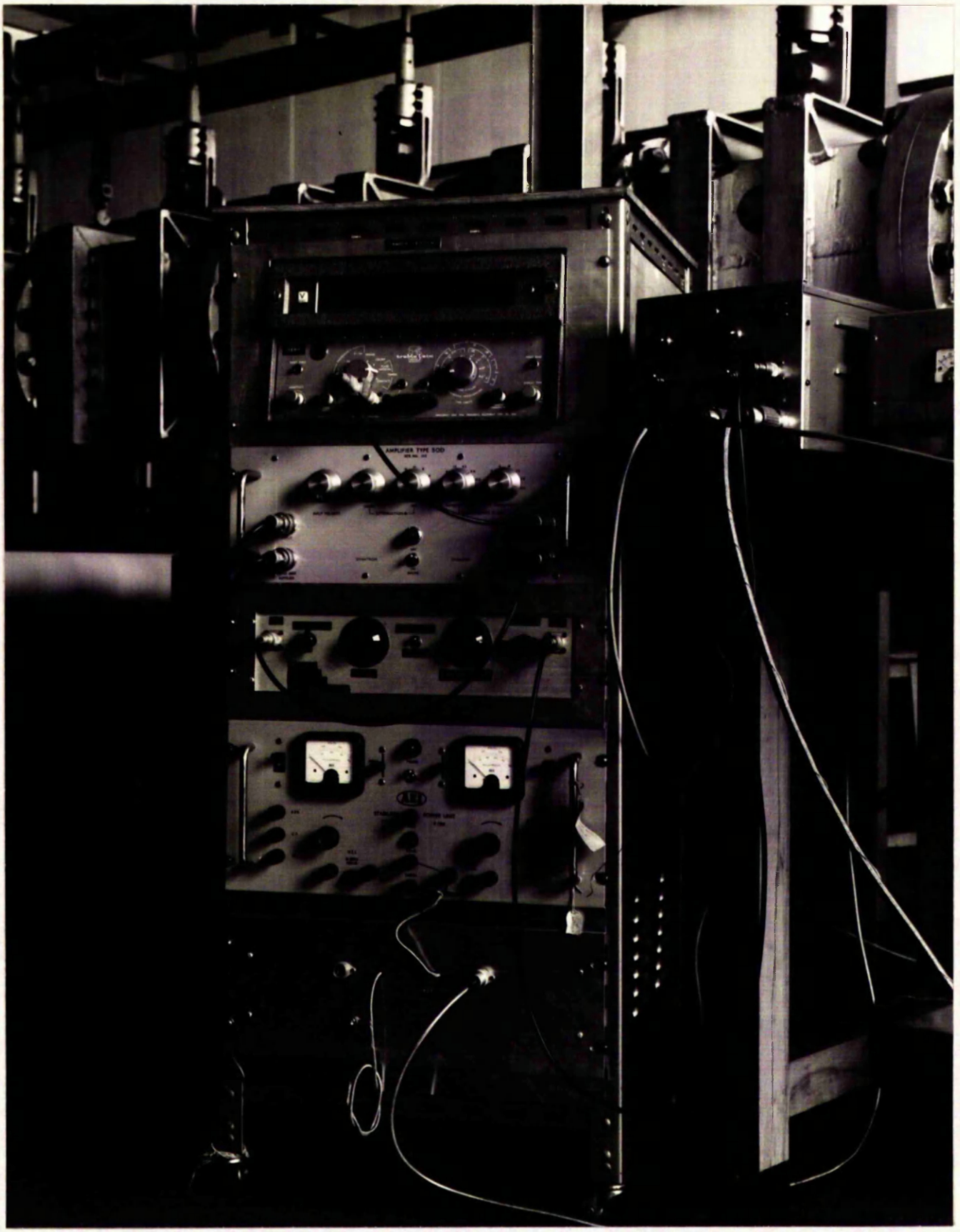

Shock Timing Equipment & Spark Trigger Unit

PLATE V.

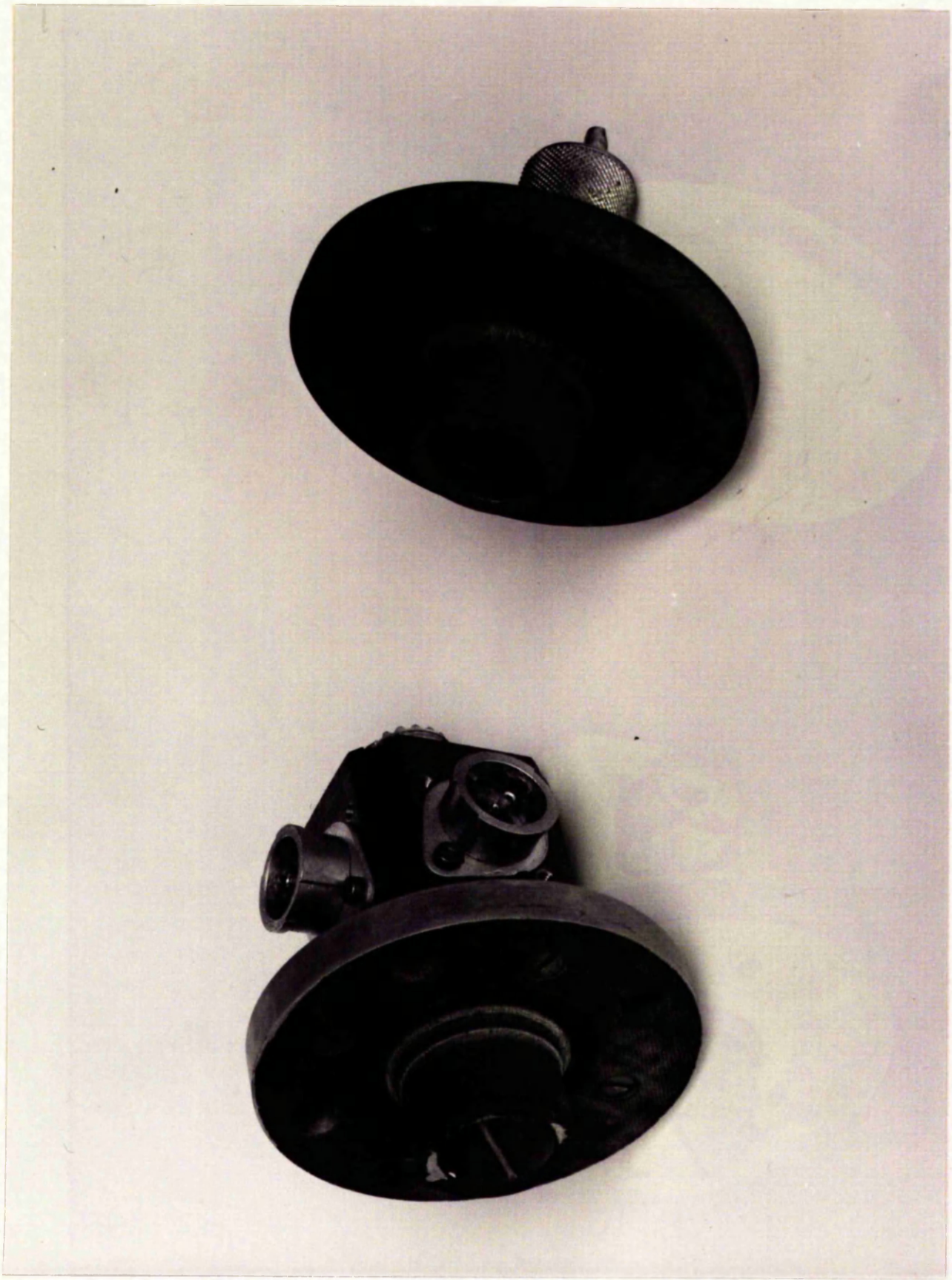

Thin Film, Wall Mounted, Heat Transfer Gauges

PLATE VI.

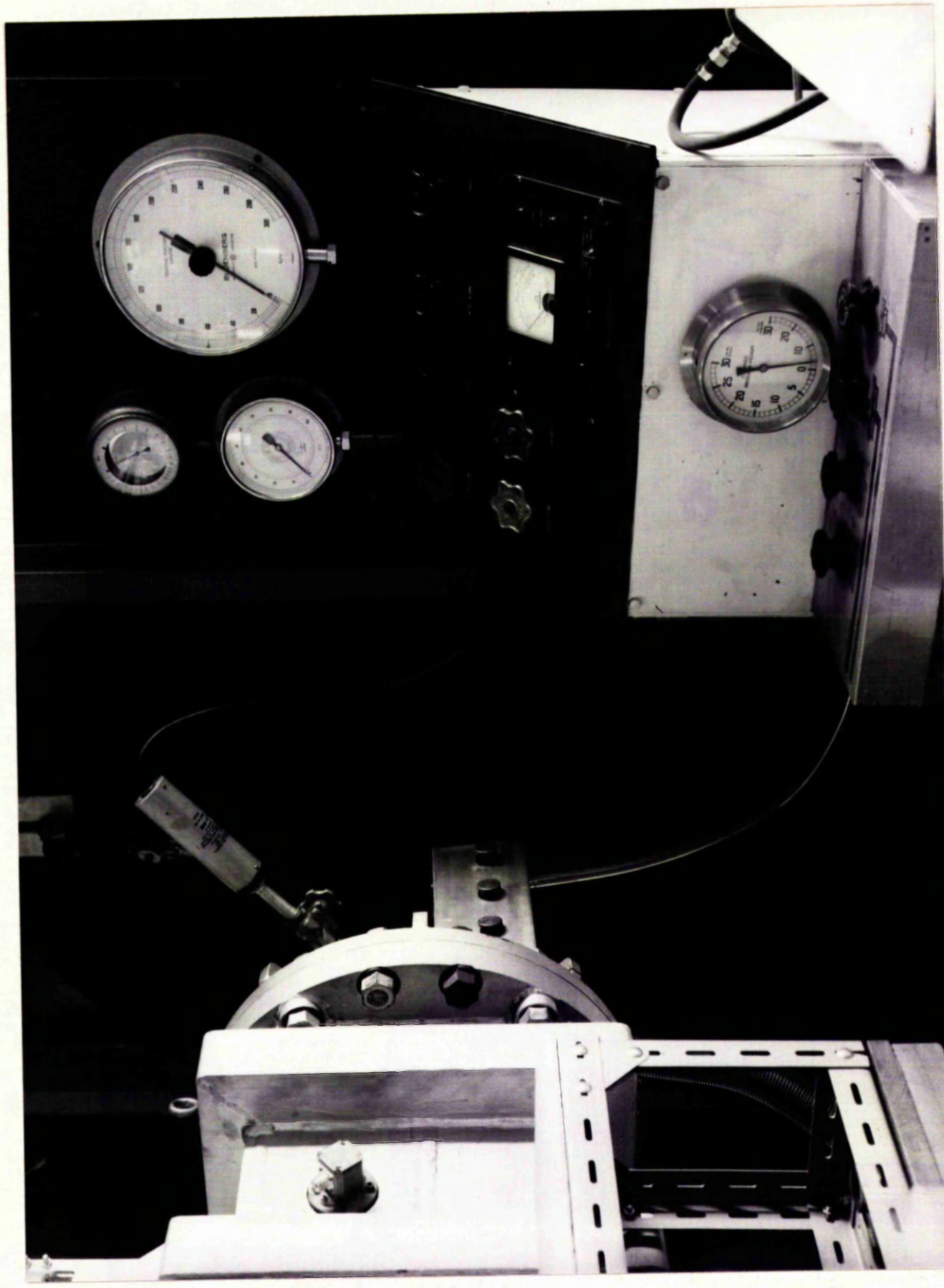

Control Panel

PLATE VII.

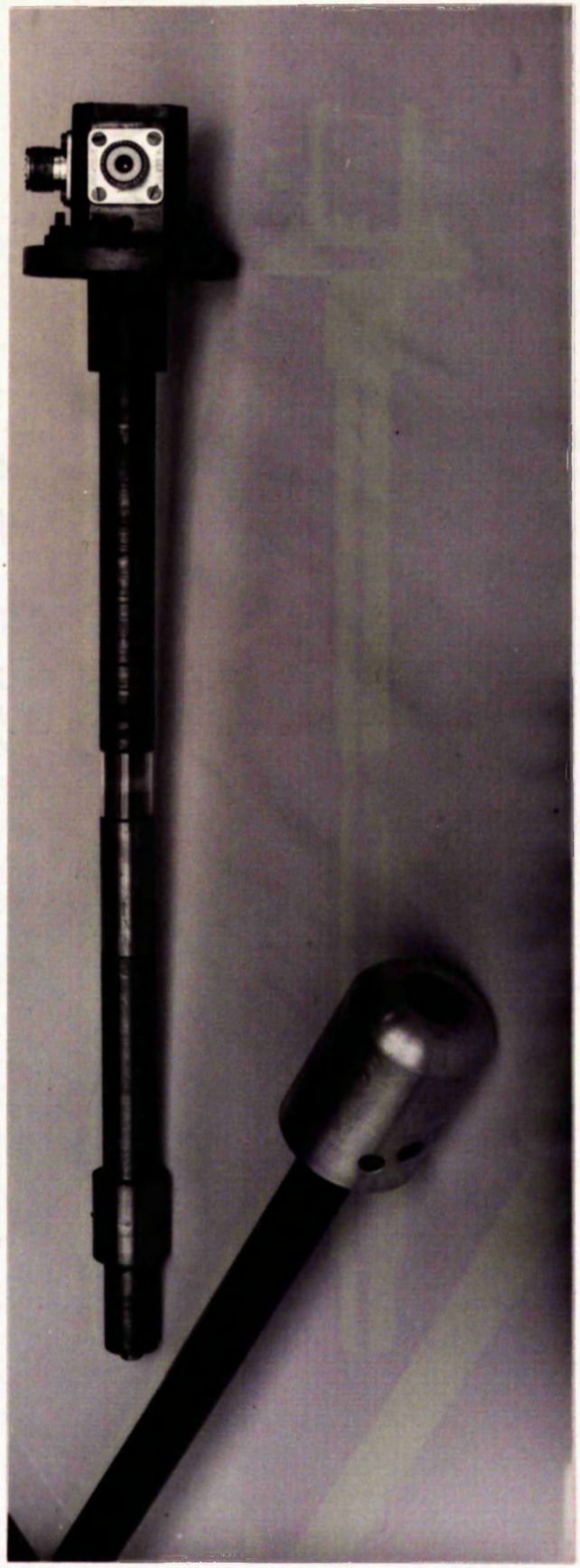

Stagnation Point Thin Film Heat Transfer Gauges

PLATE VIII.

PLATE IX.

View Illustrating Schlieren Light Sources

CHAPTER 5

THEORETICAL EXAMINATION OF THE DIAPHRAGM OPENING.

THEORETICAL EXAMINATION OF THE DIAPHRAGM OPENING.

INTRODUCTION.

It has been noted, Chapter 3, that strong secondary shock waves have been observed under certain conditions. The advantageous effect, which such shock waves have upon the resultant flow has also been discussed. In the following chapter an attempt is made to evaluate the circumstances, which could lead to their formation.

Initially we shall follow the method of Kireyev, ref.(14) and assume that the effect of the diaphragm may be described by the quasi-steady solution applied to a supersonic nozzle, which is varying with time. This is an isentropic solution, which cannot describe the real conditions, but because of the large entropy variations present elsewhere, which may be taken as a reasonable approximation to the real case.

ISENTROPIC SOLUTION.

The solution is treated in two parts;

(a) the solution of the equation of motion of the diaphragm petals,

and (b) the flow resulting from the diaphragm opening, which is solved using the method of characteristics.

Unfortunately the two parts are interdependent and in the treatment of (a) it has proved necessary to resort to reasonable approximations as to how the pressure distribution on the petals varies with their angular displacement θ. Fig. (5. 1) illustrates the model chosen.

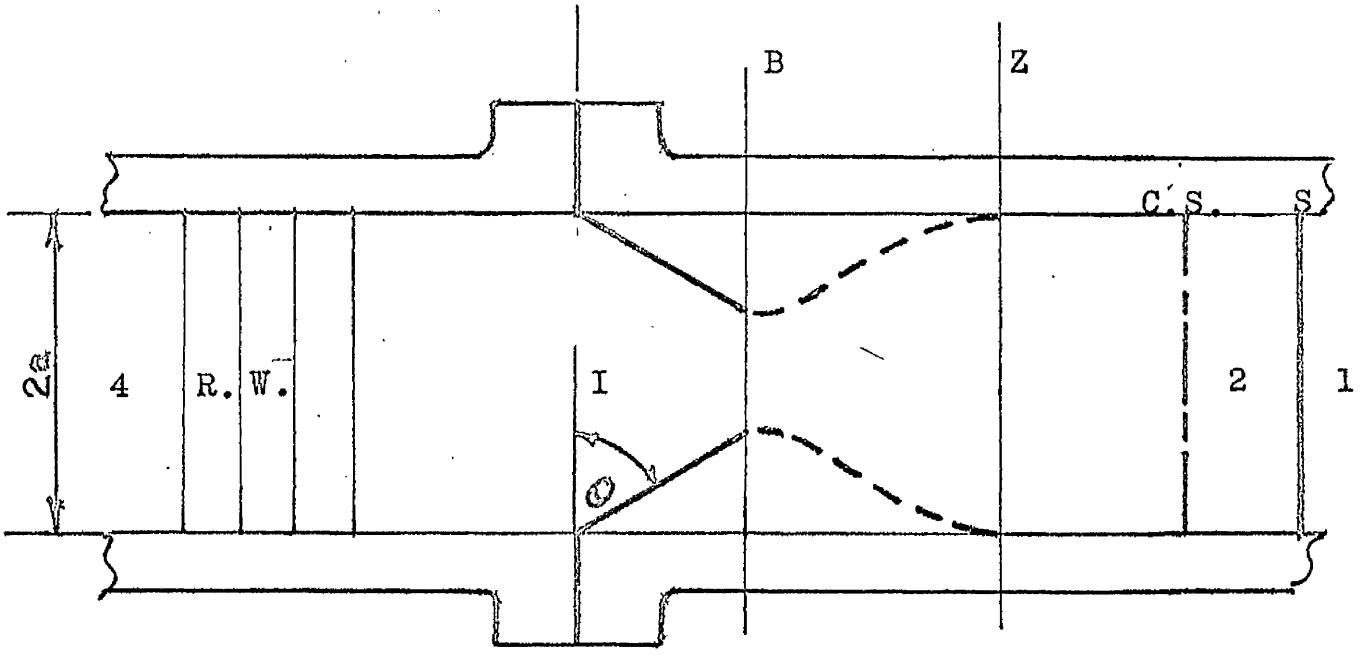

Fig.(5. 1)

It is assumed that a crack starts at the centre of the diaphragm and propagates along the scribe pattern at the rate, which is normal for brittle fractures in steel, viz. 17,000 feet per second approximately. Some time later the hole is of finite size and the mixing process has settled down. At this time it is assumed that the flow may be treated as being one-dimensional. From this point in time onwards the problem is treated using the method of characteristics with the boundary conditions imposed by the varying nozzle at B and the static pressure ratio.

To obtain the timewise variation of the nozzle throat area the equation of motion for the petal must be solved. In fig.(5. 2) the assumed shape of the petal is shown, which is governed by the initial deflection angle, taken as $\theta_o = 30^o$ in all cases, and the scribe pattern. As a further simplification the petals are assumed to be plane.

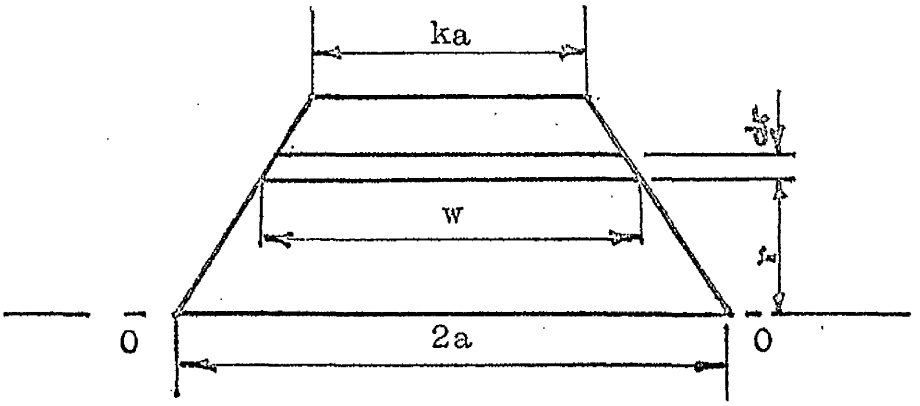

Fig.(5. 2)

This configuration is valid only for a square tube, or in the case of a round tube, where a is not the radius, but some mean dimension. The term k is a function of the scribe pattern, eg. k = 0, for diagonal scribing.

The area of element w.dr at r is given by,

$$w.dr = \left[\sqrt{\frac{3}{2}}r(k - 2) + 2a\right] dr \qquad \ldots.(5.\ 1)$$

ACCELERATING FORCES ON THE PETAL.

(a) The petal is accelerated by the action of the differential pressure.

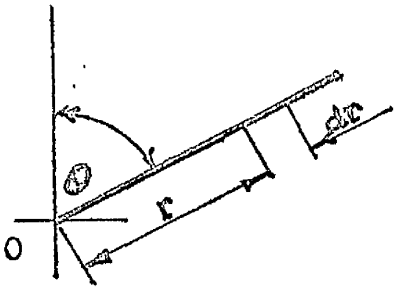

Fig.(5. 3)

The pressure differential p on the element w.dr applies torque $^{T}p_{w}$ about 0, where

$$^{T}p_{w} = p\left[\sqrt{\frac{3}{2}}r(k - 2) + 2a\right] r.dr \qquad \ldots.(5.\ 2)$$

Integrating over the whole plate; from r = 0 to $r = \frac{2a}{\sqrt{3}}$, one obtains the total torque T_p about the edge 0

$$T_p = p \frac{4a^3}{3} \cdot \left[\frac{(k-2)}{3} + 1\right] \qquad \ldots.(5.\ 3)$$

The moment of inertia I of the petal about 0 is

$$I = \frac{2\sqrt{3}}{9} \cdot a^4 \left(k + \frac{2}{3}\right) \cdot \frac{W}{g} \qquad \ldots.\ (5.\ 4)$$

From equations (5. 3) and (5. 4) one obtains the relation for the angular acceleration of the petal;

$$\left[\frac{d^2\theta}{dt^2}\right]_p = 2\sqrt{3} \cdot \frac{pg}{aW} \cdot \frac{(k+1)}{(3k+2)} \qquad \ldots.(5.\ 5)$$

(b) The release of elastic energy when the diaphragm ruptures will also tend to impart an angular acceleration to the petals.

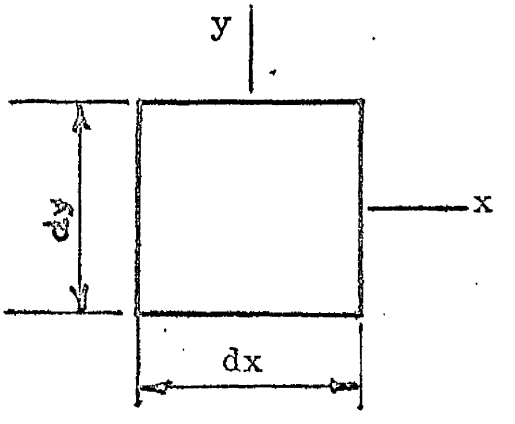

Fig.(5. 4)

Consider a small element dx.dy of a uniformly stressed diaphragm.

Then,

$$\epsilon_x = \frac{1}{E} \cdot \left[f_x - \nu f_y\right]$$

$$= \epsilon_y ; \qquad (\text{since } f_x = f_y)$$

$$= \frac{0.7 f_x}{E} ; \qquad (\nu = 0.3, \text{ for steel})$$

The energy stored in the diaphragm;

$$S.E. = 2f_x t.\frac{0.7f_x}{E} \quad 4a^2$$

$$= \left[(f_x)^2 t.a^2\right] \quad 1.87 \times 10^{-7}$$

If it is assumed that all this energy is employed in rotating the petals,

then the

$$S.E. = \frac{1}{2} I\omega^2$$

$$= \frac{1}{2} \quad \frac{2\sqrt{3}}{9} \quad a^4(k - \frac{2}{3}) \quad \frac{W}{g} \omega^2$$

Taking a 0.015 in. thick diaphragm as typical of the diaphragms used in the 12"x12" tube,

$$I = 0.009 \quad lb.in.sec.^2$$

and the total elastic strain energy stored,

$$S.E. = 252 \quad lb.in.$$

If it is assumed that this is all divided between the two main petals,

then

$$\frac{1}{2} \times 0.009\omega^2 = 126$$

hence the angular velocity imparted to the main petals as a result of the release of the elastic strain energy is

$$\omega_{S.E.} = 167 \quad rad./sec.$$

DECELERATING FORCES ON THE PETAL.

There are three effects to be considered, which should tend to decelerate the angular motion of the petal.

(a) The torque necessary to overcome the petal root stiffness in bending was considered by Kireyev and shown to be insignificant. Consequently it is ignored in the subsequent analysis.[*]

(b) It is virtually impossible to assess the aerodynamic drag, since the streamlines are controlled by the nozzle configuration. The relative velocities are such, however, as to suggest that the drag will be small. Likewise the pressures are relatively low for most of the opening period. The drag must be considered in any treatment of the petal motion after it has rebounded off the wall.

(c) In certain cases it is obvious that the manner of crack propagation can effect the opening of the diaphragm. This is largely uncontrollable and difficult to describe mathematically. A "good burst" implies that the crack will run at the maximum, brittle fracture, rate and our efforts have been directed to obtaining this condition in our experimental evaluation of scribing techniques. It is thus considered reasonable to assume that this may be accounted for by a starting time t_o.

EQUATION OF MOTION OF THE MAJOR PETAL.

Neglecting all but the static pressure forces on the petal, the equation of motion is,

---

[*] A qualitative assessment of the effect of root bending in the case of a round tube is made on p. 82

$$\ddot{\theta} = c.\ \phi(t), \qquad \ldots.(5.\ 6)$$

where

$$c = 2\sqrt{3}\ \frac{p_4 g}{aW} \cdot \frac{(k+1)}{(3k+2)} \cdot$$

The function $\phi(t)$ describes the variation of the differential pressure with respect to time.

Using the angle θ as the primary variable the conditions on the inlet side of the nozzle may be evaluated. The area ratio $A_{t/A}$ is given by,

$$A_{t/A} = (1 - \tfrac{2}{\sqrt{3}}.\cos\theta) \qquad \ldots.(5.\ 7)$$

and the area ratio $A_{r/A}$ is given by,

$$A_{r/A} = (1 - r.\cos\theta) \qquad \ldots.(5.\ 8)$$

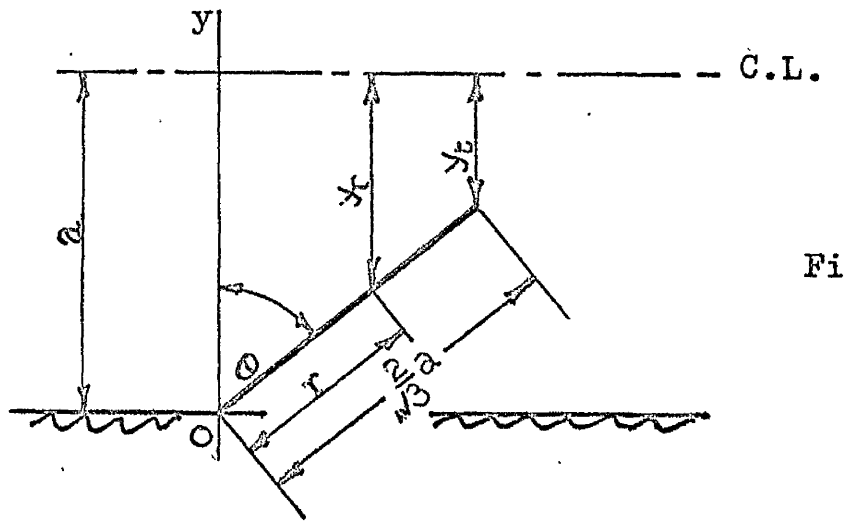

Fig.(5. 5)

The chosen expression for nozzle throat area makes some allowance for leakage past the petal edges.

Using the relationship (5. 7) for the area ratio, the inlet Mach No. M_i, is found from standard isentropic flow tables, ref.(20).

Referring to fig.(5. 1), it will be observed that the isentropic stagnation conditions at the inlet are a function of the throat velocity, which is ,at this stage, unknown.

If the relative velocity $u_w = -u_t$ is superimposed then the appropriate stagnation conditions at inlet to the nozzle are obtained by treating an expansion from $u_4 = u_w$ and a_4 to M_i, rather than from static conditions in region 4.

The distribution of the differential pressure on the petal is a function of Θ and the radial distance r from the root. Considering the upstream side first, the isentropic relation between pressure and area ratio is integrated over the petal radius for incremental values of Θ;

$$\text{ie.} \quad f(\Theta) = \int_0^{\frac{2a}{\sqrt{3}}} (p_r)_{up.} dr, \qquad \ldots.(5.\ 9)$$

where p_r is given by,

$$A_{r/A_t}{}^2 = \frac{\gamma - 1}{2} \cdot \frac{\left[\frac{2}{\gamma} - 1\right]^{\frac{\gamma+1}{\gamma-1}}}{\left[1 - (p_r/p_o)^{\frac{\gamma-1}{\gamma}}\right](p_r/p_o)^{\frac{2}{\gamma}}} \qquad \ldots.(5.\ 10)$$

The solution to equation (5. 10) is to be found in the standard isentropic flow tables. The graphical integration is shown in figs.(5. 9) and (5. 10). The results are universally applicable, since they are independent of petal velocity and time. It should be noted that equation (5. 10) is double valued and that the subsonic values are used for the upstream side of the nozzle throat.

The supersonic solution is used to obtain the downstream pressure ratio p_z/p_o, but since the supersonic portion of the nozzle has a free boundary, the pressure on the petal is independent of the radius r and a function of Θ only. Therefore the fuction $F(\Theta)$ is obtained as,

$$F(\Theta) = \int_0^{\frac{2a}{\sqrt{3}}} (p_r/p_o)_{up.} dr - p_z/p_o \qquad \ldots.(5.\ 11)$$

It should be noted that this is an average uniform differential pressure taken over the whole petal, which is deemed adequate, since $(p_r)_{up.}$ does not vary greatly with r. The petal geometry also minimizes the inaccuracy involved in adopting this simplified pressure distribution, since the area is smallest where the pressure reduction is largest, at the petal tip. The function $F(\Theta)$ is plotted in fig.(5. 11)

The equation of motion may now be written;

$$\ddot{\Theta} = \phi(t) = c.\frac{p_o}{p_4}. F(\Theta) \qquad ....(5.\ 12)$$

The isentropic stagnation pressure at the inlet to the nozzle is evaluated by considering an unsteady expansion from region 4 to inlet, ie. from u_w, a_4 to M_i. For an unsteady expansion, one may say, in general;

$$u + \frac{2}{\gamma - 1}. a = \text{constant} \qquad ....(5.\ 13)$$

hence

$$u_w + \frac{2}{\gamma - 1} a_4 = u_i + \frac{2}{\gamma - 1} a_i \qquad ....(5.\ 14)$$

ie.
$$\frac{a_i}{a_4} = \frac{\frac{u_w}{a_4} + \frac{2}{\gamma - 1}}{M_i + \frac{2}{\gamma - 1}} \qquad ....(5.\ 15)$$

and
$$\frac{u_i}{a_4} = \frac{\frac{u_w}{a_4} + \frac{2}{\gamma - 1}}{1 + \frac{2}{M_i(\gamma - 1)}} \qquad ....(5.\ 16)$$

The slope of the characteristic at the inlet is given by,

$$N_i = \frac{u_i - a_i}{a_4} \qquad ....(5.\ 17)$$

and the stagnation pressure ratio, p_o/p_4, at the inlet to the nozzle is then given by,

$$\frac{p_o}{p_4} = \left[1 + \frac{\gamma_4 - 1}{2} \cdot \left(\frac{N_i + 1}{1 - \beta_4 \gamma_4 N_i}\right)^2\right]^{\frac{1}{2\beta_4}} \cdot \left[1 - \frac{N_i + 1}{\alpha_4}\right]^2 \quad \ldots\ldots(5.\ 18)$$

as derived in ref.(1). The inlet conditions for the nozzle are thus obtained for all values of Θ, using the values of N_i derived in equations (5. 15) - (5. 17). Equation (5. 18) is plotted in fig.(5. 12a), allowing one to obtain the appropriate value of p_o/p_4 for any value of N_i. The value of N_i is, however, a function of the x component of the petal tip velocity, consequently p_o/p_4 must be found by an iteration process. It has been found that the solution converges rapidly and it is our practice to start the calculation with $u_w \simeq 0$.

It is particularly unfortunate that the ratio p_o/p_4 is a function of the coefficient c, since c embraces all the measureable parameters pertaining to the diaphragm. In fact the solution of the equation of motion is relatively insensitive to the nozzle throat velocity and a standard function for the variation of p_o/p_4 with Θ could be adopted for all relevant values of c.

THE APPLICATION OF THE METHOD OF CHARACTERISTICS TO THE FLOW IN A SHOCK TUBE, INITIATED BY A PETALLING DIAPHRAGM.

If one assumes that a supersonic expansion takes place from the nozzle throat to the channel area at some station Z downstream of the throat, then the conditions at Z are known in terms of the inlet conditions;

p_o/p_4 , u_i/a_4 , a_i/a_4 and u_w/a_4 .

These results in conjunction with the initial pressure ratio, p_4/p_1, allow one to establish the starting conditions at Z after the chosen time t_o;

ie.

$$p_z/p_1 = p_z/p_o \cdot p_o/p_4 \cdot p_4/p_1 ,$$

$$u_z/a_4 = u_{ne.}/a_4 + u_t/a_4$$

and $$a_z/a_4 = a_{ne.}/a_4 .$$

With the initial velocity and the speed of sound at Z the pressure is matched to that in the undisturbed channel, region 1, through a shock wave, contact surface and expansion wave or Q shock as appropriate. Thereafter the method of characteristics is applied to evaluate the further effect of the diaphragm.

This solution implies that the free boundary to the supersonic steady expansion moves at the nozzle throat velocity. Such an assumption will have little effect on the final result, if the throat velocity is relatively small. The situation arises with large rapid opening diaphragms that the throat velocity may reach levels comparable with the gas velocity. When these conditions prevail, the following hypothesis may be more realistic.

FORMATION OF SHOCK WAVES AT THE NOZZLE THROAT.

If the boundary downstream of the throat is not moving at the throat velocity, a limiting case may be considered, in which the downstream throat is formed relative to the shock tube walls, which implies an instantaneously stationary nozzle.

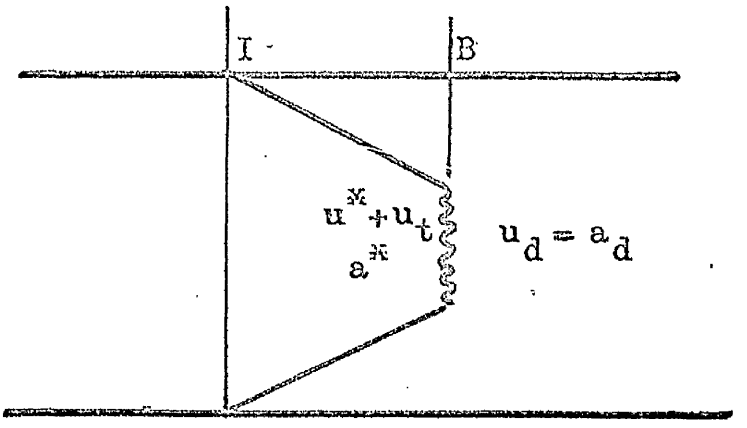

Fig.(5. 6)

The upstream conditions relative to the walls are;

$$\text{gas velocity} = u^{\star} + u_t$$

$$\text{speed of sound} = a^{\star}$$

To obtain throat conditions relative to the walls a backward facing shock must be formed in the region of the throat. This shock will reduce the gas velocity to the downstream value u_d and increase the sound speed to $a_d = u_d$. The value of u_d is obtained by iteration, the method being illustrated by way of example in Table IV on page 81. Thereafter the gas is expanded to the conditions at Z by way of a quasi-steady expansion for the area ratio appropraite to the instant considered. The solution then proceeds as for the isentropic case, with the conditions at Z being matched to those in the undisturbed channel through a shock wave, contact surface and expansion wave, or Q shock, as appropriate. In the continued characteristic solution the entropy increase through the throat based shocks must be included. In addition the downstream pressure must be treated in a step by step fashion, since this is now a function of time and not of area ratio alone, as in the isentropic solution.

It will be noted in the two examples derived, see figs.(5. 13), that the compression waves emanating from

station Z show no tendency to coalesce and thus form secondary shock waves over the primary opening period. When the diaphragm petals rebound from the shock tube wall the conditions at the throat are altered. The sign of u_t is now reversed, thus the gas conditions relative to the tube walls, immediately downstream of the petal tips are,

$$\text{gas velocity} \simeq u^{\text{※}} - u_t$$

$$\text{speed of sound} = a^{\text{※}}.$$

The gas will now undergo a quasi-steady compression to station Z. The P characteristics emanating from Z after rebound will then tend to overtake those formed during the primary opening period. Secondary shocks are then established.

It is virtually impossible to proceed any further with the solution of the equation of motion without experimental information. Immediately prior to the petal striking the shock tube wall the drag assumes some importance and certainly so, after it rebounds off the wall. In addition the amount of energy absorbed on impact, which may be described by the coefficient of restitution, is unknown and must be subject to variation from one specimen to another. the only experimentally determined parameter which has any bearing on these characteristics is the duration of the rebound. Measurements of the rebound time do not contain enough information to allow one to establish either of the unknowns. They do however point to the excessive variation in the rebound characteristics obtained with like diaphragms.

It is worth noting that the interaction of secondary shocks, formed as the result of diaphragm rebound, with the primary shock, does not necessarily preclude the possibility of disturbances, resulting from the opening process, interrupting the quasi-steady flow at the working section. As the diaphragm starts to open again after the rebound it may be likened to the original opening action and one would

expect a similar distribution of compression characteristics, with an even greater dispersion, because of the slower speed.

NUMERICAL SOLUTION IN TWO PARTICULAR CASES.

In the following subsection the two cases considered are;

(a), supersonic isentropic expansion from the throat to station Z,

and (b), supersonic non-isentropic expansion from the throat to station Z.

Similar initial conditions are chosen.

$$c = 2\sqrt{3} \cdot \frac{p_4 \cdot g}{aW} \cdot \frac{k+1}{3k+2}$$

$$= 4 \times 10^6 \quad \text{per sec.}^2$$

The diaphragm chosen is made from mild steel tinplate, 0.017 in. thick and specific weight = 0.71 lb/ft.^{2} The corrected specific weight, W = 0.61 lb/ft.^{2} With k = 1 and a = 5.875 in., the value of p_4 is obtained from the relation above;

$$p_4 = 188 \text{ lb/in.}^2$$

With an initial channel pressure, p_1 = 10 Torr, the initial pressure ratio,

$$p_4/p_1 = 970.$$

An estimate of the starting time, t_o, is made on the basis of the time taken by a sound wave emanating from the centre of the diaphragm to reach the inlet to the nozzle, by which method one obtains $t_o \doteqdot 250$ microseconds. During the period t_o the isentropic stagnation pressure ratio at the nozzle inlet is assumed; $p_o/p_4 = 1$. The angular velocity of the major petals, ω_o, reached at the end of the period t_o is then,

$$\omega_o = c.t_o$$
$$= 1.0 \times 10^3 \text{ rad/sec.}$$

These assumptions imply that the rupturing process offers no restraint to the motion of the petals.

The solution of the equation of motion is now,

$$\omega^2 = 2c. \int_{\Theta=30^o}^{\Theta=90^o} p_o/p_4 . F(\Theta) . d\Theta$$

The solution in case (a) may be obtained by successive approximation, using the information presented in fig.(5. 12a) for the variation of p_o/p_4 with Θ as initial values, in conjunction with the boundary condition,

$$\omega_{(30^o)} = \omega_o = 1.0 \times 10^3 \text{ rad/sec.}$$

In practice it has been found that p_o/p_4 is relatively insensitive to changes in ω and that fig.(5. 12a) may be taken as valid for all ω.

In case (b) the function $F(\Theta)$ is no longer valid as plotted in fig.(5. 11) and a step by step solution involving successive approximations is once again necessary to solve equation (5. 11).

(a) Supersonic Isentropic Expansion to Station Z.

Table II, overleaf, shows the condensed calculation of the diaphragm petal trajectory and illustrates the relative insensitivity of the calculation to significant variations in the values of p_o/p_4.

θ	30°	40°	50°	60°	70°	80°	90°
p_o/p_4	.565	.565	.565	.565	.565	.565	.565
$F(0)$	1.000	.963	.900	.800	.686	.500	0
t, $\mu s.$	250	400	520	624	718	805	889
u_t/a_4	.419	.494	.493	.431	.320	.173	0
p_o/p_4	.628	.572	.554	.549	.548	.548	.528
t, $\mu s.$	250	399	517	620	713	800	884
u_t/a_4	.419	.501	.497	.434	.321	.173	0
p_o/p_4	.628	.571	.553	.548	.548	.548	.528

Table II.

Since the differences between the second and third approximations are insignificant, the outlet conditions are obtained from the second. The characteristic solution is based on the assumption that the quasi-steady nozzle flow is established when $\theta = 40^\circ$ and the conditions at Z at this time are matched to those in the undisturbed channel through a shock wave, contact surface, etc.

θ	40°	50°	60°	70°	80°	90°
A_t/A	.115	.258	.423	.605	.800	1.000
M_z	3.76	2.907	2.383	1.975	1.600	1.000
p_z/p_o	.009	.031	.070	.132	.235	.528
a_z/a_4	.455	.536	.599	.661	.727	.833
$u_z/a_4 + u_t/a_4$	2.212	2.055	1.861	1.626	1.336	.833

Table III.

At $\Theta = 40^{\circ}$;

$$\frac{u_z}{a_4} + \frac{u_t}{a_4} = 2.212 \quad \text{and} \quad \frac{a_z}{a_4} = .455$$

have to be matched to

$$\frac{u_1}{a_4} = 0 \quad \text{and} \quad \frac{a_1}{a_4} = 1.0,$$

through a pressure differential,

$$\frac{p_z}{p_1} = \frac{p_z}{p_o} \cdot \frac{p_o}{p_4} \cdot \frac{p_4}{p_1}$$

$$= 5.06$$

Referring now to Table 1a , ref.(21),

when

$$\triangle u/a = 2.212 \quad \text{then} \quad p'/p = 10.26 > 5.06,$$

therefore the match is made through a Q-shock, contact surface and a P-shock. The appropriate shock strengths are determined by iteration, utelising the data tabulated in Table 1a of ref.(21). The complete solution is illustrated in fig.(5. 13).

(b) Supersonic Nonisentropic Expansion to Station Z.

The isentropic solution is used as a first approximation in determining the throat conditions. In the course of calculating the isentropic solution the value of $^{a}i/a_4$ is found for each increment in Θ. The local speed of sound at the petal tips is then given by $^{a}t/a_4 = .913.\,^{a}i/a_4$. The iteration procedure is illustrated in Table IV, for the case,

$$\Theta = 40^{\circ}, \quad ^{u}t/a_4 = .501 \quad \text{and} \quad ^{a}t/a_4 = .812.$$

A guess is made for the value a'/a, see Table 1a , ref.(21)

a'/a	M_s	a'	$\triangle u/a$	$\triangle u$	$a^{*}-u_t$	$a^{*}-u_t-\triangle u = u'$
1.120	1.399	.915	.570	.463	1.313	.850
1.100	1.329	.893	.481	.391	1.313	.922
1.107	1.355	.898	.514	.417	1.313	.896

Table IV.

The process is repeated for the remaining values of Θ. A quasi-steady expansion is now assumed in order to obtain the conditions at Z. The value p_z/p_4 can be calculated and is used to find a better value for equation (5. 11). The calculation is repeated until the values obtained for p_z/p_4 have suitably converged.

The final outlet conditions at Z are then obtained and the characteristic solution follows as before. In this case it was found necessary to use a further unsteady expansion from Z to match the gas conditions at outlet to those in the channel. In order to assist in this calculation a graphical solution of the equation;

$$\frac{p}{p_o} = \left[1 - \frac{1}{\alpha_o}(N + 1)\right]^{\frac{1}{P}}_{o} \quad ,$$

for the static pressure ratio in a rarefaction wave has been plotted in fig.(5. 14).

RESULTS OBTAINED FROM THE THEORETICAL SOLUTIONS.

(a) A comparison of the two solutions shown in figs. (5. 13) reveals that, for the particular cases considered, the existence of backward facing shocks in the region of the throat has a negligible effect on the petal trajectory.

(b) The analysis does not predict the gain in Shock Mach No. relative to the ideal case, which is frequently ob-

served and considered by White in ref.(13). A case may be made for employing a hybrid solution using the formation from compression concept until such time as the gas conditions at Z are matched to those in the channel.

(c) For all the cases considered the petal trajectory may be described by the curve appropriate to the scribe pattern as shown in fig.(5. 15).

(d) Generally, experimental observations of the petal trajectories, refs.(21) and (22), of circular diagonally scribed diaphragms indicate a slowing up of the opening process as the petals approach the fully open position, see fig.(5. 16). A qualitative explanation for this phenomenon is readily made.

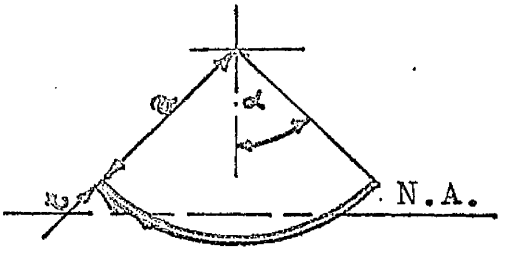

Fig.(5. 7)

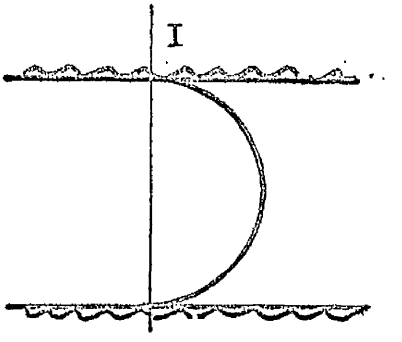

Fig.(5. 8)

Consider plane bending of the section shown in fig.(5. 7), which represents the root section of the petal, then;

$$\frac{I}{y} = \frac{a^3.t(\alpha - \sin\alpha.\cos\alpha.)}{a.(\frac{\sin\alpha}{\alpha} - \cos\alpha)} = Z$$

$$= 1.465\ a^2t \qquad \ldots \text{(when } \alpha = 45^\circ)$$

The restraining torque T_b resulting from the bending of the root section is

$$T_b = f.Z = I_p.\ddot{\theta}_b ,$$

where I_p, the moment of inertia of the petal, about an edge,

is given by equation (5. 4); substituting, the deceleration caused by root bending is

$$\ddot{\theta}_b = 1.465\, a^2 t.f \; \frac{1}{\frac{2\sqrt{3}}{9} a^4 (k + \frac{2}{3}) \cdot \frac{W}{g}} .$$

Letting k = 0, for diagonal scribing,

then

$$\ddot{\theta}_b = 5.71 \frac{fgt}{a^2 W} = \text{constant}$$

It is very difficult to assess the validity of this expression. Referring to fig.(5. 8), if the diaphragm blows to a full hemisphere, which is the theoretical maximum deformation, which it can undergo prior to rupture, then the expression is not valid at all and the opening is more in the nature of an unfolding process, which can hardly be described by the plane petal approximation at all. On the other hand with large diameter thin diaphragms, which tend to allow a minimum of deformation prior to bursting, it should apply over part of the trajectory. This size effect in the root bending restraint is seen, when one compares the trajectories, shown in fig.(5. 16), of a small Copper bursting disc, ref.(22) and a large Aluminium diaphragm, ref.(21).

It has not proved possible to find a consistent basis for assessing the time t_o and the initial angular velocity ω_o. The method adopted in this report is believed to be a reasonable representation of the initial conditions in our particular case. The crack is assumed to run at the brittle fracture rate, approximately 17,000 ft/sec., appropriate for mild steel. On this basis the crack should be fully developed in less than 50 microseconds, which should be compared with t_o = 250 microseconds, the time taken for a sound wave leaving the centre of the diaphragm to reach the nozzle inlet. It is evident from the scatter in our measurements of

opening times, that the cracks do not, in general, behave in this idealised manner. With more ductile materials the problem is aggravated. Measurements of opening time are subject to some uncertainty, since no single criterion has been established to signify the beginning of the opening process. Our own experience indicates that opening times can differ by a factor of 2, depending only on the method of detecting the commencement of rupture. Pierced diaphragms lend themselves to positive triggering, since the instant the plunger strikes the diaphragm is readily detected.

The slowing up of the petal over the latter part of its trajectory is a particularly undesireable feature. The difference between the slope of the characteristics and the shock wave, as plotted on the x-t diagram decreases as the throat aperture increases, consequently small increases in opening time over this period lead to disproportionately long "shock formation distances." A similar argument suggests that delays may be incurred at the start, without undue penalty being placed on the "shock formation distance". Other factors relevant, in particular, to the matching conditions are affected by t_o and ω_o. Further investigation is necessary before these factors and their effect on the subsequent flow can be assessed.

(e) Entropy increases at the diaphragm reduce the "shock formation distance". The distances obtained in solutions (a) and (b) are 17 feet and 16 feet respectively.

(f) Variations in the state parameters behind an incompletely developed shock wave may lead to anomalous results in studies, which utelise the shock as a temperature pulse. Fig.(5. 17) shows the theoretical rise in 'Static Temperature' and'Static Pressure' with time, at stations 12.5 feet and 21.25 feet, as given by solution (b). These positions represent stations before and after the shock is formed.

(g) The shock is not fully formed when the P characteristic, which leaves the diaphragm as it strikes the wall of the tube, reaches the primary shock wave. It may, however, be assumed to be a valid criterion for "shock formation," if the petal does not rebound off the wall.

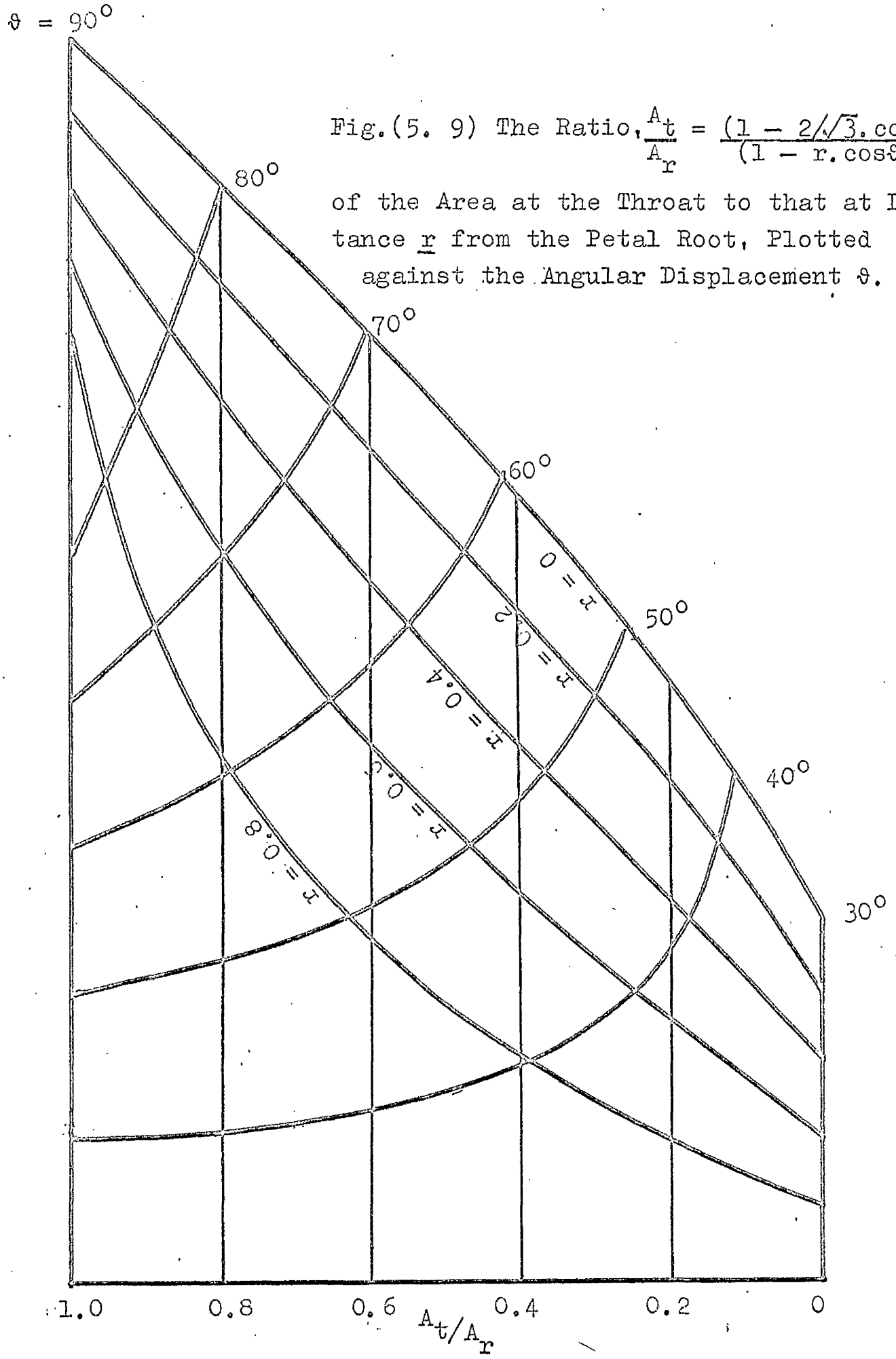

Fig.(5. 9) The Ratio, $\frac{A_t}{A_r} = \frac{(1 - 2/\sqrt{3}.\cos\vartheta)}{(1 - r.\cos\vartheta)}$, of the Area at the Throat to that at Distance r from the Petal Root, Plotted against the Angular Displacement ϑ.

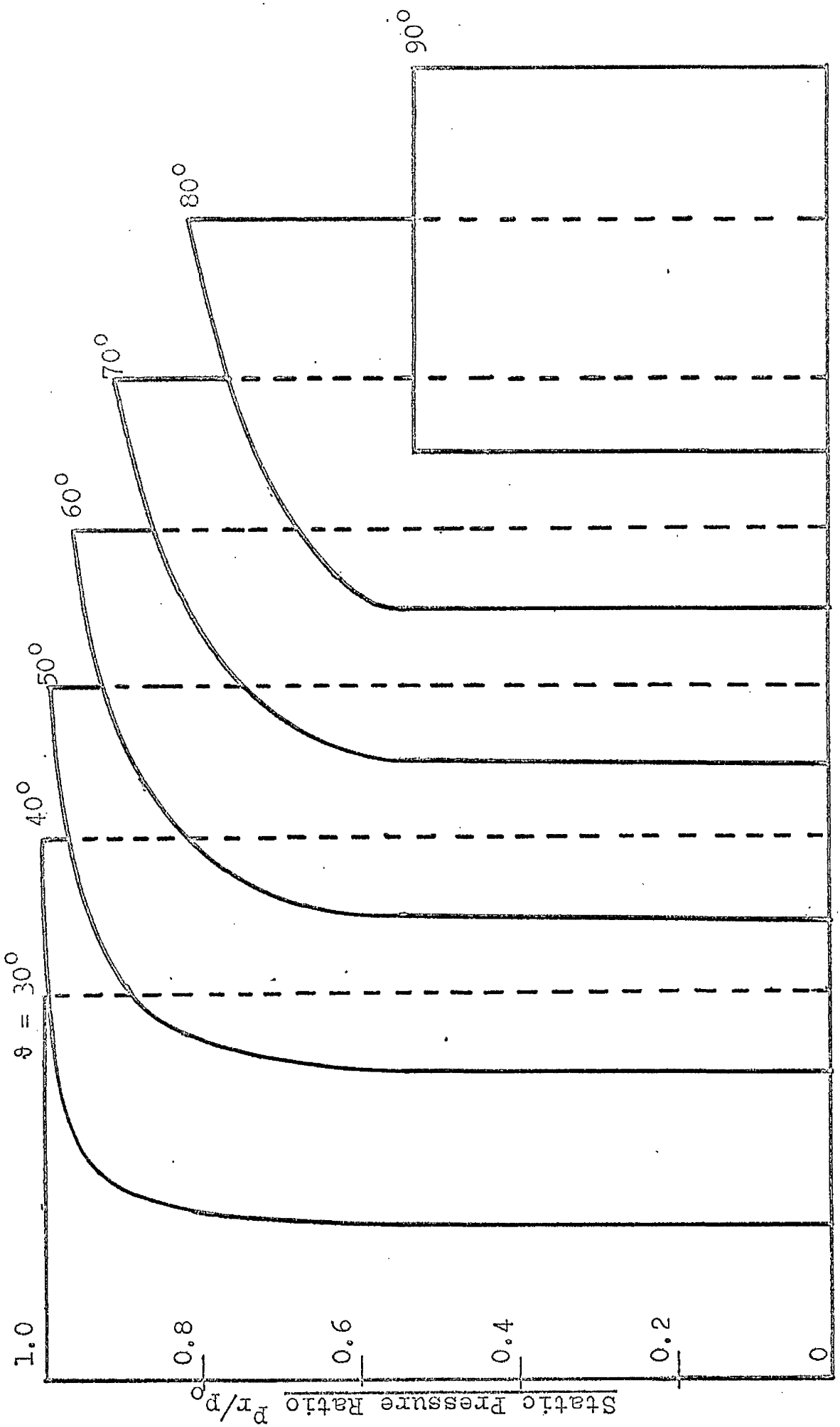

Fig.(5. 10) Static Pressure Distribution on the Upstream Side of the Petal Plotted against Angle ϑ

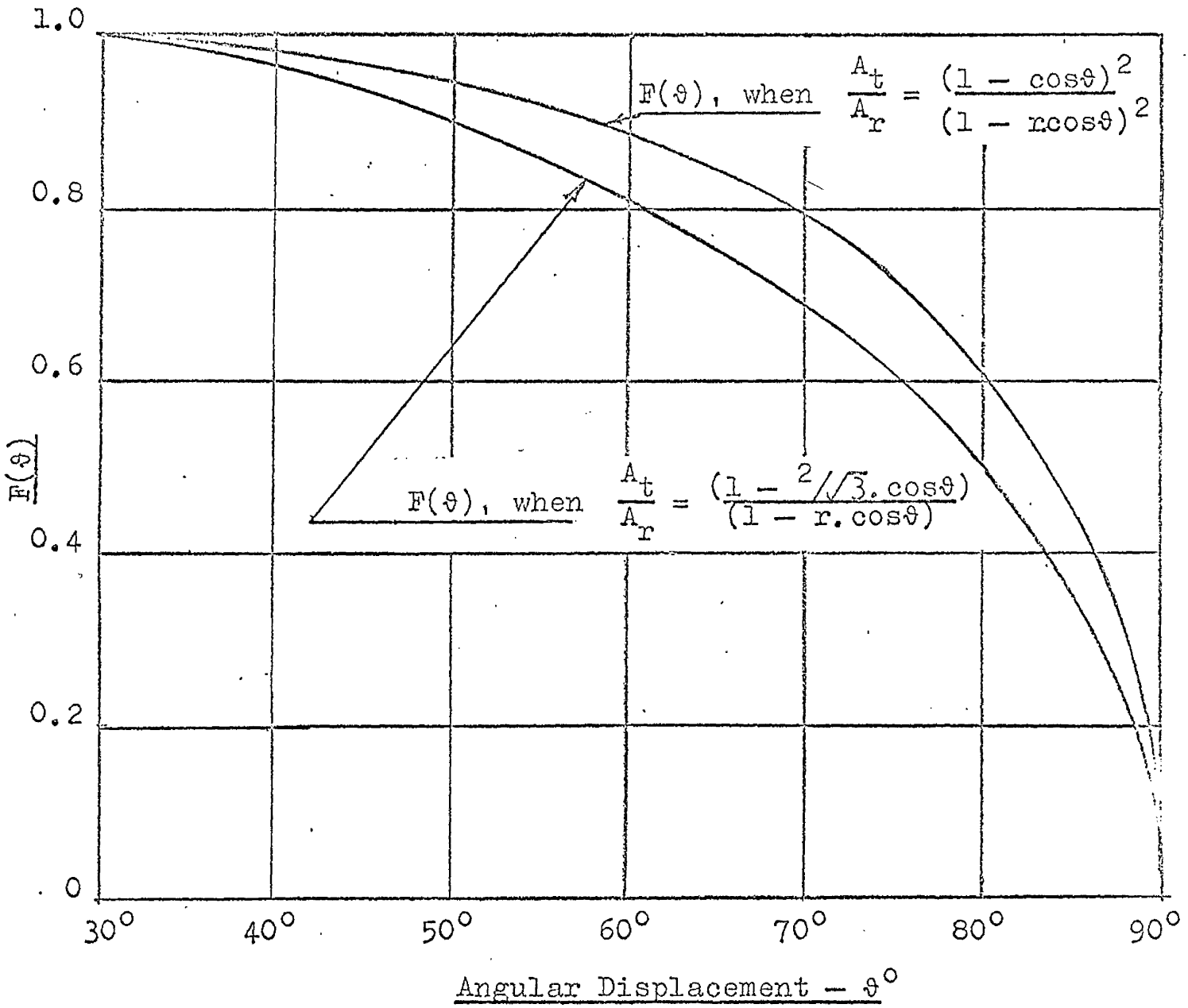

Fig.(5. 11) Differential Pressure Distribution Function F(ϑ) Plotted against Angle ϑ.

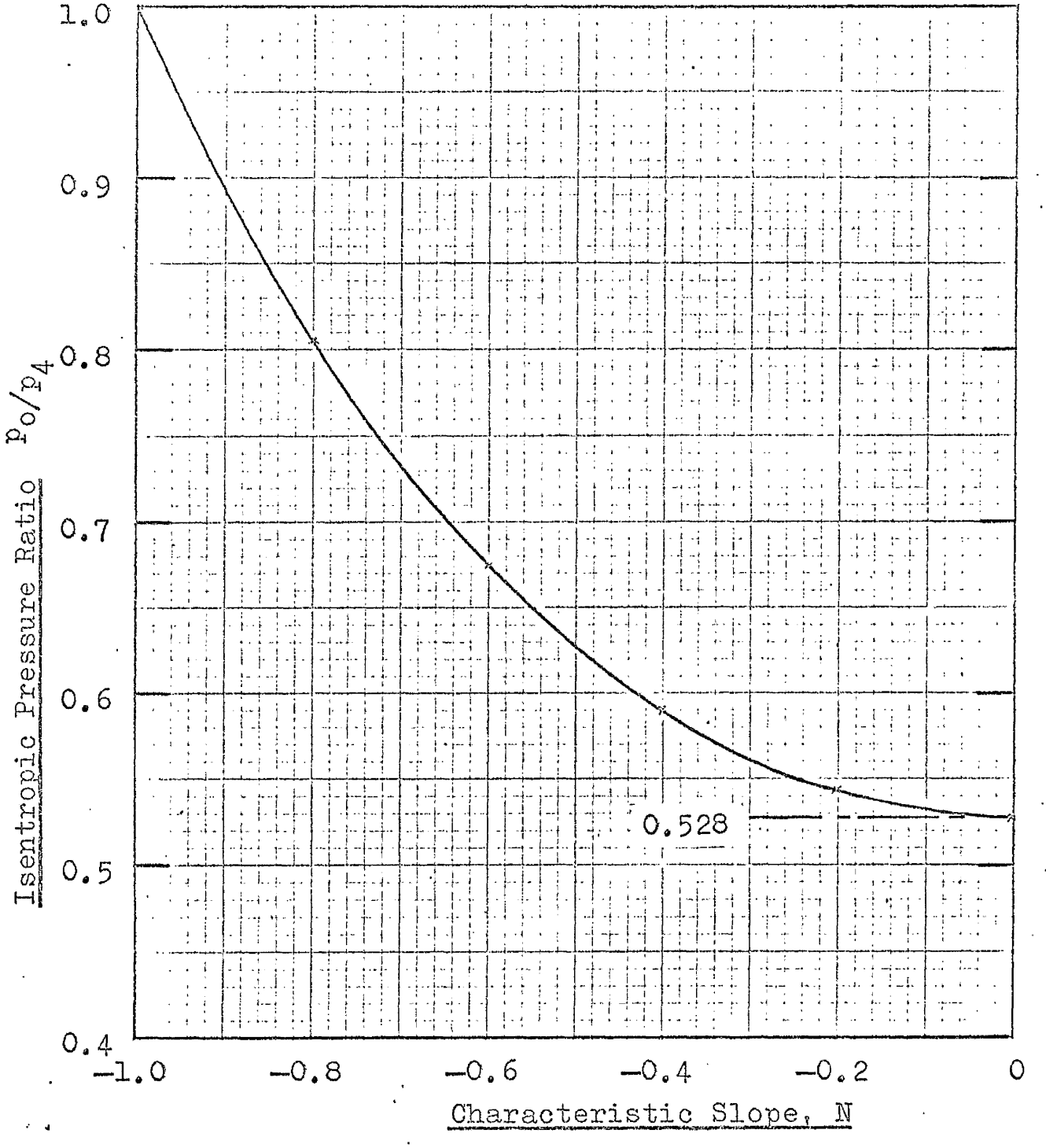

Fig.(5. 12) Variation of the Isentropic Pressure Ratio with Characteristic Slope N.

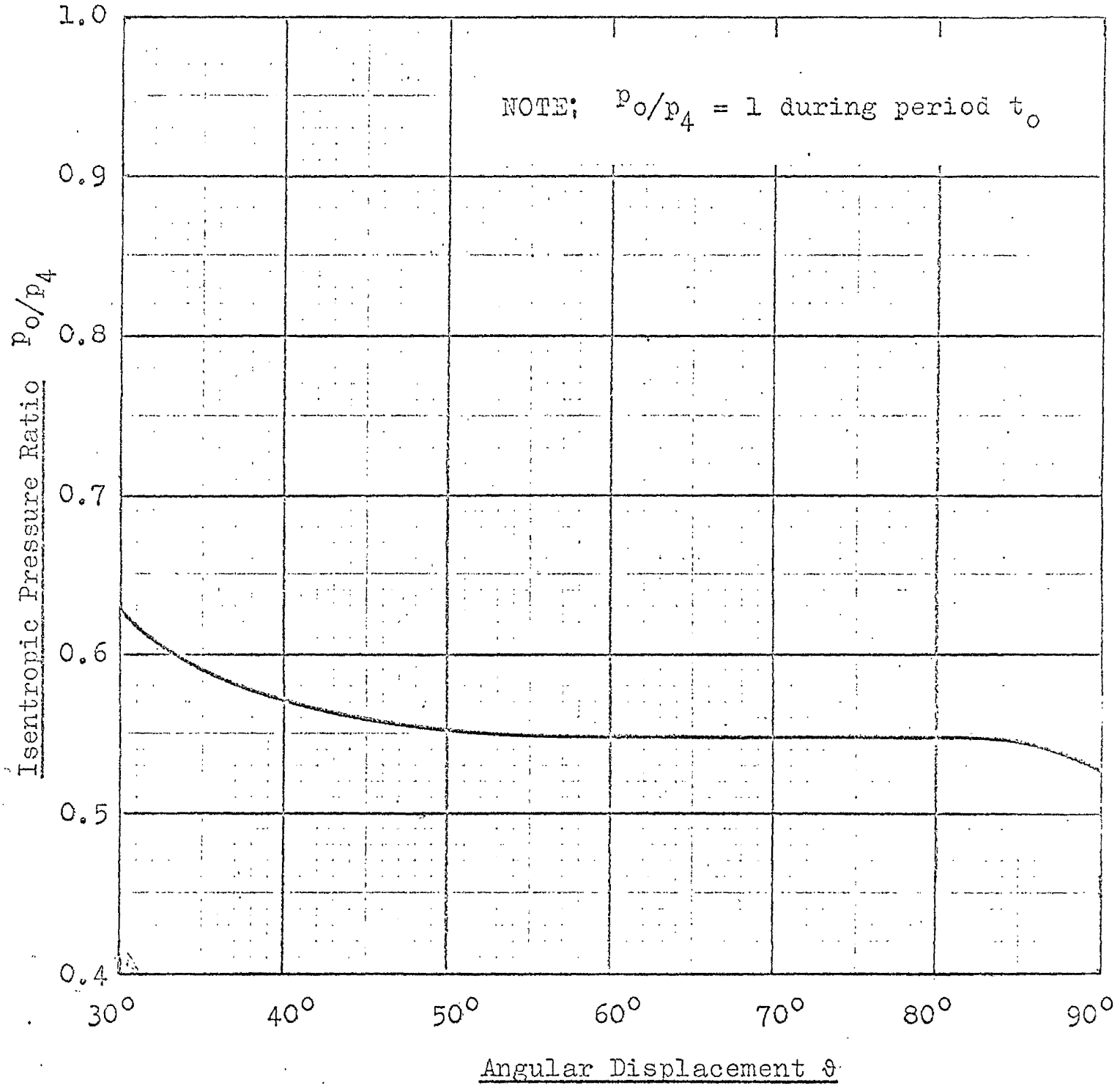

Fig.(5. 12a) Variation of Isentropic Pressure Ratio with Angular Displacement ϑ.

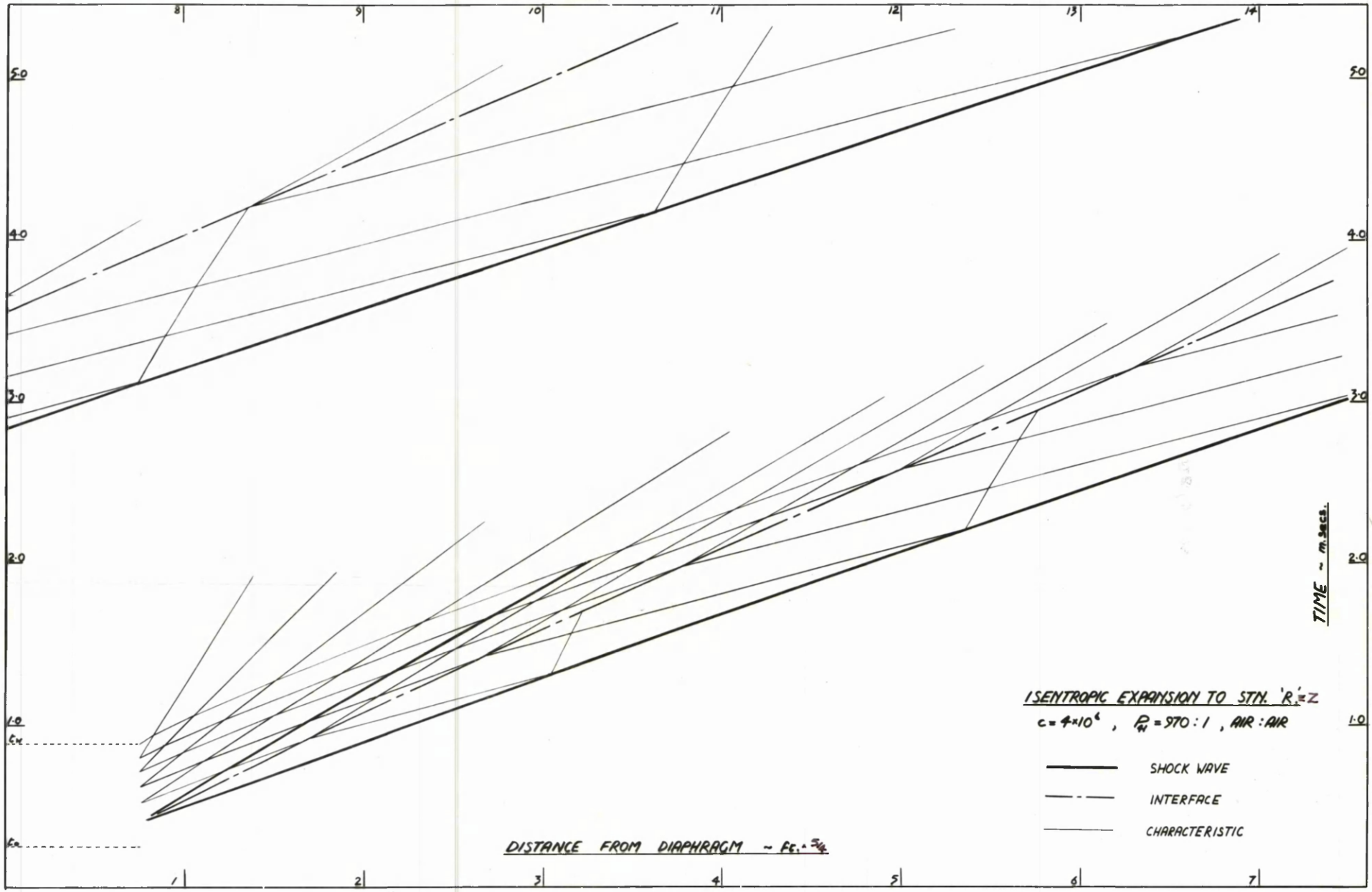
8
9
10
11
12
13
14
5·0
4·0
3·0
2·0
1·0
t_x
t_0
1
2
3
4
5
6
7
TIME ~ m.secs.
ISENTROPIC EXPANSION TO STN. 'R₄' ≡ Z
c = 4×10⁶ , P_N = 970 : 1 , AIR : AIR
SHOCK WAVE
INTERFACE
CHARACTERISTIC
DISTANCE FROM DIAPHRAGM ~ Fts.

Fig. (5. 13a)

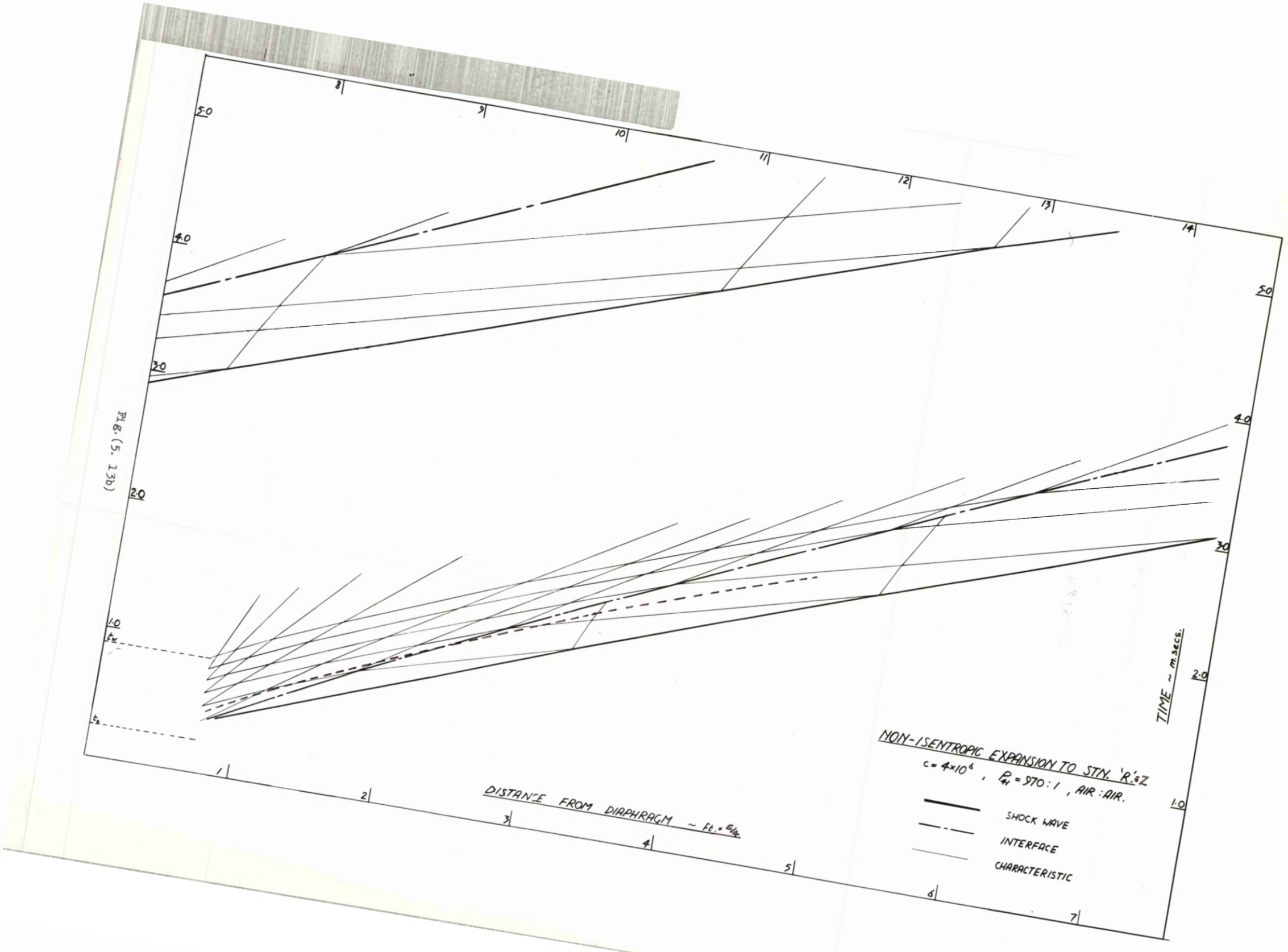
8
9
10
11
12
13
14
5·0
4·0
3·0
2·0
1·0
t_2
t_1
1
2
3
4
5
6
7
DISTANCE FROM DIAPHRAGM ~ Ft. = $\frac{6}{4}$
TIME ~ m.secs.
NON-ISENTROPIC EXPANSION TO STN. 'R.' IN Z
$c = 4\times10^{6}$, $P_{41} = 970:1$, AIR : AIR.
SHOCK WAVE
INTERFACE
CHARACTERISTIC

Fig. (5. 13b)

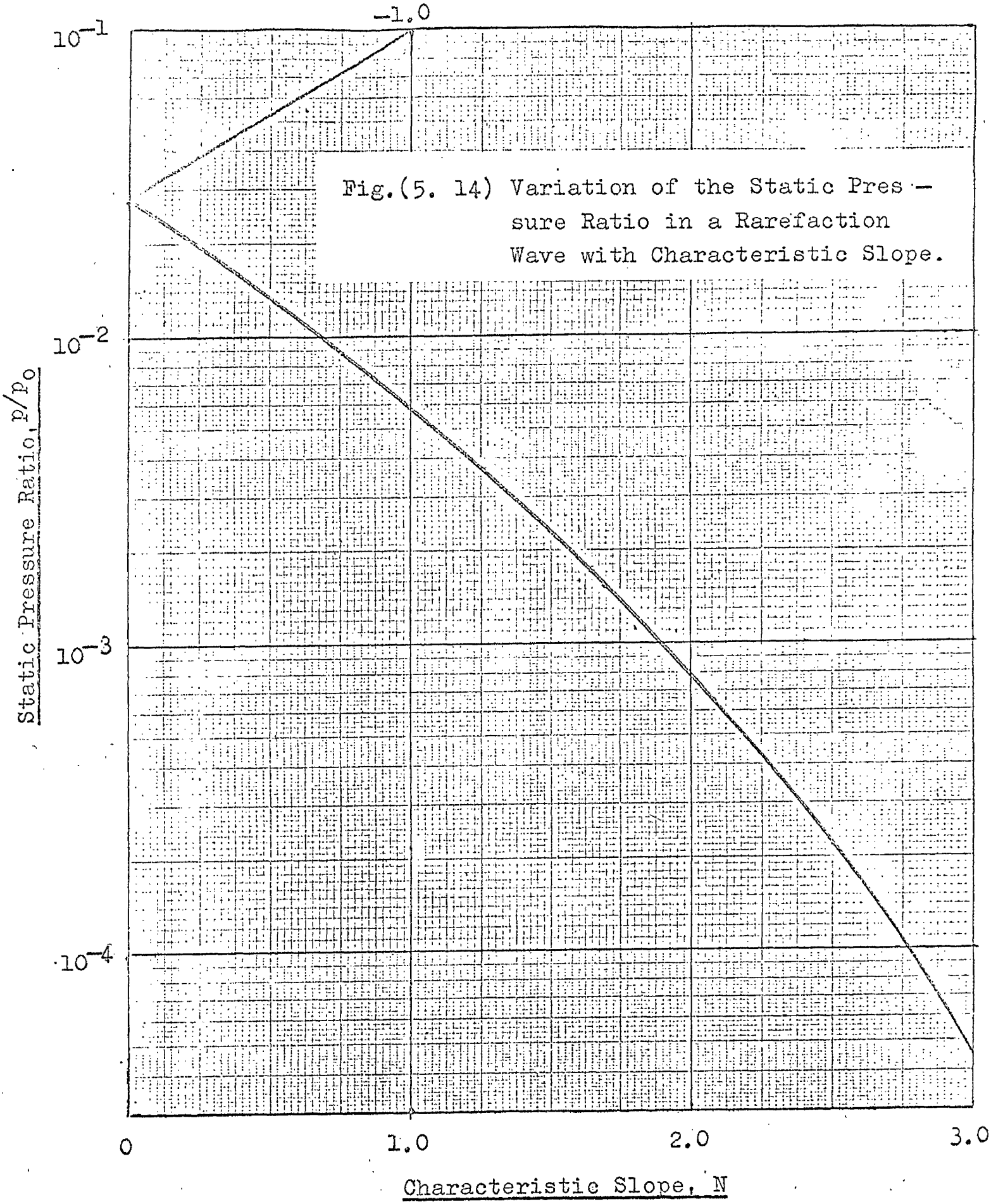

Fig.(5. 14) Variation of the Static Pressure Ratio in a Rarefaction Wave with Characteristic Slope.

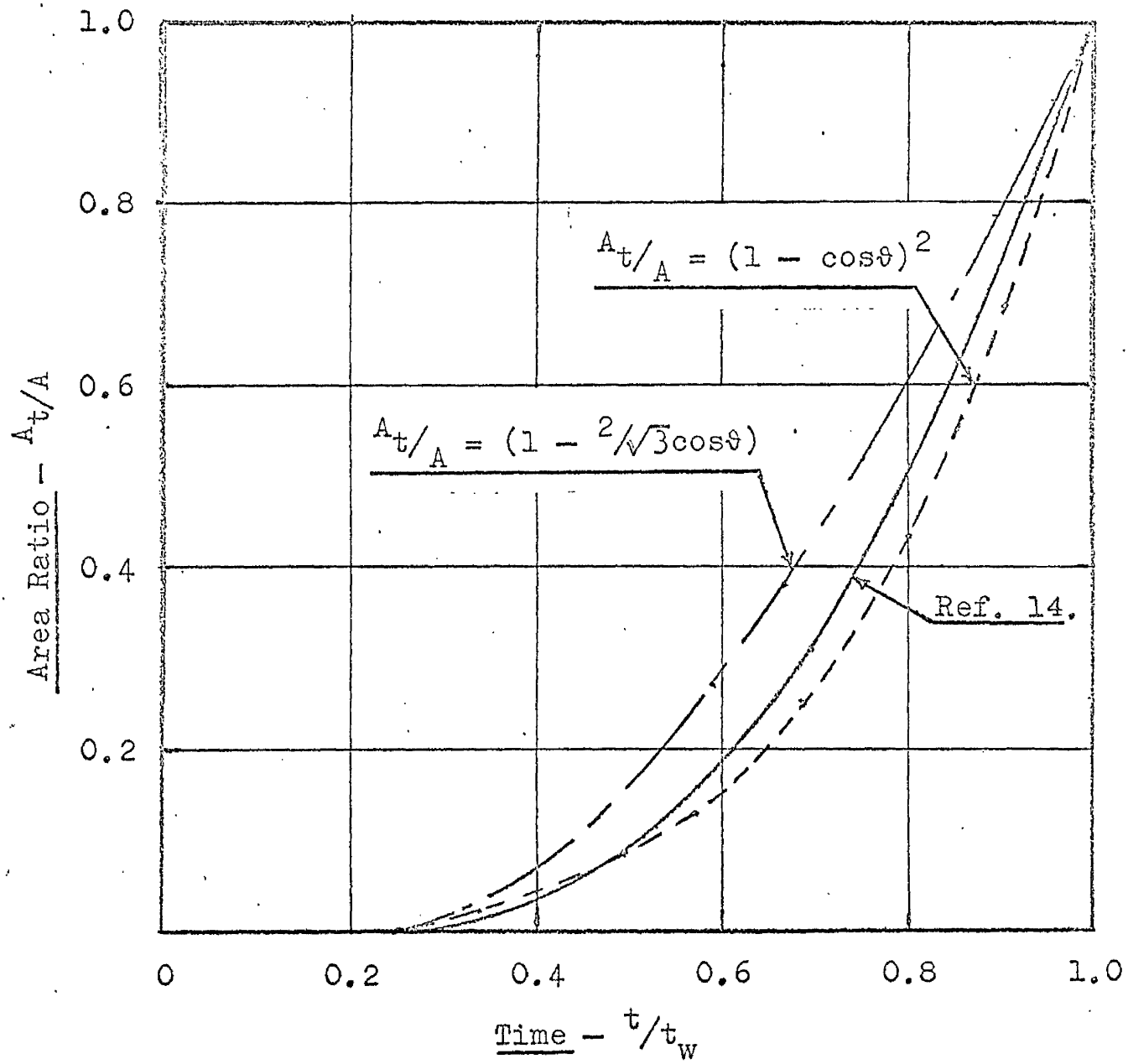

Fig.(5. 15) Timewise Variation of Throat Area Ratio

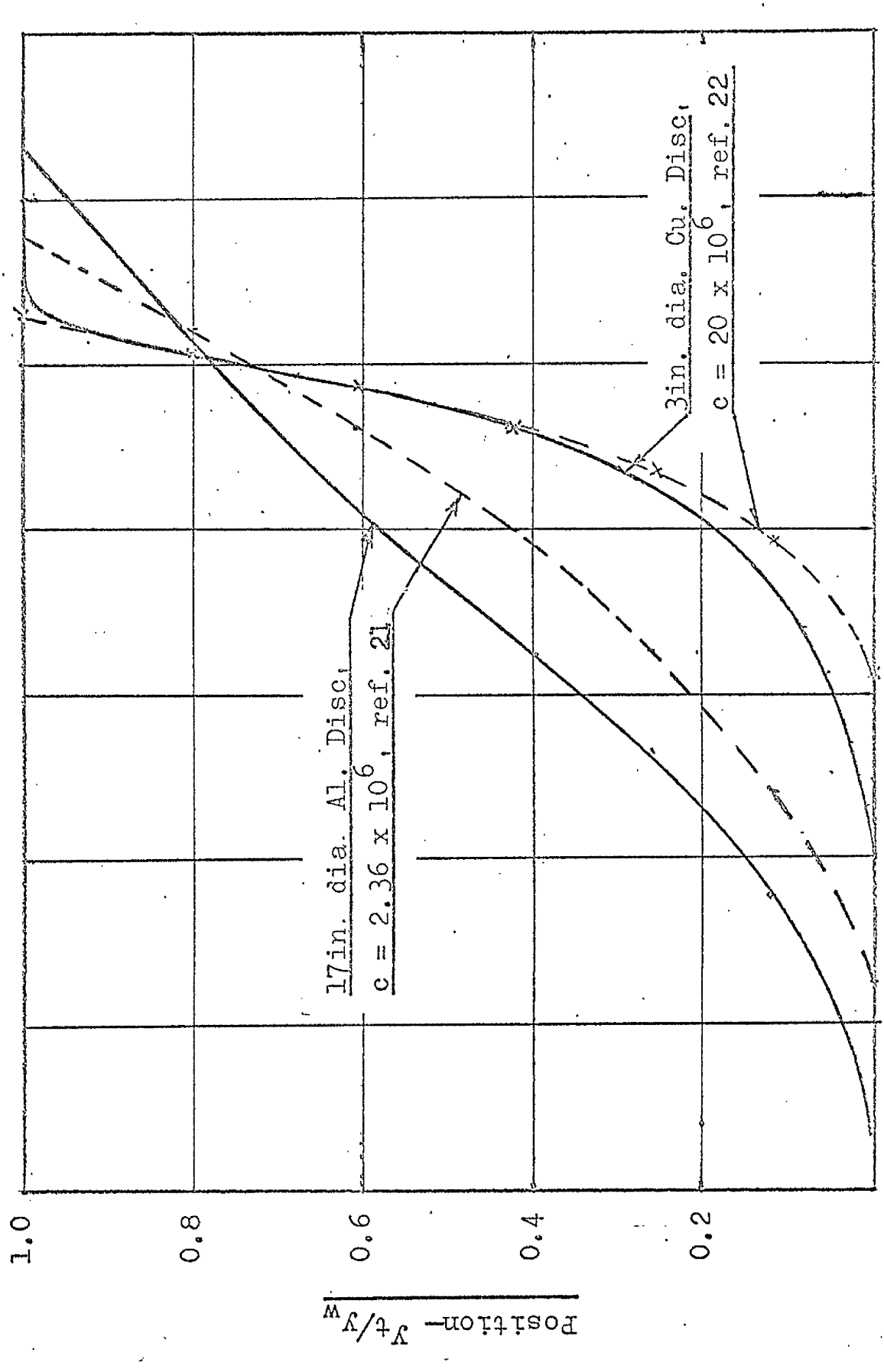

Comparison of Theoretical and Experimental Diaphragm Trajectories.

Fig. (5. 16)

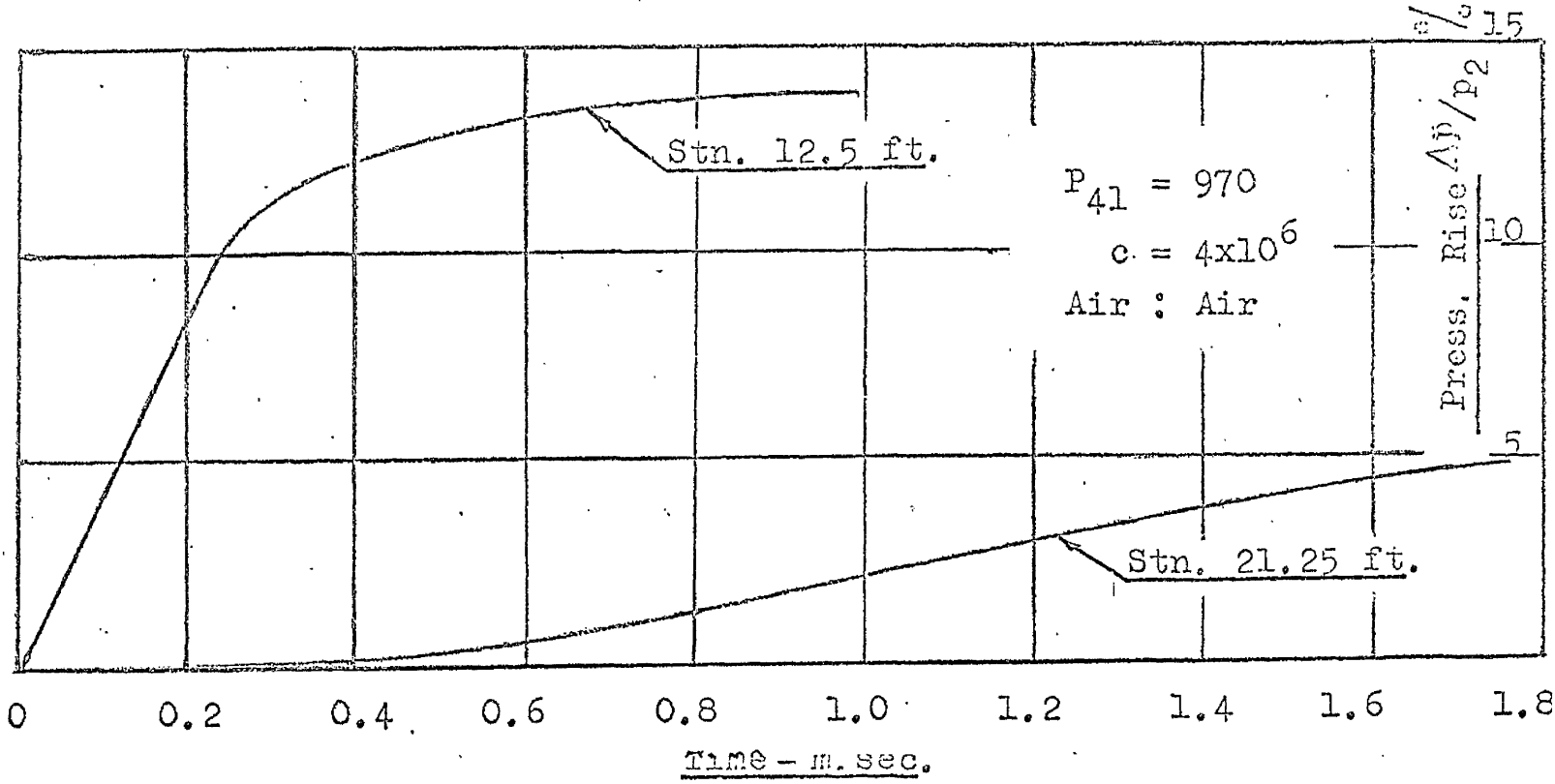

The Theoretical Pressure Rise at a Fixed Station Behind the Incident Shock.

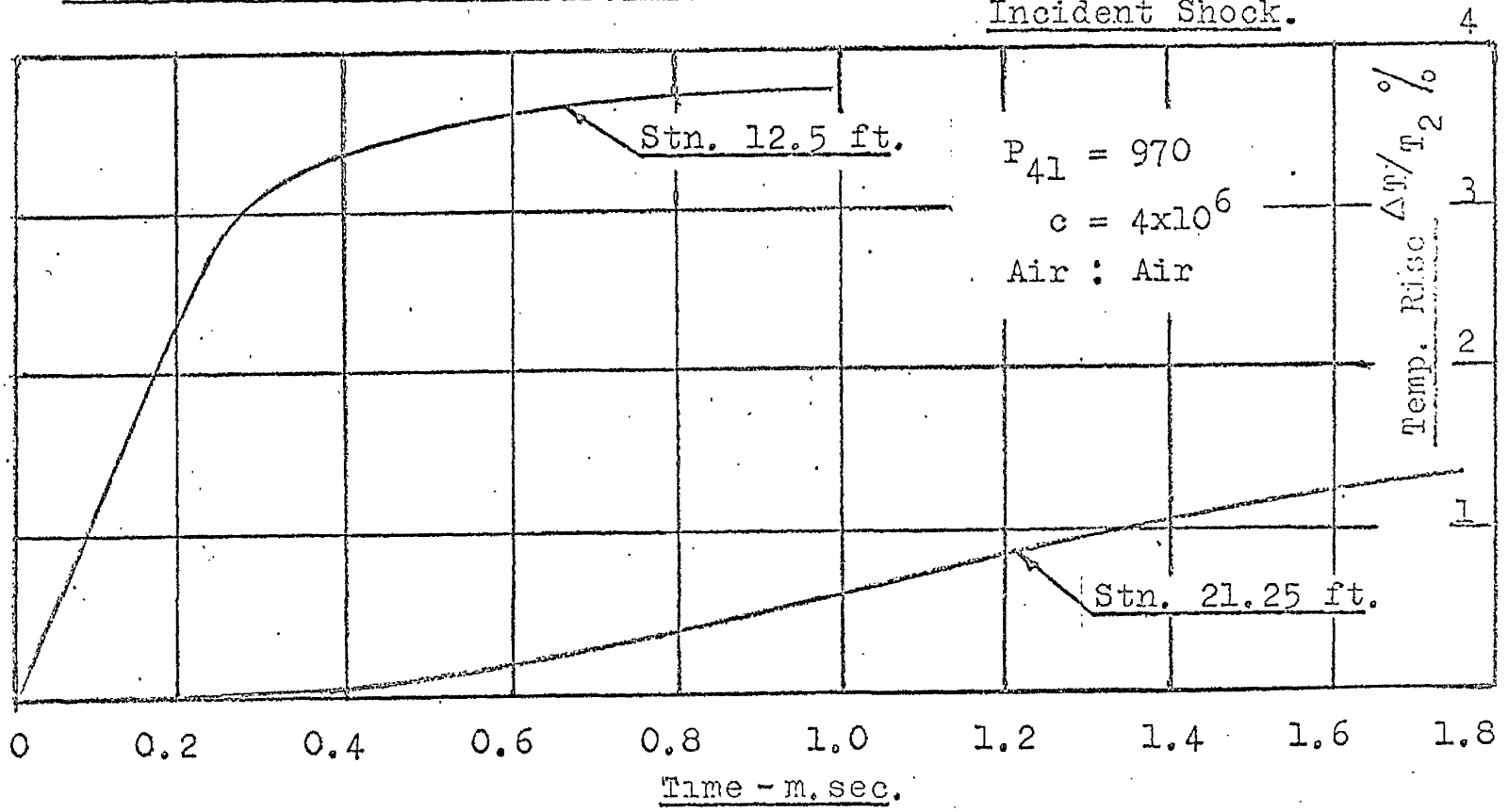

The Theoretical Temperature Rise at a Fixed Station Behind the Incident Shock.

Fig.(5. 17)

PLATE X.

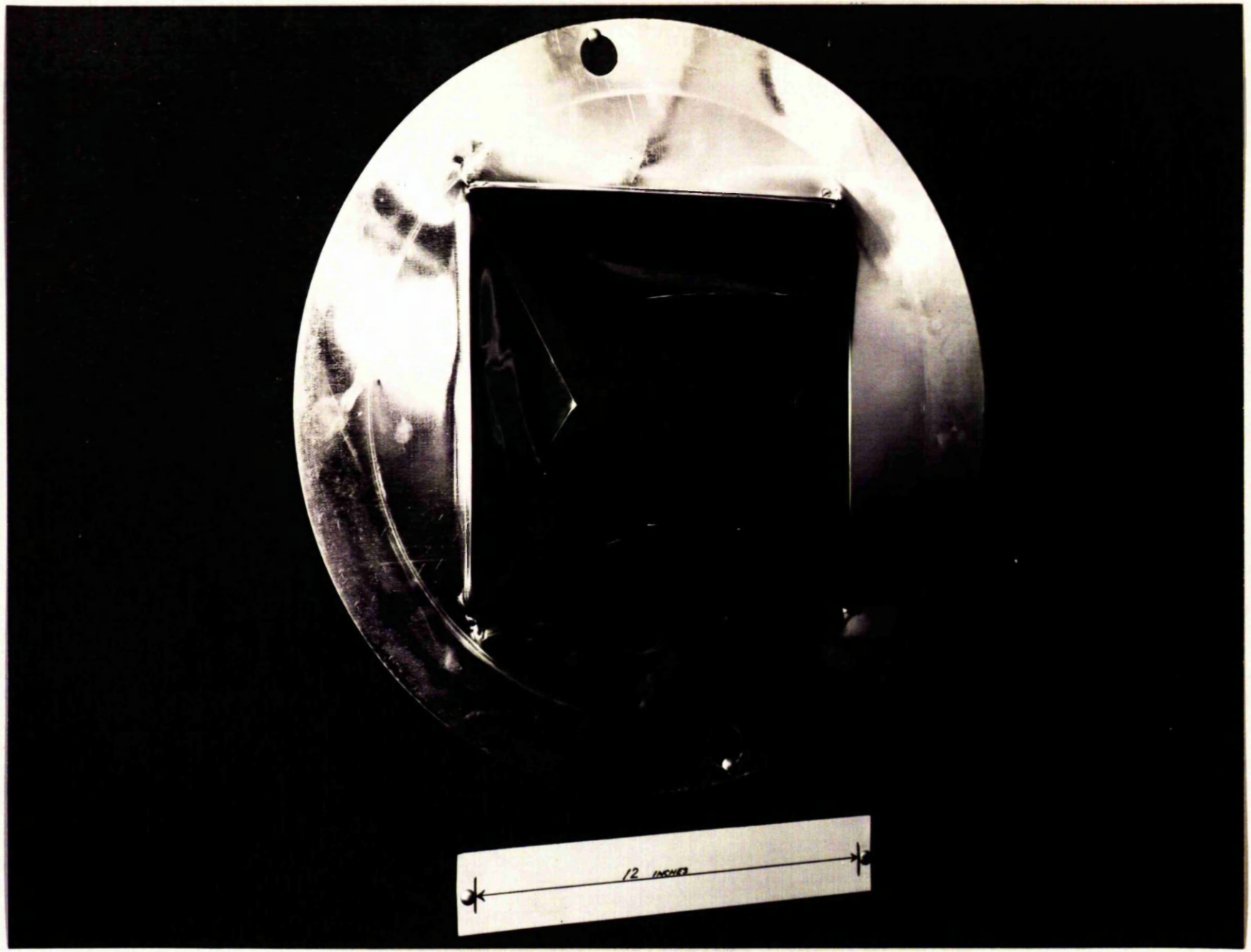

Prescribed Diaphragm, After Rupture

CHAPTER 6.

EXPERIMENTAL RESULTS

EXPERIMENTAL RESULTS

INTRODUCTION

The experimental results presented in this chapter are not the product of a programme established to verify the theoretical work presented in Chapter 5, but rather the preliminary data obtained in the course of developing the instrumentation and in the efforts to establish a consistent mode of diaphragm operation. These results, in fact, precipitated the theoretical analysis.

DIAPHRAGM RUPTURE.

Economic considerations dictated the choice of mild steel as a diaphragm material. Thin steel sheet can be readily obtained in thicknesses of 0.010 - 0.011 inches, 0.016 - 0.017 inches and 0.019 - 0.020 inches. With these gauges of material it has proved possible to cover the range of bursting pressures from 70 to 220 psi. Initially diaphragms were burst in the unscribed condition, with fairly consistent bursting pressures, but the measured Shock Mach Nos. were subject to wide and random variation. In addition, in many cases it was found that pieces of diaphragm had been lost during the burst. Such fragmentation of the diaphragm could not be tolerated, since it would lead to damage of the windows, or stagnation probes, when fitted. Consequently no further attempts were made to operate with unscribed diaphragms.

After a number of trial firings with scribed discs, it was decided to examine the effect of scribing with tensile specimens, which were loaded in a Tensometer. Specimens were prepared, 6 inches long by $\frac{1}{2}$ inch wide in the two gauges of material then available; 0.011 inches and 0.019 inches. The results obtained with the thicker specimens are tabulated below in Table V. The results obtained with the thinner spe-

cimens proved to be useless, because the steel, from which they had been made, was totally unsuitable as a diaphragm material.

Specimen	L_y	L_f	$f_{ult.}$
1	0.160	0.193	
2	0.160	0.192	
3	0.160	0.192	
4	0.159	0.192	
5	0.158	0.191	
Av.	0.159 T.	0.192 T.	20.5 T/in.^{2}

(0.019 in. thick unscribed)

Specimen	L_y	L_f	$f_{ult.}$
1	0.159	0.190	
12	0.158	0.189	
13	0.158	0.190	
14	0.164	0.191	
15	0.160	0.188	
Av.	0.160 T.	0.190 T.	20.3 T/in.^{2}

(0.019 in. thick scribed)

Table V.

It was found to be necessary, in order to ensure consistent failure at the scribe line, to use about ten heavy strokes with a hardened steel pointer. The form and depth of the groove obtained with this technique was observed in the projection microscope and is sketched in fig.(6. 1)

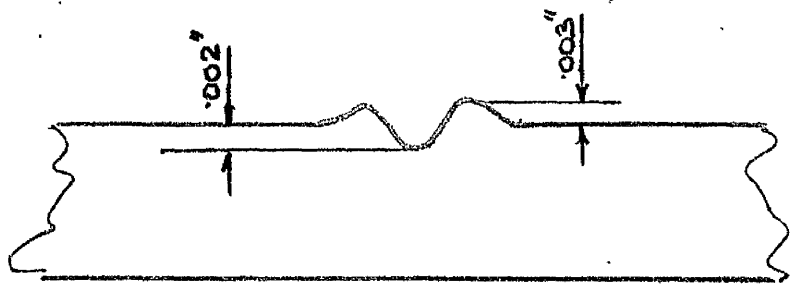

Fig.(6. 1)

Illustrated in fig.(6. 11) is a recording of the stress-strain characteristics of a typical unscribed tensile specimen. Superimposed on this is a similar record, obtained from a scribed specimen and one will note that the only detectable difference between the two traces is the degree of strain at failure. Variations in the strain to failure were considerable for all specimens, particularly so, in the scribed cases. The figures for strain to failure have not been presented, since the maasurements were quite rudimentary, except for the two instances,where the characteristic was recorded.

Latterly the pointed scriber was discarded and a more sophisticated tool adopted, which caused less local hardening of the steel. It proved possible,with one even stroke of this tool, to make scribed bursting discs, which petalled perfectly. No specimens were prepared and tested with this type of scribe, but the random variations in disc bursting pressure indicate that the strain to failure is still not uniform after scribing.

The relationship between the rupturing pressure and the strain to failure may be seen from the following:

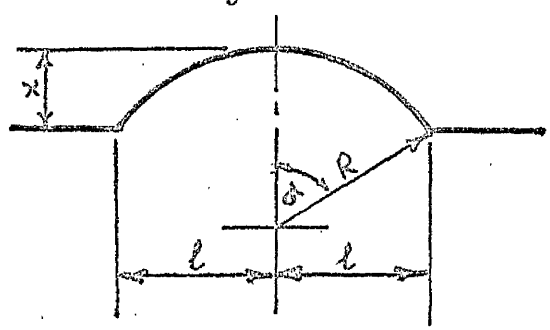

Fig.(6. 2)

$$P_b = 2f_{ult.}\frac{t}{R} \quad \ldots.(6.\ 1)$$

$$\alpha R = a(1 + \epsilon) \quad \ldots.(6.\ 2)$$

Bursting pressure, based on an ultimate tensile stress $f_{ult.} = 20.5\ T/in.^2$, is plotted for the three gauges of steel in use, against the radius of curvature R in fig.(6. 7). The radius of curvature may be evaluated from measurements of the centre displacement x, by reference to fig.(6. 8).

Utelising equations (6. 1) and (6. 2) in conjunction with the relationship $\frac{a}{R} = \sin\alpha$, then the effect of variations in the strain to failure may be calculated. The function $P_b/_t$ has been plotted for the range, $10\% < \epsilon < 30\%$. It should be noted that the strain to failure in the case of the diaphragm, undergoing biaxial loading, is not directly comparable with ϵ for the test specimen, which is loaded uniaxially. In fact the maximum value of ϵ, deduced from measured bursting pressures and centre deflections of diaphragms removed from the tube immediately prior to rupture, appears to be between 17% and 18%. The post scribing tests were carried out with 0.017 in. thick diaphragms, which were preblown in the unscribed state to 210 psia. When removed from the tube, measurements of the centre deflection indicated very consistent strains of 16.5% in this condition. Table VI records the bursting pressures measured after scribing the prestressed diaphragms. The predicted bursting pressure, evaluated from the curves in fig.(6. 9) is 215 psia., if one assumes that the diaphragm undergoes no further deformation.

The results presented in Table VI suggest that the prestressing technique might be more successful if the preblowing pressure were to be reduced relative to the natural bursting pressure. It is also evident that the scribing has a marginal effect on the failing stress.

Preblow psia.	P_b psia.	x in.	%	P_b (predicted)
210	200	3.00	16.5	215
"	207	2.94	16.0	213
"	205	3.00	16.5	215
"	207	3.00	16.5	215
"	203	2.81	15.0	209
"	205	3.0	16.5	215
"	210	2.81	15.0	209
"	207	3.00	16.5	215
210	206		16.1	213

Table VI.

DIAPHRAGM OPENING TIME MEASUREMENTS.

The diaphragm was converted into a switch by stretching "Scotch Tape" across the surface, painting a conducting film on the tape and further insulating the conductor at one side by covering with another layer of tape.

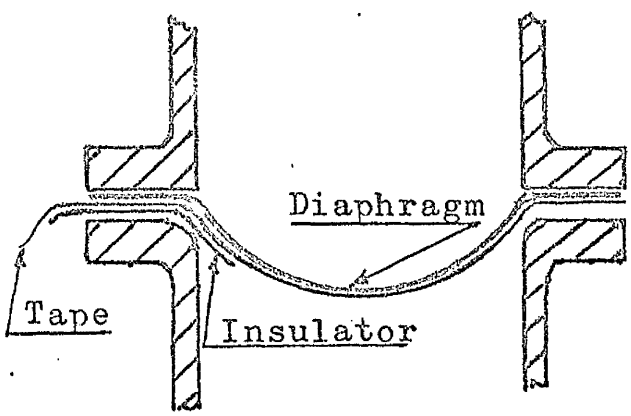

Fig.(6. 3)

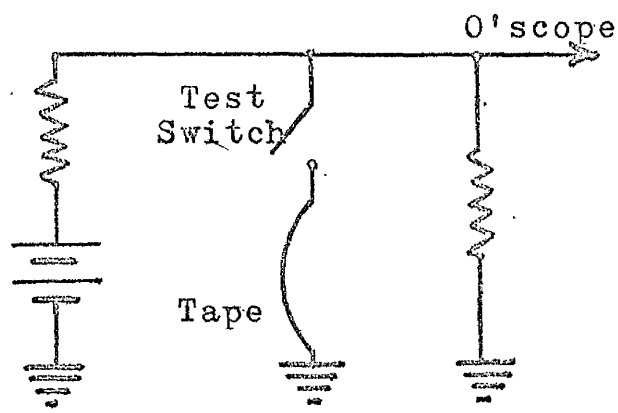

Fig.(6. 4)

The diaphragm had to be preblown to about 80% of its bursting pressure before applying the tape, otherwise it would invariably break before the diaphragm burst. Unfortunately one could never be sure when the tape ceased to conduct in relation to the diaphragm opening, with this technique.

A second method was adopted in an endeavour to resolve the uncertainty regarding the triggering. A small piezo electric crystal was clamped to the wall of the tube close to the diaphragm. This proved sensitive enough to detect the vibration of the diaphragm as it started to break. An insulated electrode, mounted flush with the wall of the tube, was employed to detect the moment when the petal struck the wall, the petal short circuiting the electrode to ground at the instant of impact. This method had the added advantage of indicating petal rebound, whilst the tape could not be relied upon to survive the first impact. Typical oscillograms, illustrating the type of record obtained with the two modes of triggering are shown in figs.(6. 17) and (6. 18).

The results obtained with the two methods are shown in figs.(6. 11) and 6. 12). One will immediately note the longer opening times obtained with the second method of measurement. This confirms the general conclusions of other observers, refs.(13) and (22), that the movement of the petals is slow over the initial period of opening. The results also indicate that consistent diaphragm bursts have yet to be obtained. Whilst some of the inconsistencies in our measurements have been attributed to inadequate definition of the trigger signal, there is enough evidence to indicate that differences in the initial rupture point, or points and crack propagation rates can lead to marked variations in the diaphragm opening characteristics.

SHOCK TRAJECTORY MEASUREMENTS ADJACENT TO THE DIAPHRAGM.

A heat transfer record obtained in the course of development work on the wall mounted heat transfer gauges gave us some reason to believe that the primary shock wave could be fully established within 6 feet of the diaphragm. This record, taken at station 6 feet, is shown in fig.(6. 14). there is no doubt that too much was read into this trace at

that time, but it did prompt further attempts to obtain similar results close to the diaphragm. This work was hampered by the limited number of data channels available for each shot. If the opening time was recorded on one channel, then only two others were left for heat transfer data. The lack of consistency in measured opening times, coupled with the uncertainty regarding the trigger signal, has further reduced the value of these results. The one event, in relation to the diaphragm motion, of which one can be sure, is the time t_w, when the petal first strikes the wall of the tube, consequently the results are plotted with reference to this time. Shock trajectories over the first 6 feet of the low pressure length are shown in fig.(6. 20). The scatter in the experimental values is large and the mean values obtained for the cases; $c = 3.10 \times 10^6$ and $c = 4.11 \times 10^6$ rad/sec.^{2} $p_1 = 10$ Torr.; cannot be described as adequately defined experimentally. They do,however, indicate that the theoretical predictions are well founded. The estimated shock trajectory for the case $c = 4.11 \times 10^6$, $p_1 = 10$ torr. is shown superimposed on the theoretical solution, plotted in fig.(5. 13). It is apparent that the boundary conditions for the two curves do not correspond, but any reassessment of the theoretical solution must await detailed measurements of petal trajectories.

Heat transfer records taken at stations close to the diaphragm are illustrated in figs.(6. 13) - (6. 16). In two of these a steep rise in temperature can be observed appearing some time after the passage of the initial shock front. This phenomenon has been attributed to either, a shock front, or a coalescing compression wave, which is virtually a shock wave. These secondary shocks must overtake the incident shock and in so doing, strengthen it. In fig.(6. 15) there is also some indication of the formation of a secondary shock at station 4 feet.

A multiplicity of secondary waves will be noted,

in particular, in the test illustrated in fig.(6. 16). The Shock Mach No. for this run, measured at station 15 feet, shows a large increase over the value normally recorded with this initial pressure ratio. This is an extraordinary result and is marked by a very short opening time, 750 microseconds, coupled with a much longer than usual rebound, 1000 microseconds. It has not so far proved possible to duplicate, or to establish the criteria relevant to the diaphragm, which led to this particularly rapid opening.

These results tend to confirm the hypothesis: secondary shocks are a consequence of the petal rebounding from the wall of the tube.

MEASUREMENTS OF MEAN SHOCK MACH No. AND RUNNING TIME.

It has been our practice to record the times taken by the shock to pass from station 14 feet $4\frac{1}{2}$ inches to station 17 feet $7\frac{1}{2}$ inches in all our test runs. With this information one can then find the mean Shock Mach No. at station 15 feet from fig.(2. 4). These results are not presented as such, but the value of M_s, so obtained, is used as a primary parameter.

Initial attempts to measure the duration of the quasi-steady flow, following the passage of the shock wave, were made using wall mounted thin film heat transfer gauges. Typical traces are illustrated in figs.(6. 21) - (6. 24) and it is apparent that positive interpretation of these oscillograms is not possible. In fig.(6. 22) the arrival of the contact surface is clearly defined, whereas in the remainder this is not the case. With the development of a satisfactory stagnation point thin film gauge the measurement of useful running times became very simple. If the stagnation point trace is linearised by squaring the voltage, then breakdown from quasi-steady conditions is clearly shown by departures from linearity. Results obtained with these transducers are

shown in figs.(6. 25) - (6. 27). The force of this technique will be noted, since the contact surface may be seen in each trace, whilst the normal departure from linearity clearly precedes the voltage peak, which denotes the contact surface. Further, it will be observed that in a number of cases the trace is increasing in slope immediately after the shock arrives at the monitoring station. Discussion of this feature is reserved for later.

Useful running time, expressed as a percentage of the ideal, is plotted in fig.(6. 28). This is based entirely on what little experimental data, which has been obtained to date. Such results will be affected by the channel pressure and the nature of the diaphragm burst. The worst possible combination of these parameters should be accounted for in the result plotted at $M_s = 6.33$. In this case a 0.005 inch thick 'Melinex' diaphragm was used with the channel pressure $p_1 = 0.2$ Torr. With this in mind, one should expect a useful running time not less than 40% of the ideal, in virtually all cases. The large scatter around $M_s = 3.0$, where the majority of the results were recorded, indicates the preponderance of variations in the diaphragm performance. It is not suggested that the information plotted in fig.(6. 28) is of general application, but it is included as a guide to the flow durations, which may be expected in the 12"x12" shock tube, bearing in mind its performance limitations.

It is interesting to compare the results shown in fig.(6. 27), when $M_s = 6.33$, with comparable ones obtained by Sandborn, ref.(23), in a 2.9 inch diameter tube. The apparent running time measured in the large tube is 300 microseconds at 17 feet from the diaphragm, whereas that, obtained at a point 18.7 feet from the diaphragm in the small tube, is only 60 microseconds.

Another interesting comparison may be drawn between these results.

	12"x12" Tube	2.9" Dia. Tube ref.(23)
Diaphragm constant $\underline{c}$ rad/sec.^{2}	: 16×10^6	20×10^6 (estd. from ref.(22)
p_4/p_1	: 3690	3690
p_1, Torr.	: 0.20	0.36
Shock Mach No., M_s measured at,	: 6.33	6.33
Station, feet	: 15.0	12.0
x.c	: 240	240

The above comparison tends to suggest that the "shock formation" distance is in inverse proportion to the value of $\underline{c}$, for similar gas combinations.

From the data presented in Chapter 3, one can say that the loss in running time for the case $M_s = 3$, $p_1 = 10$ Torr., resulting from real gas and viscous effects, is approximately 1% of the ideal running time, at station 17 feet. In order to confirm the implication that the loss of running time observed in the cases cited above is due largely to non-ideal diaphragm performance, a comparison is made between the run M.5, shown in fig.(6. 26), and the characteristic solution presented in fig.(5. 13).

The apparent running time, the time difference between the passage of the shock wave and the contact surface at a fixed station, is measured at station 17 feet and the Shock Mach No. at station 15 feet.

$$\triangle t_{(\text{apparent})} = 1240 \text{ microsecs.}$$

$$M_s = 3.0$$

From the characteristic solution, fig.(5. 13) the corresponding figures are;

$$\triangle t_{(\text{apparent})} = 1360 \text{ microsecs.}$$

$$M_s = 3.0.$$

It should be noted that the diaphragm used in the case of run M.5. has different characteristics to those, which were assumed in the calculation. The comparison does serve to illustrate the marked loss in running time caused by the diaphragm taking a finite time to open. Physically this loss in flow duration is readily explained.

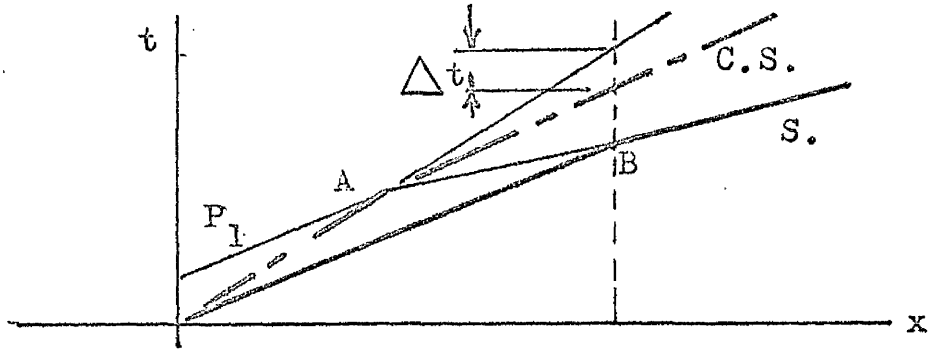

Fig.(6. 5)

Fig.(6. 5) is the x-t diagram following the opening of the diaphragm. Initially one has a shock wave weaker than that predicted by the ideal case, with its associated contact surface. Following characteristic P_1; it reaches the contact surface at point A, whereupon the contact surface is accelerated. P_1 does not, however, reach the shock wave until point B. During this period the contact surface velocity is greater than that implied by the shock strength over the period AB. A loss in running time $\triangle t_1$ is shown, which is increased for each subsequent characteristic. The nett loss by this analysis cannot then be compared with the ideal case directly. In fact one is comparing the running times obtained with the trajectories as shown in fig.(6. 6).

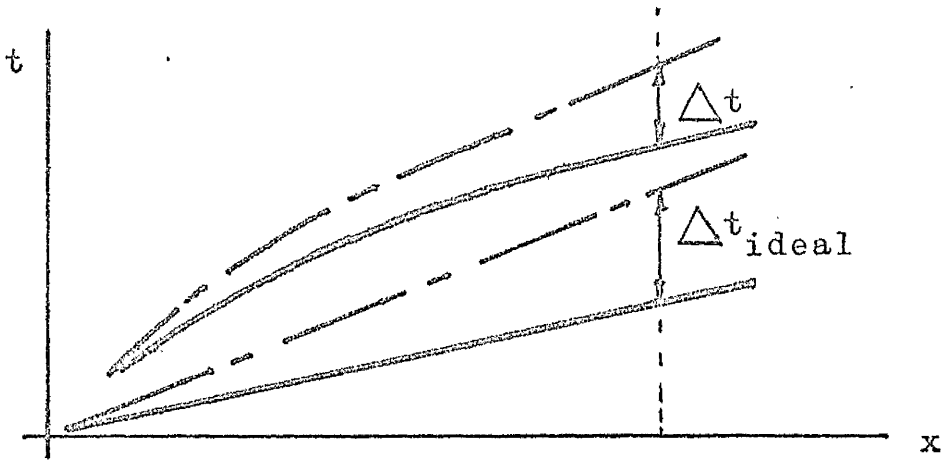

Fig.(6. 6)

NON-UNIFORMITIES IN THE FLOW PAST A STATION, FOLLOWING THE PASSAGE OF THE PRIMARY SHOCK WAVE.

It has been noted that the linearised stagnation point heat transfer traces were not consistently linear up to the time, at which mixing of the gases in front of the contact surface began to affect the transfer of heat to the probe. It is to be expected, that it will take some time to establish the flow around the cylindrical probe. It was suggested by Dr. Davies, on the basis of unpublished work carried out at the National Physical Laboratory, that this time, in our particular case, should be of the order, 50 microseconds.

Figs.(6. 25) - (6. 27) illustrate three stagnation point heat transfer records obtained using a cylindrical probe, of the type shown in fig.(4. 11). Results, figs.(6. 25) (6. 26), were obtained for practically identical bursting pressures and, whilst (6. 25) is markedly non-linear, there is no doubt, that the linearised trace in the other, is a straight line.

Similarly, the results for the Helium driven test, fig.(6. 27), show a constantly increasing heat transfer rate,

as indicated by the progressive increase in the slope of the curve. This is, as one would expect, from the analysis of this run, given on page 105.

A rough assessment has been made in Appendix I, of the sensitivity of the stagnation point heat transfer rate, $\dot{q}$, which is virtually proportional to $\triangle E/_{t}^{\frac{1}{2}}$, to small variations in the flow in region 2.

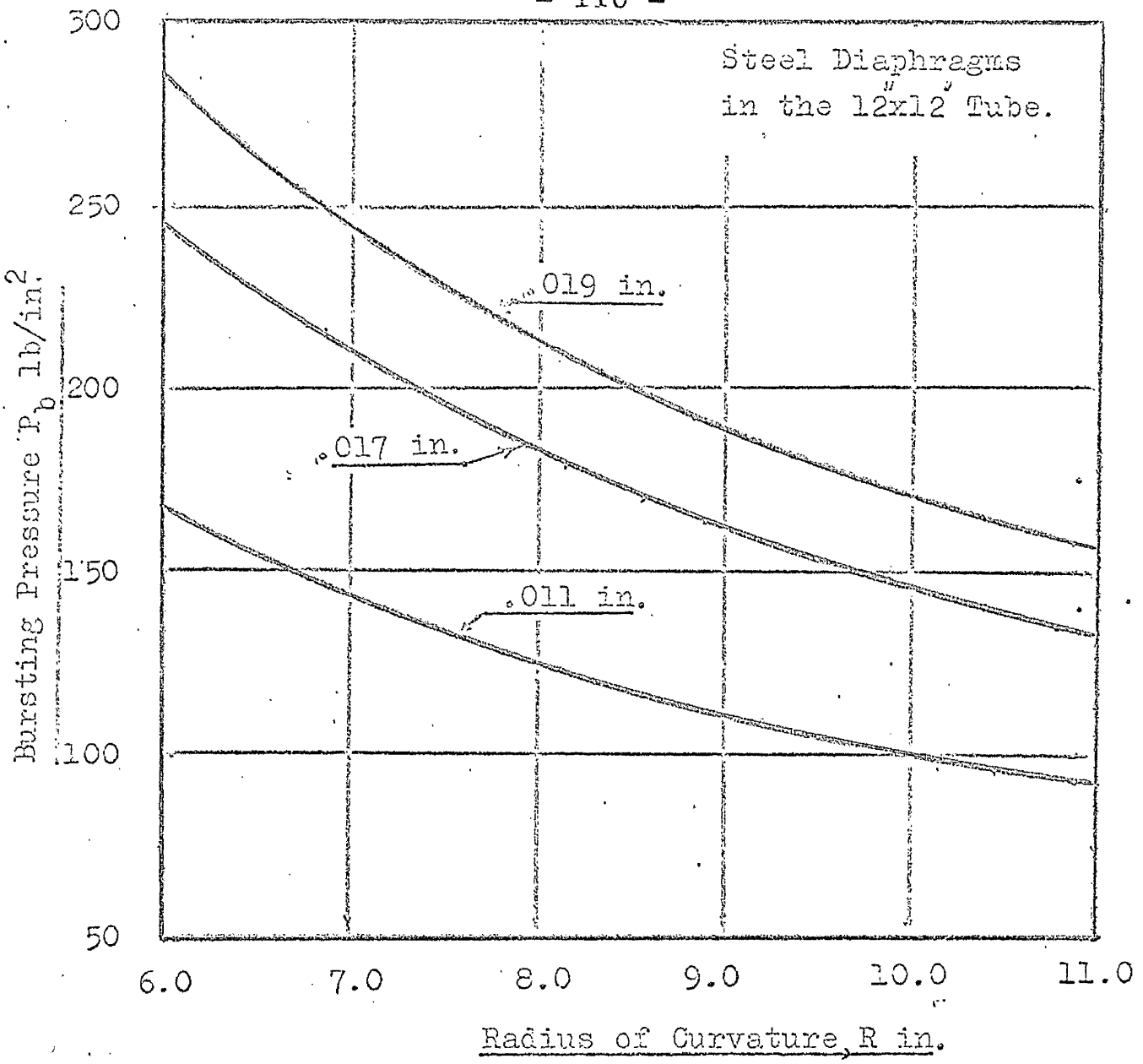

Fig.(6. 7) Theoretical Bursting Pressure versus R.

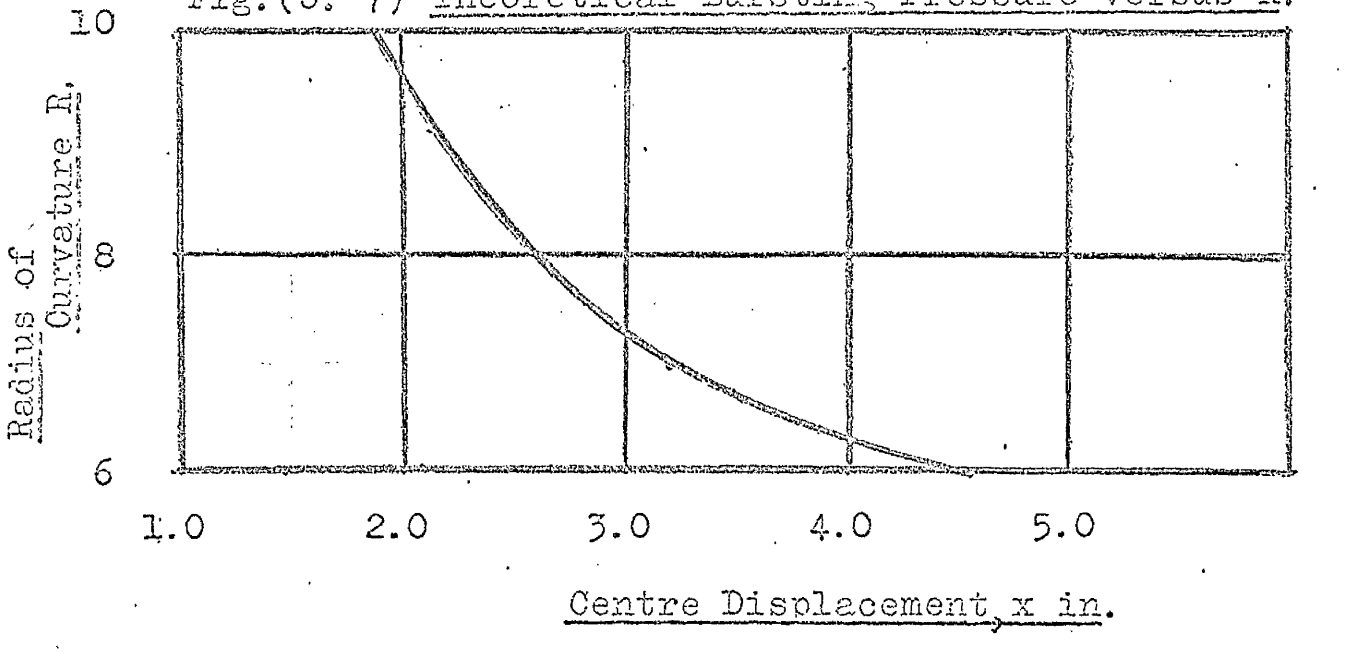

Fig.(6.8) Calculated Correspondence between R and x.

Equations — $\alpha = {}^{1}/_{R}.(1 + \varepsilon)$ and ${}^{1}/_{R} = \sin.\alpha$

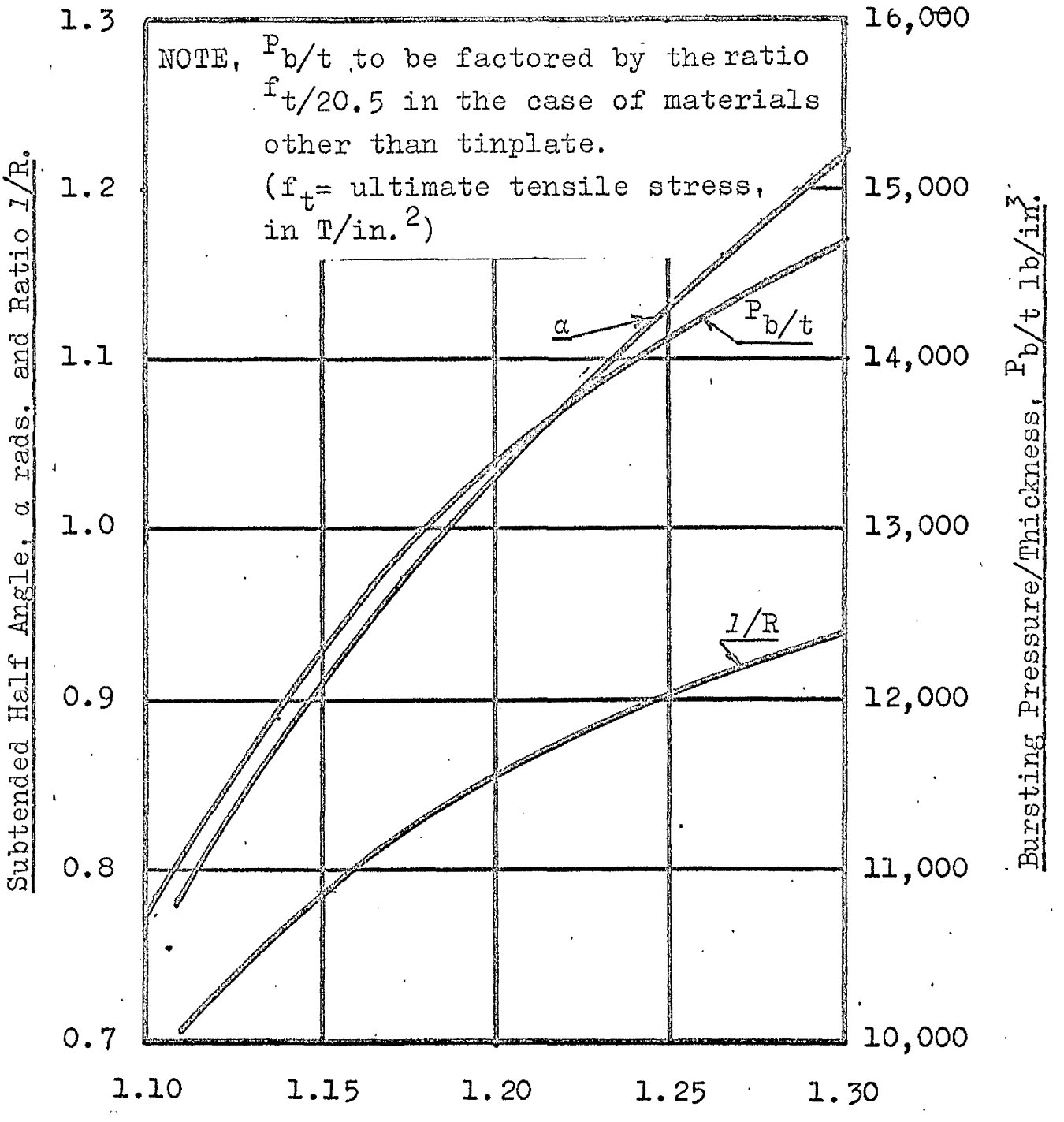

Fig.(6. 9) Diaphragm Bursting and Deformation Characteristics.

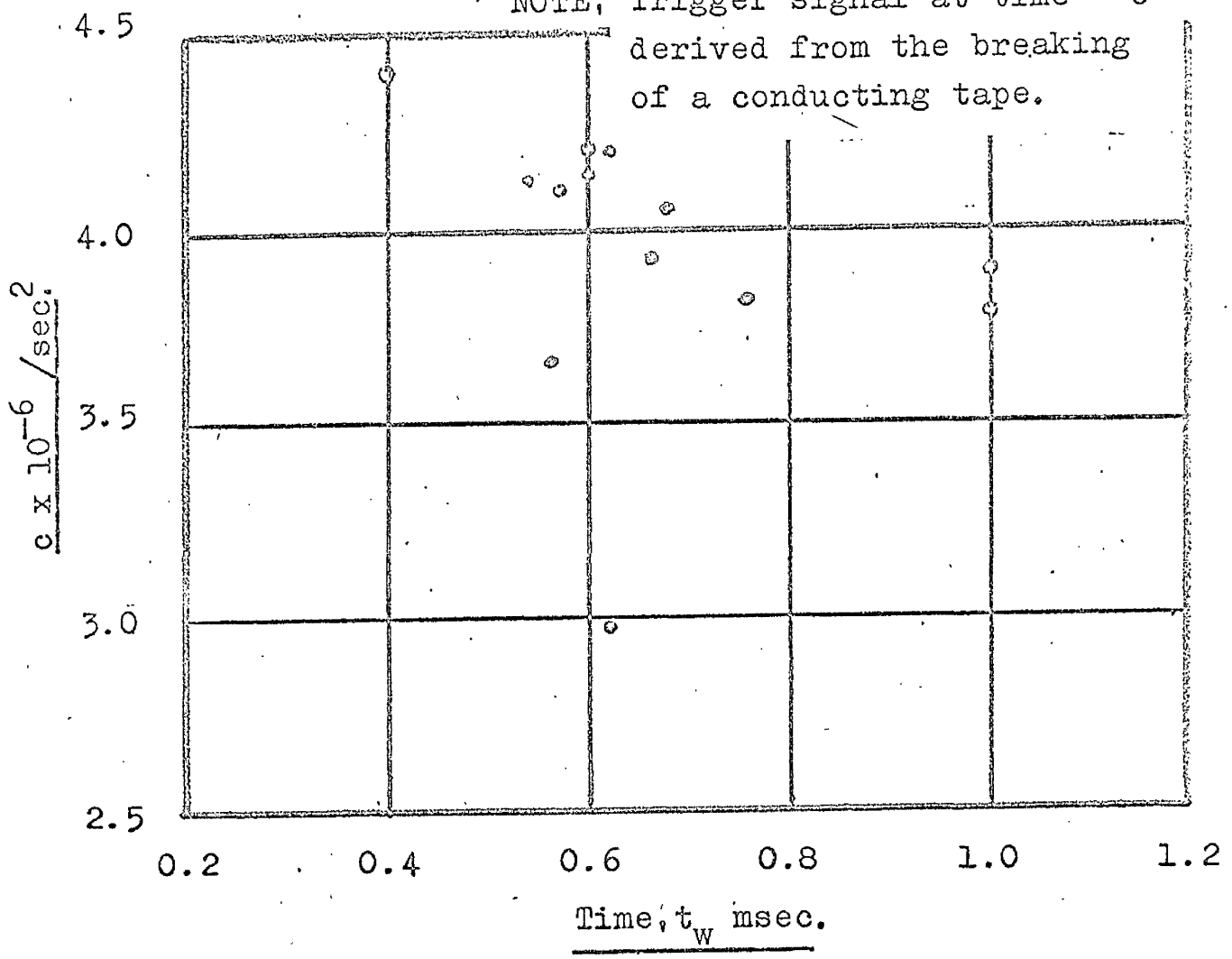

Fig.(6. 11) Diaphragm Opening Time Plotted against c.

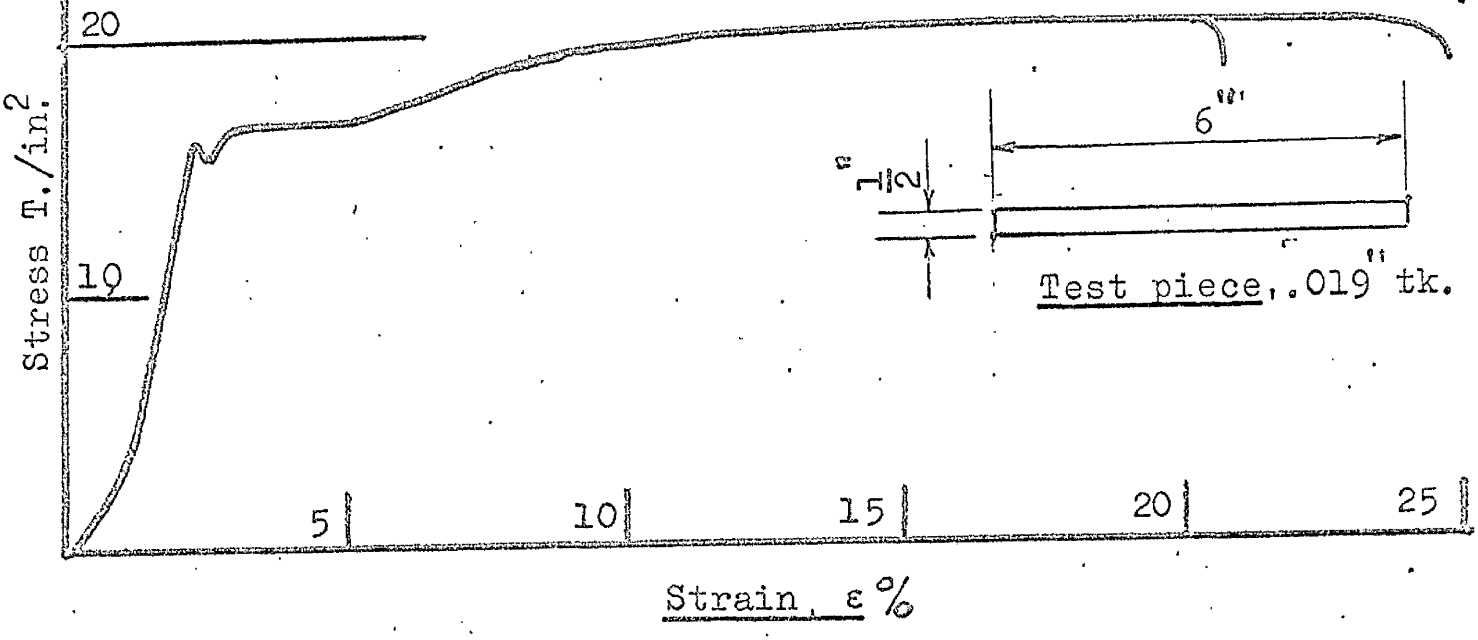

Fig.(6. 10) Stress / Strain Characteristic for Tinplate.

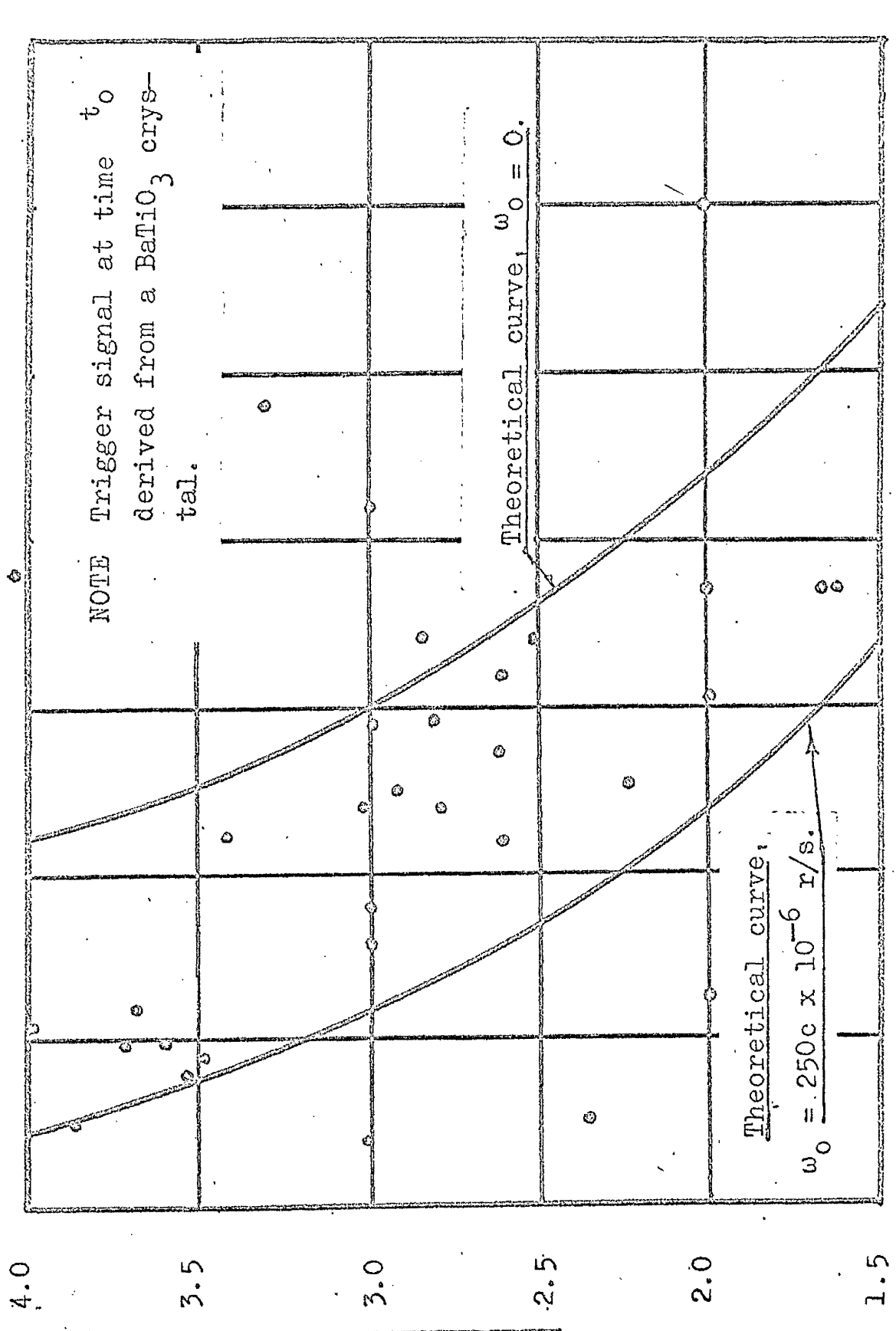

Fig. (6. 12) Diaphragm Opening Time, t_w, Plotted against Factor c.

Figs.(6. 13 –16), Heat Transfer Records, Obtained at Stns. 2' – 6', Air : Air.

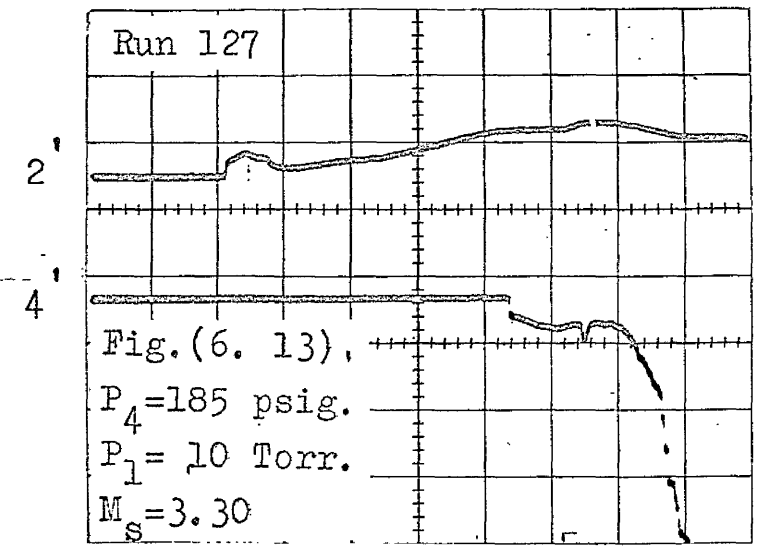

200 μsec./cm.

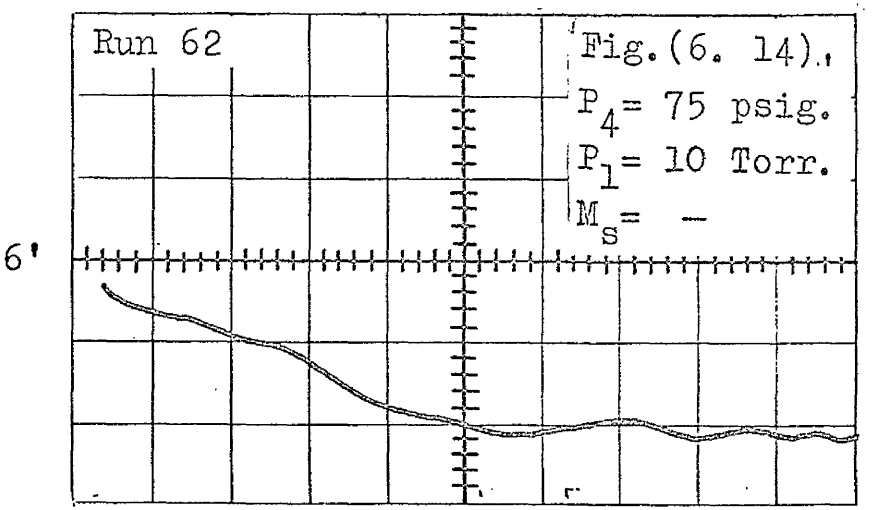

100 μsec./cm.

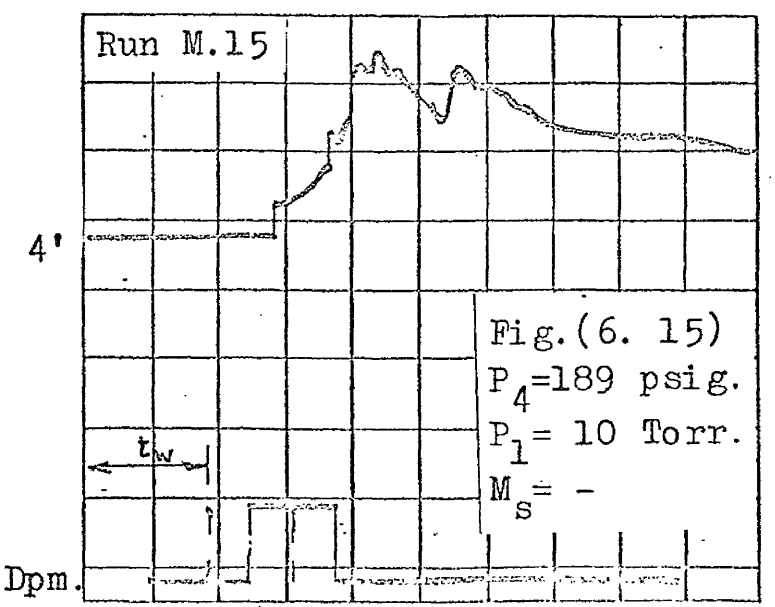

500 μsec./cm.

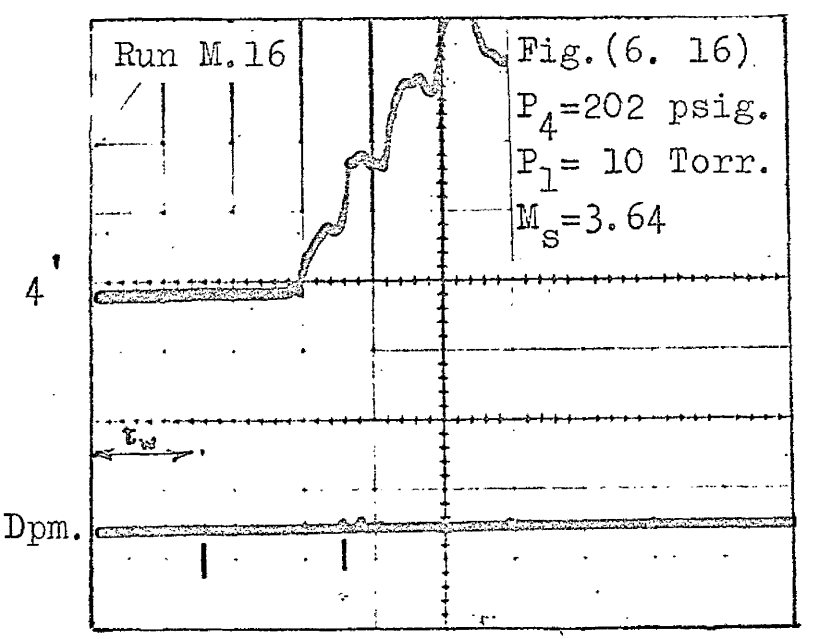

500 μsec./cm.

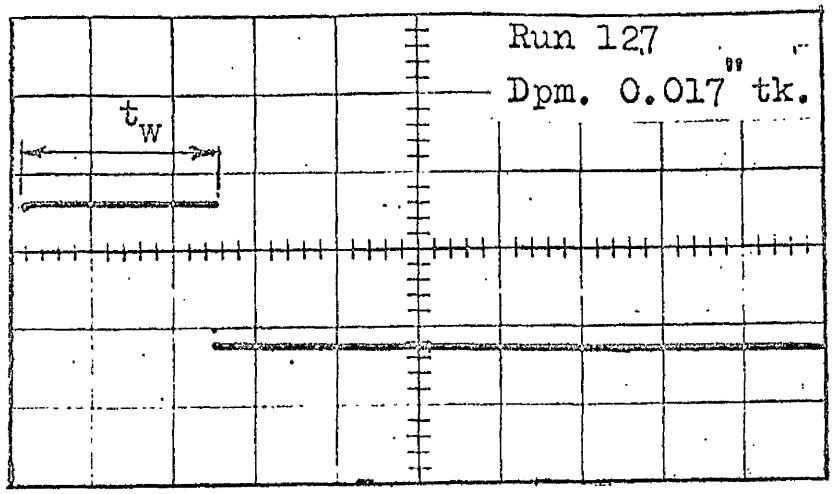

200 μsec./cm.

Fig.(6. 17)

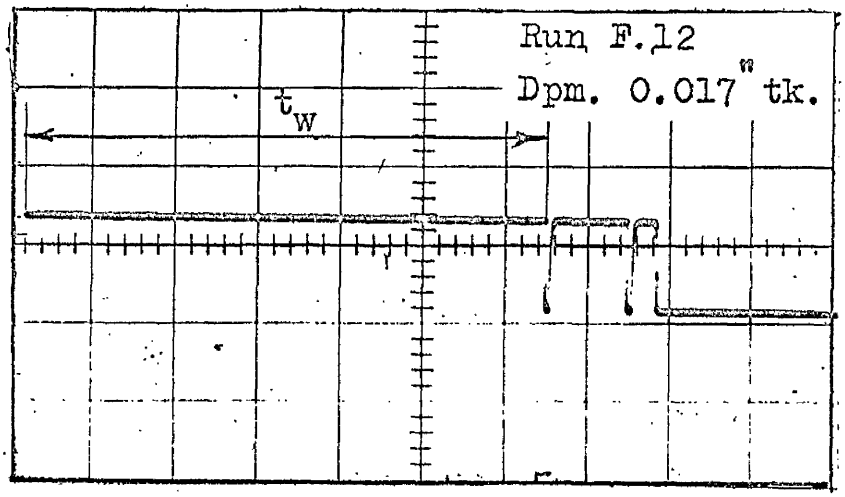

200 μsec./cm.

Fig.(6. 18)

Diaphragm Opening Time, t_w, Measured with Tape Controlled and Crystal Controlled, Triggering, Respectively.

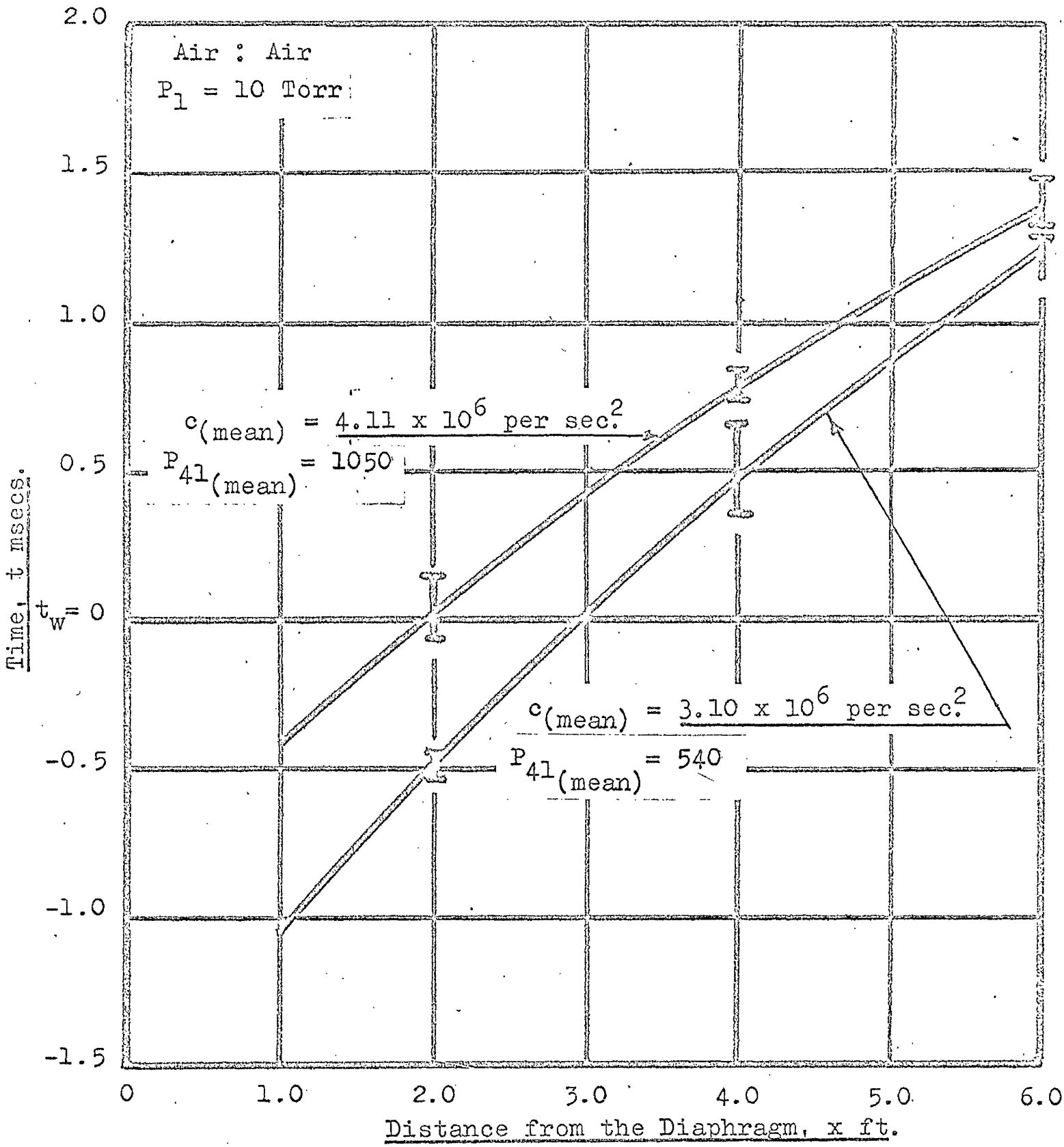

Fig.(6. 20) Experimentally Determined Shock Trajectories.

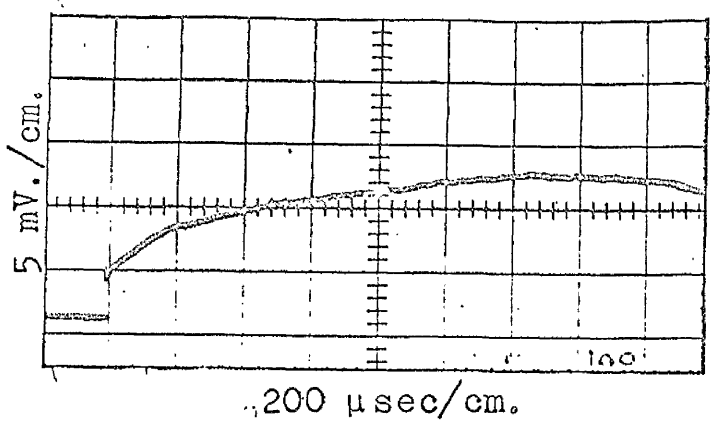

Fig.(6. 21) Heat Transfer to the Wall, Run 100.

M_s = 3.14, R = 100 I =25 mA

P_1 = 10 Torr., Lcn.– 15 ft.

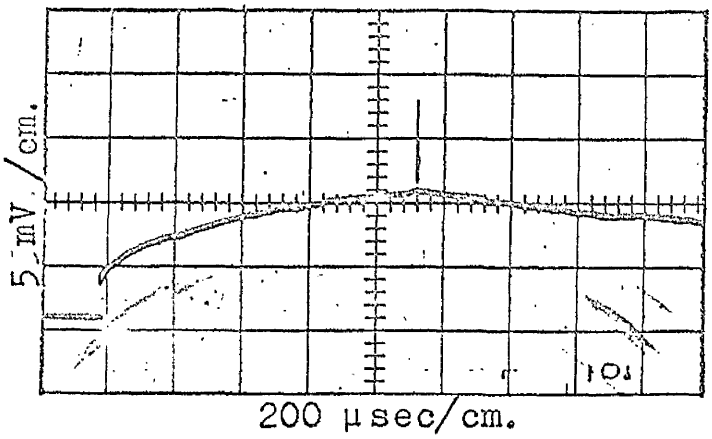

Fig.(6. 22) Heat Transfer to the Wall, Run 101.

M_s = 3.24, R = 100 I =25 mA

P_1 = 10 Torr., Lcn.– 15 ft.

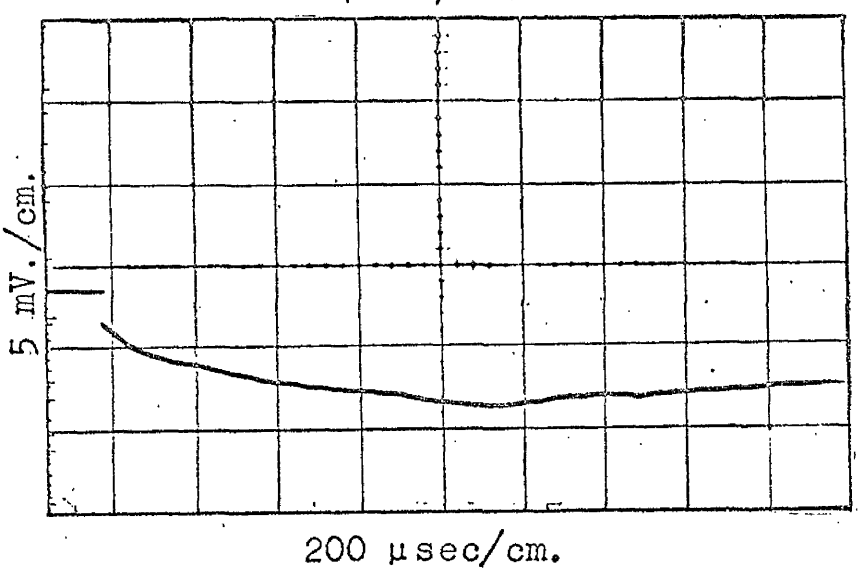

Fig.(6. 23) Heat Transfer to the Wall, Run 109

M_s = 3.34, R = 100
I = 15 mA.

P_1 = 10 Torr

Lcn. – 15 ft.

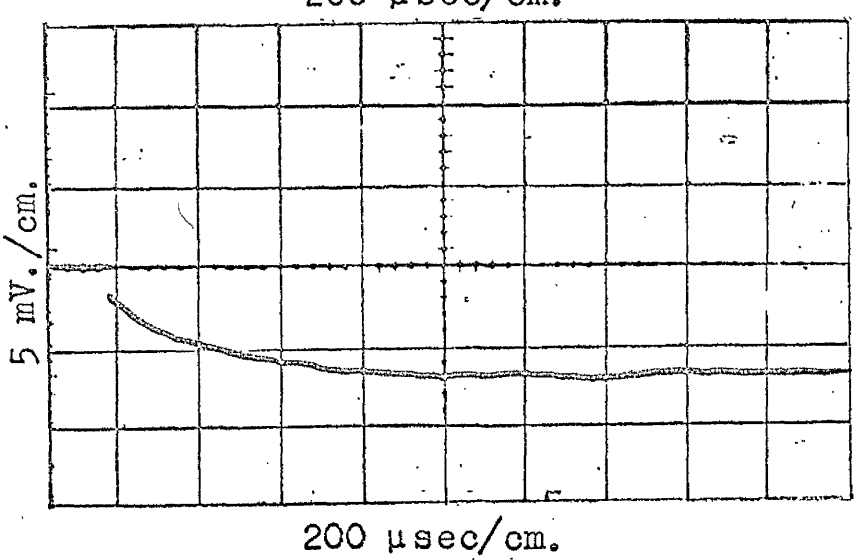

Fig.(6. 24) Heat Transfer to the Wall, Run 110

M_s = 3.20, R = 100
I = 15 mA.

P_1 = 10 Torr.

Lcn. – 15 ft.

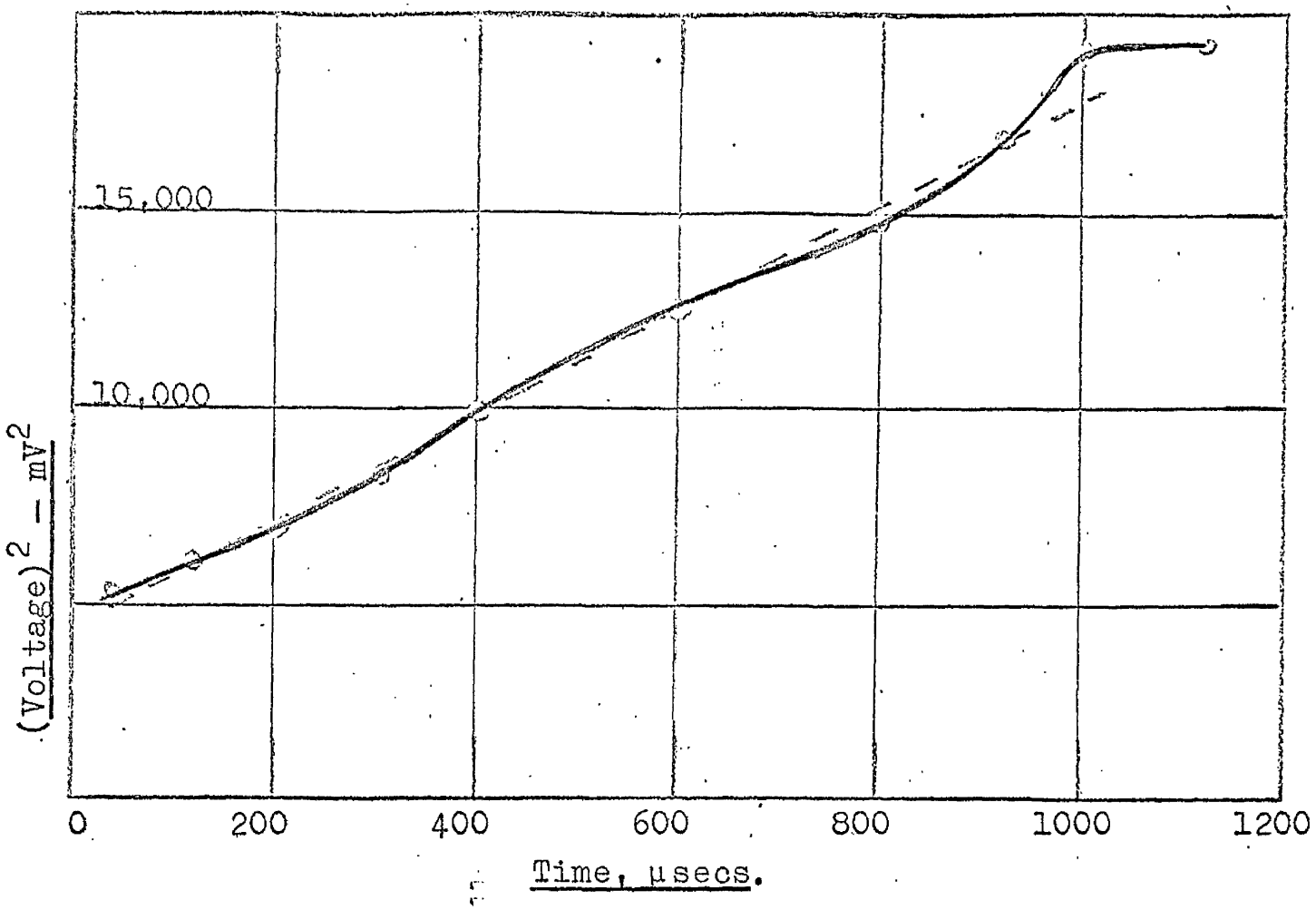

Test Conditions :

Air : Air, M_s = 3.05, P_1 = 10 Torr.
R = 300 , I = 20.5 mamp.

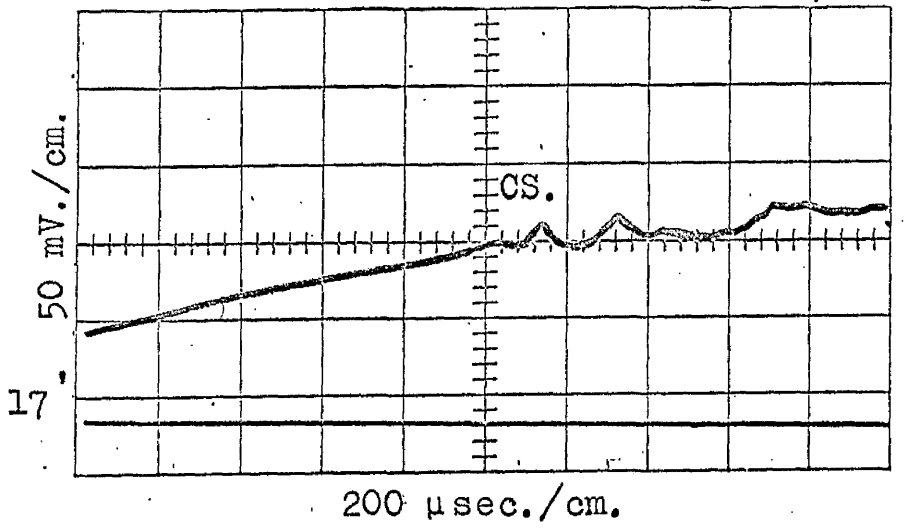

Fig.(6. 25) Stagnation Point Heat Transfer Record, Run M.1.

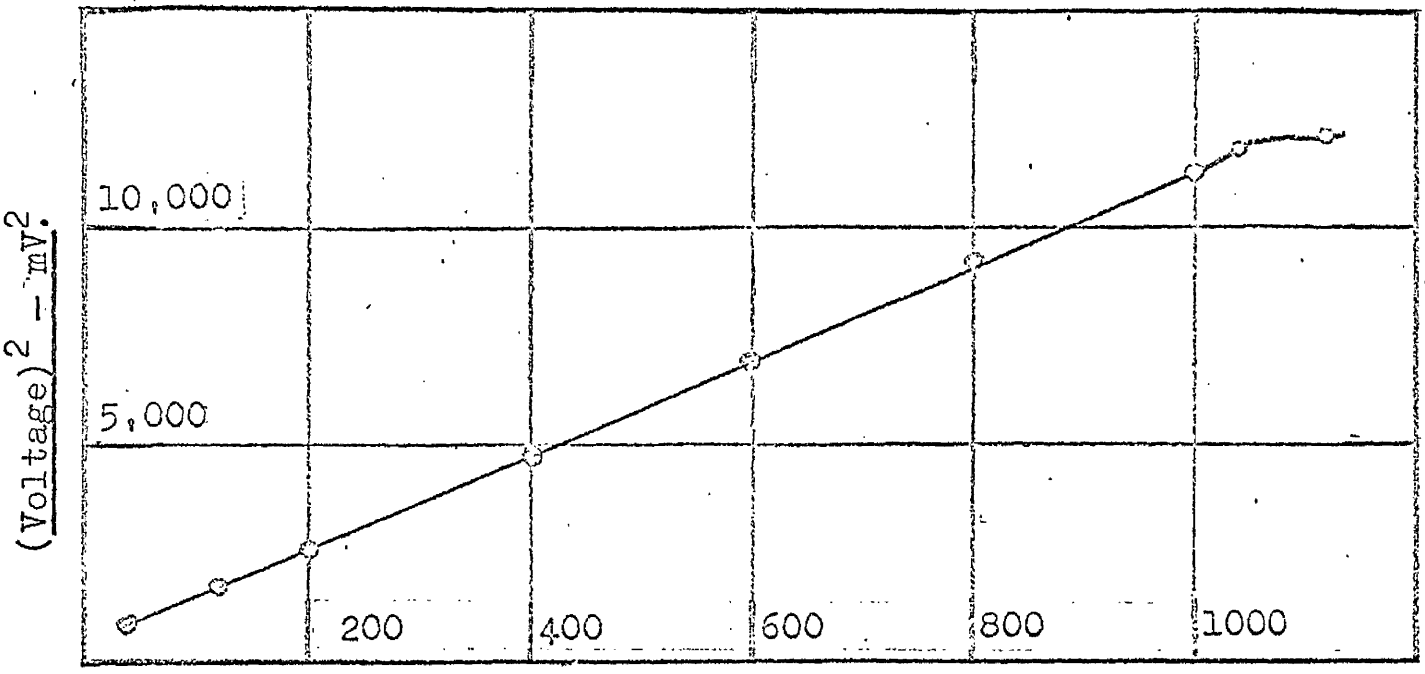

Test Conditions :

Air : Air, M_s = 3.01, P_1 = 10 Torr.
R = 300Ω, I = 20.5 mamp.

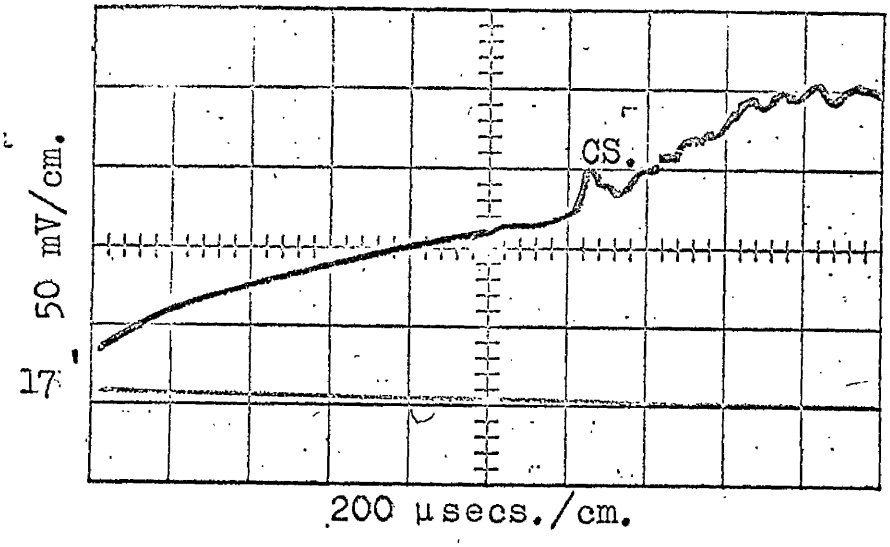

Fig.(6. 26) Stagnation Point Heat Transfer Record, Run M.5.

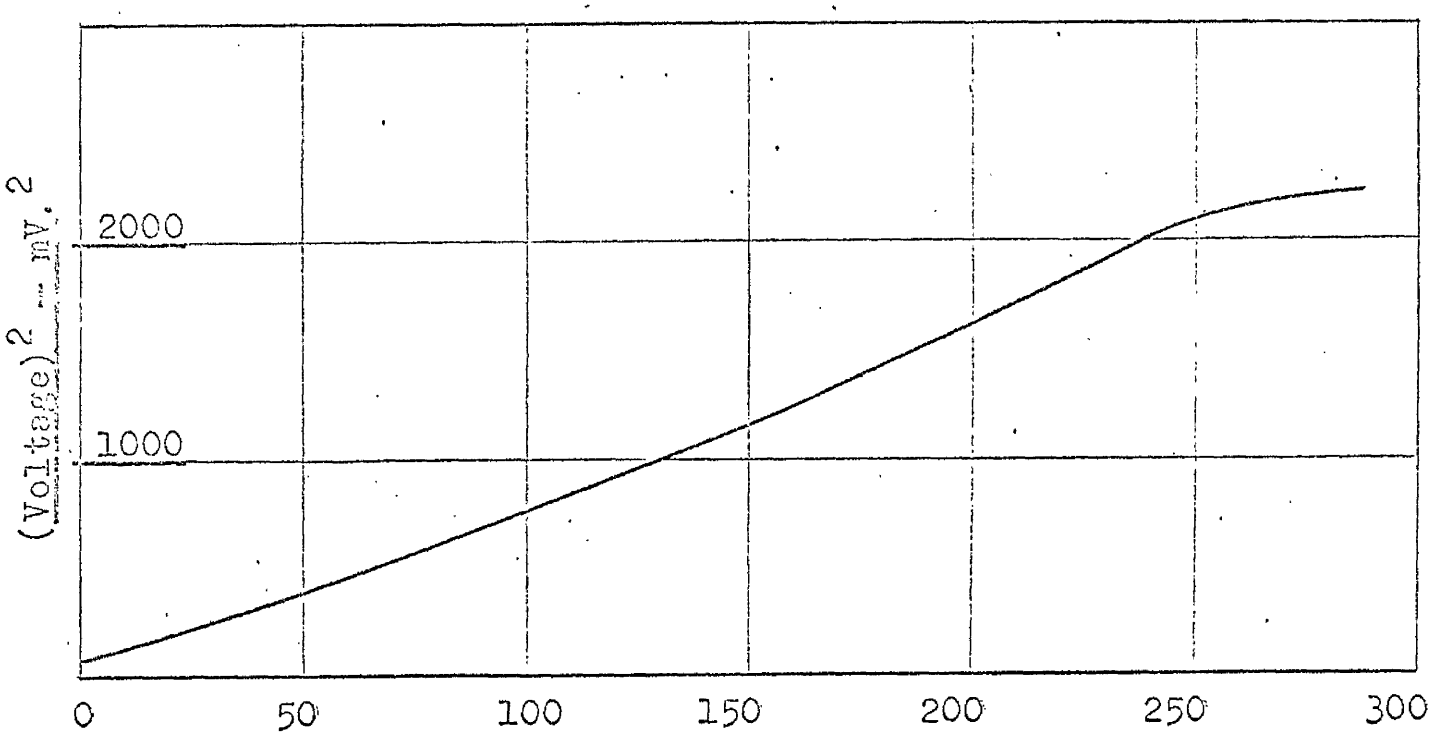

Test Conditions :

He : Air, $M_s = 6.33$, $P_1 = 0.2$ Torr.

$R = 300\Omega$., $I = 20.5$ mamp.

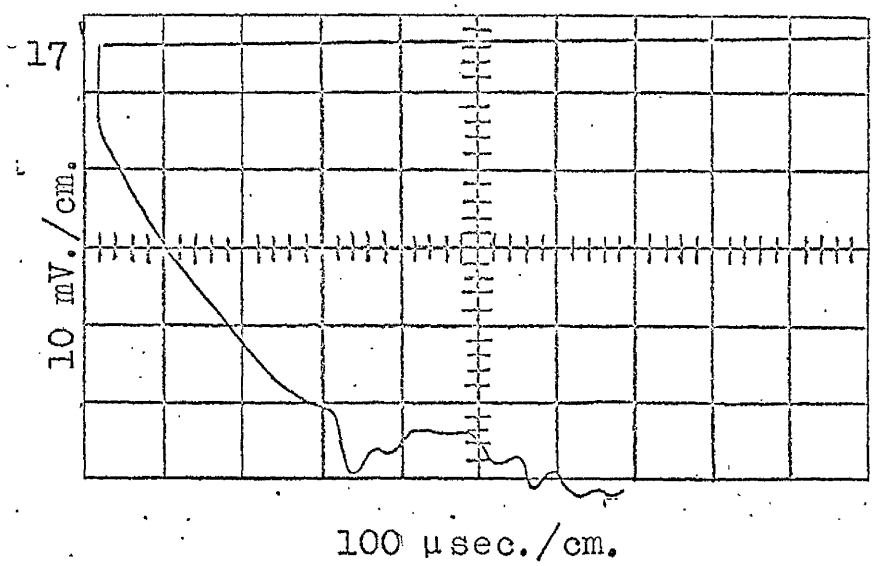

Fig.(6. 27) Stagnation Point Heat Transfer Record, Run M.10.

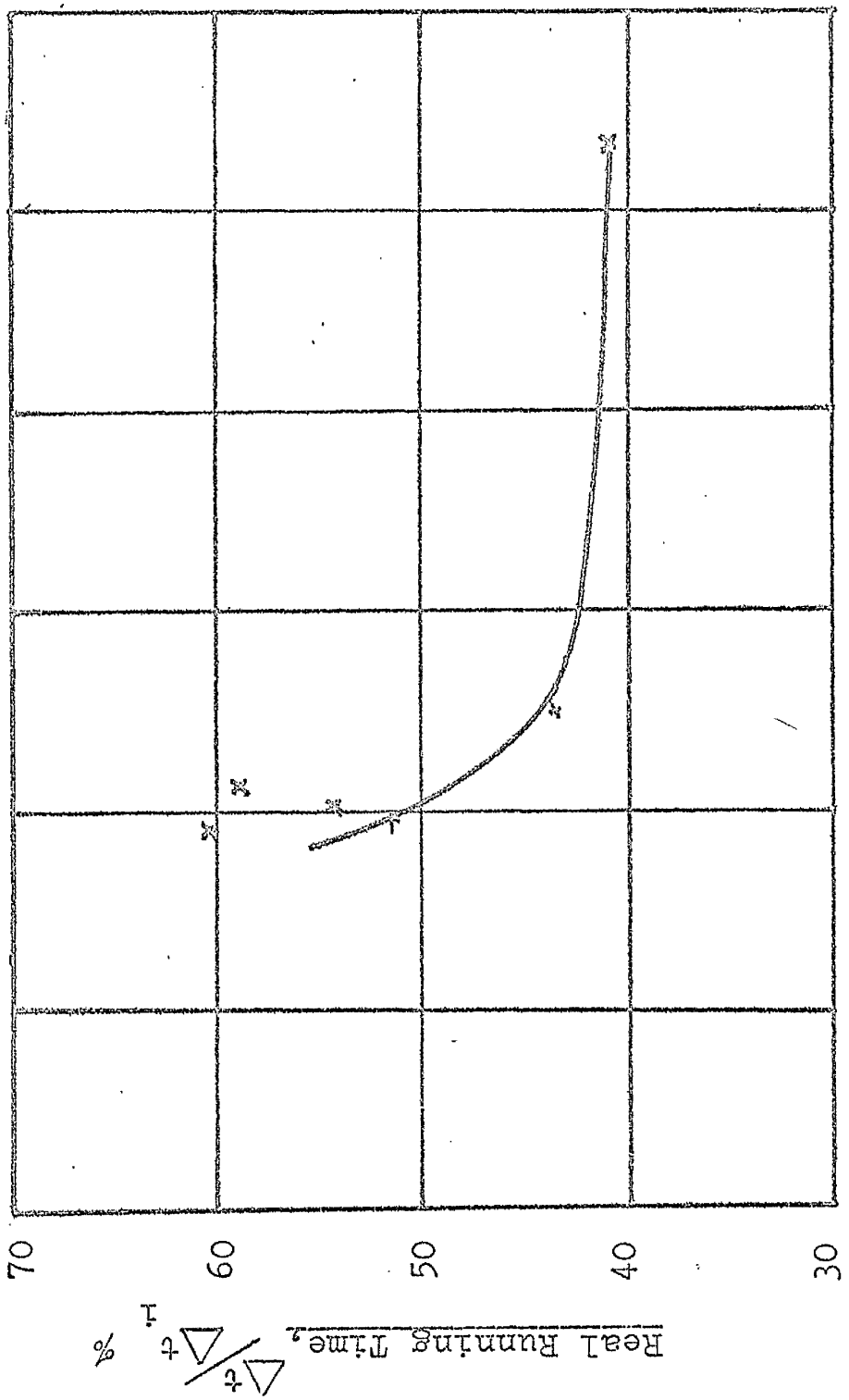

Fig.(6. 28) Real Flow Durations $\Delta t / \Delta t_i$, Measured at Stn. 17 ft. in the 12"x12" Shock Tube.

IN CONCLUSION

THE 12" x 12" SHOCK TUBE.

The basic concept behind the design of the tube, was to use a large section in order to reduce viscous interference at the "working section" to an absolute minimum. In this limited objective the design was successful, in that apparent flow durations, measured in the Glasgow Tube were about five times those, measured in the 2.9 inch diameter tube, ref.(23), for practically identical gas combinations, at similar distances from the diaphragm.

It is clear from both, the experimental results and the theoretical work, that the tube is too short, for operation with conventional diaphragm techniques. At the lower Shock Mach Numbers, associated with Air : Air driving, the length is marginal, in that the shock appears to "form" about 17 - 18 feet from the diaphragm. With Helium driving, however, it would appear that the shock will not form within the length of the tube.

GENERAL REMARKS ON PETALLING DIAPHRAGMS.

A factor,

$$c = 2\sqrt{3}\ \frac{p_4 \cdot g}{aW} \cdot \frac{k+1}{3k+2}\ ,$$

has been derived, which is indicative of diaphragm efficiency. It is not an absolute measure of efficiency, since it makes no allowance for rupturing characteristics. In addition the effect of the rupturing characteristics on the shock trajectory is still largely undetermined, anyway.

The criteria, which govern when the conditions at the outlet from the varying nozzle at the diaphragm should be "matched" to those in the undisturbed channel, have yet to be established. It is essential to know whether this is basically, a time dependent, or a mass flow controlled, condition. If the matching conditions are inherently a function of the mass flow, then the mechanism of rupture is relatively insignificant, since the primary shock will rapidly overtake the weak disturbances, associated with the initial rupture.

A circular tube should lead to longer "shock formation distances", owing to the increased stiffness of the petals, in opposition to bending. This could be alleviated by increasing the number of petals.

A petalling diaphragm would, if there was no viscous attenuation, lead to a shock wave, which was continuously accelerating asymptotically to the strength, given by the ideal instantaneous opening analysis. In effect, what happens in the actual case is that, some way down the tube, viscous attenuation and compression acceleration cancel out and the shock wave reaches a maximum strength, after which,it is continuously weakened until it reaches the end of the tube. Of the two mechanisms, which cause flow variations in the time dependent quasi-steady flow at a fixed station, which is the worst in any particular case, is still a matter for conjecture. This paper indicates a theoretical approach, which allows one to calculate the effect of the diaphragm.

It has been shown that the opening of the diaphragm can lead to significant reductions in flow duration at a fixed station, and this should be borne in mind, when considering viscous flow losses. Once again, the method, by which this loss was evaluated, does not allow one to draw general conclusions.

COMPARISON WITH KIREYEV'S SOLUTION, ref.(14), FOR A PETALLING DIAPHRAGM.

The main difference between the two solutions lies in the inclusion of the petal tip velocity in the calculations presented in this paper. This was necessary in our case, since the petal tip moves so fast, relative to the speed of sound in the driving gas. Generally, with smaller tubes and light gas driving, the petal tip velocity will be insignificant. There is also a difference in the treatment of the expansion of the driving gas in region 4 to the inlet of the nozzle, between the two calculations, but the effect of this on the shock wave trajectory should be negligible.

In the presentation of results, Kireyev is somewhat misleading. For any specific measured opening time the "shock formation distance" is independent of the tube section. Kireyev shows the relationship between the local shock velocity and the maximum, plotted against distance from the diaphragm, expressed in tube diameters. The presentation is, however, only relevant to the particular tube and the particular diaphragm, for which the calculations were made.

The method of characteristics does not permit one to pinpoint the effect of any specific parameter on the final solution and it is only by doing a number of calculations on representative configurations, will it be possible to infer a general trend in any particular direction.

USE OF STAGNATION POINT HEAT TRANSFER PROBES TO INVESTIGATE VARIATIONS IN THE QUASI-STEADY FLOW.

The stagnation point heat transfer probe has much to commend it, as an indicator of non-uniformities in the flow. It is cheap to make, simple to install, insensitive to vibration and easy to calibrate, ref.(25). In Appendix I preliminary calculations

suggest that it could be used as a very sensitive indicator of departures from quasi-steady flow, when, as in our case, the variations were such, as to lead to a continual increase in heat transfer rate, with time, until the arrival of the contact surface.

It is unfortunate, that when the results quoted in Chapter 6 were obtained, no attempt was made to calibrate the probes used. If the probes had been calibrated it would then have been possible to infer from the linearised traces the actual magnitude of the flow disturbances and relate them to fig. (5. 17).

APPENDIX I

STAGNATION POINT HEAT TRANSFER.

The relative sensitivity of the output from a stagnation point heat transfer probe is assessed for minor flow variations in region 2.

Using the method of ref.(24), the stagnation point heat transfer rate for a cylindrical body in supersonic flow is calculated.

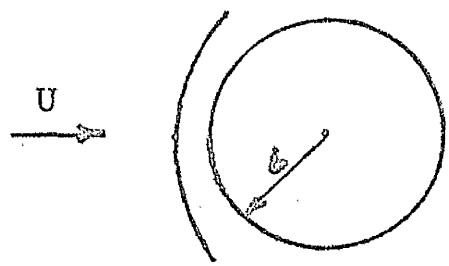

Fig.(A-I. 1)

The recovery temperature T_r is given by,

$$T_r = T\left(1 + \frac{\gamma - 1}{2} M^2\right), \qquad \ldots.(A\text{-}I.\ 1)$$

therefore,

$$(T_r - T_w) = T - T_w + \frac{\gamma - 1}{2} M^2.T, \quad \ldots(A\text{-}I.\ 2)$$

where T = static temperature in the free stream.

Then,

$$(T_r - T_w) = (T - T_w) + \frac{U^2}{2C_p}. \qquad \ldots.(A\text{-}I.\ 3)$$

Using the relation,

$$\dot{q} = - \frac{Nu_r . k_r . (T_w - T_r)}{d}, \qquad \ldots.(A\text{-}I.\ 4)$$

for heat transfer rate / unit area,

and

$$Nu_r = 0.934\ Re_g^{.5} . Pr^{.4},$$

which is valid for laminar incompressible flow and consequently assumed to be valid near the stagnation point, then,

$$\dot{q} = 0.934\sqrt{\frac{\rho U \delta}{\mu_r}} \cdot \frac{k_r}{\delta} \cdot (T - T_w) + 0.47\sqrt{\frac{\rho U \delta}{\mu_r}} \cdot \frac{k_r \cdot U^2}{\delta \cdot C_p} \quad \ldots\ldots(A\text{-}I.\ 5)$$

Putting, $\quad Pr. = \dfrac{\mu_r \cdot C_p}{k_r} = 1.0,$

then,

$$\dot{q} = 0.934\sqrt{\frac{\rho U \mu_r}{\delta}} \cdot C_p(T - T_w) + 0.47\sqrt{\frac{\rho U \mu_r}{\delta}} \cdot U^2 \cdot \quad \ldots\ldots(A\text{-}I.\ 6)$$

Let,

$$\mu_r = 2.31 \times 10^{-8} \cdot T_r^{.5}$$

and

$$T_r = \frac{U^2}{2C_p},$$

hence,

$$\dot{q} = 14 \times 10^{-6}\sqrt{\frac{\rho}{\delta}} \cdot UC_p(T - T_w) + 7 \times 10^{-6}\sqrt{\frac{\rho}{\delta}} \cdot U^3$$

and

$$\frac{\partial \dot{q}}{\partial U} = 14 \times 10^{-6}\sqrt{\frac{\rho}{\delta}} \cdot C_p(T - T_w) + 10.5 \times 10^{-6}\sqrt{\frac{\rho}{\delta}} \cdot \frac{U^2}{2} \quad \ldots\ldots(A\text{-}I.\ 7)$$

The relationship between the voltage response of the stagnation point thin film gauge and the actual heat transfer rate is derived in ref.(25);

ie.

$$\dot{q} = \frac{2}{\pi}\left[\frac{4.19}{2.E_o}\sqrt{\pi}\sqrt{\rho ck} \cdot \frac{E(t)}{t^{\frac{1}{2}}}\right] + \int_o^t f\left[E(t), \tau\right] d\tau$$

or

$$\dot{q}^2 = \text{const.}\ \frac{E(t)}{t}^2 + \left[\text{Integral term}\right]^2$$

One will observe, from the form of equation (A-I. 7), that $\frac{\partial \check{q}}{\partial U}$ is a function of the static head and the dynamic head, hence one would expect the stagnation point gauge, the output of which is a function of $\check{q}$, to be a sensitive indicator of static temperature variations behind the incident shock. In addition the temperature behind a developing shock wave increases and since the probe is an integrating device, the sensitivity will be further enhanced. The actual form in which the data is used also increases the apparent sensitivity of the probe, because it is much more convenient to examine a curve for non-linearity, rather than try to estimate the deviations from the ideal case, when that ideal is a parabola.